Development and Assessment of Focused Ultrasound-Based Approaches for Non-Viral Transfection of Brain Tumors

---

A Dissertation

Presented to

the faculty of the School of Engineering and Applied Science

University of Virginia

---

in partial fulfillment
of the requirements for the degree

Doctor of Philosophy

by

Colleen T Curley

December 2019

APPROVAL SHEET

This Dissertation
is submitted in partial fulfillment of the requirements
for the degree of
Doctor of Philosophy

Author Signature: Colleen T. Curley

This Dissertation has been read and approved by the examining committee:

Advisor: Richard Price

Committee Member: Brent French

Committee Member: Timothy Bullock

Committee Member: Jennifer Munson

Committee Member: Benjamin Purow

Committee Member: _____

Accepted for the School of Engineering and Applied Science:

Craig H. Benson, School of Engineering and Applied Science

December 2019

Acknowledgements

There are many people that I need to thank for their help and support throughout my time at UVA. First, I would like to acknowledge my advisor, Dr. Richard Price. I cannot thank you enough for your support, encouragement, and guidance throughout the course of these research projects. I would also like to thank the current and former members of the Price Lab. In particular, thank you to Brian Mead for your collaboration and friendship during our shared time in the Price lab. Thank you to Ji Song, Alex Mathew, Katie Gorick, and Andrew Thim, who have all helped immensely with wrapping up this work over the last few months.

I am grateful to my many collaborators for their crucial contributions to these projects. In particular, I would like to acknowledge Karina, Divya, Namho, and the whole team at Johns Hopkins for their work on the BPN projects. Thank you to Jenny Munson and Kathryn Kingsmore, your expertise has greatly enhanced the impact of this work. Thank you to Tim Bullock, Aaron Stevens, Kasia Stasiak, Aly Witter, and Natasha Sheybani for collaboration on the intracranial melanoma immunology projects. None of the experiments in this dissertation could have been completed without the help of Wilson Miller and Will Garrison. Thank you so much for all of the time and effort that you put in to these projects. Many thanks to all of my current and former committee members for their input and feedback.

My friends and family have provided an enormous amount of support throughout this process. In particular, thank you to Alyssa Becker for being there with me to celebrate the successes and learn from the failures throughout the course of our research projects. Thank you to the whole Lehigh crew – you never fail to lift my spirits and put a smile on my face. I cannot express in words how grateful I am to my husband, Jerry, who has been a source of unwavering love and support. I am so lucky to have such an amazing partner for all the adventures to come. Last but not least, thank you to my parents and sisters, Caitlin and Christie, for always supporting from the very beginning.

Table of Contents

Chapter 1: Preface

1.1 Abstract

Glioblastoma (GB) is the most common malignant primary brain tumor. Even with aggressive treatment, the median overall survival for GB patients is only 15 months. Furthermore, brain metastases develop in roughly 10-20% of all cancer patients. Development of brain metastases worsens overall prognosis and limits treatment options. Although promising new treatments for both primary and metastatic brain tumors, including gene therapy approaches, are constantly under development, brain neoplasms present tremendous challenges to effective therapeutic delivery.

There are three main physical barriers impede effective delivery of systemically administered agents into brain tumor tissue: 1.) the blood-tumor barrier (BTB) 2.) the blood-brain barrier (BBB) and 3.) the brain tissue barrier. The BTB is formed by leaky tumor vessels that contribute to high interstitial fluid pressures, limiting convective transport of circulating agents into the tissue. Despite areas of high vascular permeability, vessel leakiness varies throughout tumors and blood-brain barrier-like properties are retained within certain regions. Lastly, the transport of agents that have crossed into the brain tumor tissue compartment is limited by steric and adhesive interactions with the extracellular matrix (ECM).

Focused ultrasound (FUS) is a versatile tool that can be used to overcome the major obstacles to effective agent delivery to brain tumors. In this dissertation, we explore two FUS-based techniques for gene delivery applications in brain tumors and investigate the molecular responses to FUS application in brain tumor tissue. First, we develop a multifaceted approach for non-invasive, non-viral transfection of brain tumors. For this method, we apply FUS in the presence of intravascular microbubbles (MBs) to disrupt the blood-tumor/blood-brain barrier (BTB/BBB) and facilitate delivery of non-viral brain-penetrating nanoparticle (BPN) gene

vectors, designed to rapidly penetrate the extracellular space and transfect large tissue volumes. We show that FUS + MB BTB/BBB disruption permits non-invasive delivery of BPNs into brain tumor tissue and results in a roughly 4-fold enhancement in transfection in both a primary and secondary brain tumor model. Furthermore, we identify enhanced convective transport in the tumor interstitium as a potential key mediator of FUS + MB tumor transfection with BPNs. Second, we aim to enhance transfection by utilizing FUS to modulate the tumor tissue interstitial space prior to BPN administration, a technique referred to as FUS preconditioning. Lastly, given the promise of FUS as a therapeutic delivery strategy for brain tumors and the progression of this technique into human clinical trials for patients with brain metastases, we investigate the effects of FUS + MB BTB/BBB opening on the brain tumor microenvironment in an intracranial melanoma tumor model.

1.2 Preview of This Dissertation

In chapter 2 of this dissertation, we will introduce topics related to brain tumors and associated delivery challenges. We review the use of FUS + MB for BBB and BTB disruption, and FUS-mediated delivery of agents to brain tumors. We will also provide a brief overview of studies investigating molecular response to FUS + MB BBB opening in brain tissue. Chapter 3 will discuss the development of a targeted, non-invasive strategy for brain tumor transfection utilizing MRI-guided FUS (MRgFUS) + MB BTB/BBB opening and non-viral brain-penetrating nanoparticle (BPN) gene vectors, as well as insights into possible mechanisms bolstering efficacy of this approach. In chapter 4, we test whether we can use FUS preconditioning of brain tumor tissue prior to FUS + MB BTB/BBB opening enhance BPN-mediated brain tumor transfection. Chapter 5 investigates the effects of FUS + MB BTB/BBB opening in an intracranial melanoma model, with a focus on the acute inflammatory response. Chapter 6 will explore future research questions related to the findings in this dissertation.

Chapter 2: Introduction

This chapter contains excerpts from:

Curley CT, Sheybani ND, Bullock TN, Price RJ. Focused Ultrasound Immunotherapy for Central Nervous System Pathologies: Challenges and Opportunities. Theranostics 2017; 7(15):3608-3623. doi:10.7150/thno.21225.

2.1 Clinical Significance

Brain tumors represent a diverse group of brain neoplasms. Primary brain tumors result from malignant transformation of cells within the brain, while secondary brain tumors arise from metastatic spread from tumors outside of the central nervous system (CNS). Glioblastoma (GB) is the most common malignant primary brain tumor in adults. Despite aggressive standard-of-care therapy, the median overall survival for GB patients is only 15 months(*1*, *2*). Secondary brain tumors are more common and occur in roughly 10-20% of all cancer patients(*3*). Development of brain metastasis signifies worse prognosis and limits treatment options. Promising new treatments for both primary and metastatic brain tumors, including gene therapy and immunotherapy approaches, are constantly under development; however, brain tumors present tremendous challenges to effective therapeutic delivery.

2.2 The Blood-Brain Barrier and Brain Tumors

The blood-brain barrier (BBB) is formed by a continuous layer brain capillary endothelial cells that are connected by tight junctions(*4*). These tight junctions form a barrier to paracellular diffusion of substances from systemic circulation. Proper functioning of the BBB is further supported by interactions between the endothelial cells with basement membranes, pericytes, and astrocytic, forming the neurovascular unit (NVU)(*5*, *6*). Additionally, drug efflux pumps like p-glycoprotein are expressed at the blood-brain barrier, where they work to remove substrates from the CNS(*7*). While the blood-brain barrier serves the essential function of maintaining brain tissue homeostasis and protecting the parenchyma from neurotoxic substances, it is also a major barrier to effective drug development for neurological applications. BBB permeability is limited to small, lipophilic molecules, less than 400 Daltons, that can freely diffuse through the endothelial membrane(*8*). Ultimately, the BBB prevents more than 98% of small molecule drugs and 100% of large molecule therapeutics from entry into brain tissue via systemic circulation(*8*).

The development of tumors within the brain parenchyma disrupts normal vascular structures, yielding a disrupted blood-brain barrier throughout much of the tumor(*9*). Tumor cells secrete angiogenic factors, such as vascular endothelial growth factor (VEGF), leading to the formation of new blood vessels(*10*). These tumor-associated vessels are abnormal in both structure and function, exhibiting large fenestrations and irregular shapes and sizes(*11*). This abnormal vasculature disturbs proper functioning of the BBB throughout much of the brain tumor mass and leads to the formation of the blood-tumor barrier (BTB). The BTB and the BBB with respect to agent delivery to brain tumors will be discussed in the next section.

2.3 Obstacles to Effective Therapeutic Delivery to Brain Tumors

Delivery of systemically administered therapeutics to brain tumors is hindered by three main physical barriers within the tissue, namely the (1) the blood-tumor barrier (BTB) (2) the blood-brain barrier (BBB) and (3) the tissue barrier. First, brain tumor blood vessels make up the blood-tumor barrier (BTB), which is characterized by heterogeneously leaky vessels(*9*). Leaky vessels within the tumor bulk create uniformly high interstitial fluid pressure, which equalizes or reverses the pressure differential between the blood vessels and the tissue, hindering convective transport of agents from the circulation into tissue(*12*). Second, the blood-brain barrier (BBB), which is a significant obstacle to agent delivery in normal brain tissue, also plays a role in limiting delivery to brain tumors. For secondary brain tumors, studies have shown varying vascular permeability between, and even within, single metastatic lesions(*13*). Additionally, delivery of therapeutic agents to brain metastases is significantly lower compared to peripheral metastases, possibly owing to retention of blood-brain barrier-like properties within a subset of vessels(*14*) In glioblastoma (GB), grade IV glioma, tumor cells invade into normal brain tissue where they are supplied by blood vessels with a fully intact BBB and thus shielded from systemic therapeutics(*15*). These invasive cells are left behind following surgical resection

and facilitate tumor recurrence after standard treatment(*16*). Therefore, overcoming the BBB around the invasive edges of GB and increasing permeability within brain lesions will be a crucial feature of successful treatment strategies. Third, the adhesive and nanoporous extracellular matrix (ECM) limits distribution of agents within the tissue(*17*). Brain ECM is composed of negatively charged glycosaminoglycans and proteoglycans, which can hinder tissue distribution of agents via charge interactions. Furthermore, brain tumors have increased volume fraction of ECM and tortuosity of extracellular space compared to normal brain tissue, which can further obstruct agent movement and dispersal(*17*). It is possible that insufficient delivery and distribution of therapeutics within brain tumor tissue has contributed to the failure of many therapeutic approaches; therefore, it is crucial to design therapeutic strategies to overcome these obstacles.

2.4 Drug Delivery to Brain Tumors

2.4.1 Local Drug Delivery Methods

Given the dismal prognosis for patients with primary and metastatic brain tumors, numerous methods have been devised to overcome obstacles to brain tumor therapeutic delivery. One type of approach is the direct application of therapeutics to the tumor or into the tumor resection cavity, which circumvents the BTB/BBB by avoiding vascular delivery. For example, drug loaded polymer wafers, such as Gliadel, can be implanted into the tumor resection cavity and provide a mild survival benefit(*18*–*20*). Still, penetration of the drug from the implant and into surrounding tissue is restricted and may contribute to limited efficacy of this technique(*21*). Convection-enhanced delivery (CED) is a method that has specifically been developed to enhance drug distribution in the tissue compared to traditional injection approaches. This technique uses bulk flow to distribute agents reproducibly and homogenously throughout larger tissue volumes(*22*). Despite preclinical efficacy, CED injections have limited

success in clinical trials for treatment of brain tumor patients(*23*). An additional drawback to local delivery methods is that the invasive nature of the procedures precludes its use with drugs requiring multiple doses.

2.4.2 Methods for Systemic Drug Delivery

Noninvasive methods that have been established for delivery of agents across the BBB include osmotic BBB disruption, bradykinin-like agents, and receptor targeted nanoparticles; however, these methods have a number of disadvantages. Osmotic BBB disruption is achieved by intra-arterial administration of a hypertonic solution, such as mannitol(*24*). This results in shrinking of endothelial cells and physical disruption of tight junctions, which allows for paracellular transport of agents into the tissue(*25*). This method, however, is complex and has associated toxicities due to widespread BBB disruption(*26*). Pharmacological BBB disruption with bradykinin-like molecules also yield disruption of tight junctions, however, these agents have failed to demonstrate therapeutic benefit in clinical trials when used in combination with brain tumor therapies(*27*). Lastly, various nanoparticle formulations have been conjugated to ligands to facilitate receptor-mediated entry into brain tissue(*28*). While agents targeting receptors, such as transferrin and folate receptors, can deliver agents across the BBB, the fraction of the administered dose that reaches the brain is low.

2.5 Focused Ultrasound for Blood-Brain and Blood-Tumor Barrier Disruption

Focused ultrasound (FUS) activation of circulating microbubbles (MBs) is now an established method for enhanced therapeutic delivery to normal and diseased brain tissues that offers numerous advantages over the methods discussed above. For BBB opening, ultrasound is applied transcranially and focused into a small region of high energy deposition within the targeted brain region. Thus, FUS + MB BBB opening is completely non-invasive and localized to

the FUS focal zone. This technique is widely used in conjunction with magnetic resonance imaging (MRI), allowing for precise spatial targeting and confirmation of successful BBB opening. In preclinical models, FUS + MB BBB opening has proven to be safe, reversible, and able to deliver a wide range of therapeutic and imaging agents. Several clinical trials have been completed or are underway and include use in patients with Alzheimer's disease, ALS, and brain tumors(*29*–*31*).

2.5.1 Mechanism of FUS-Mediated BTB/BBB Disruption

FUS + MB-mediated BTB and BBB opening occurs due to expansion and contraction of microbubbles within blood vessels of the targeted tissue volume. Bubbles in the ultrasound field can oscillate in either a stable or inertial manner, depending upon the applied pressure amplitude. Inertial cavitation occurs when oscillations lose stability and ultimately lead to rapid, violent bubble collapse(*32*). This can yield a highly localized rise in temperature, acoustic streaming, and shock wave formation, and is associated with tissue damage(*33*). Safe and reproducible BBB/BTB opening with FUS and microbubbles is attributed to stable cavitation, which is a more predictable mode in which bubbles steadily oscillate in size to produce mechanical shear forces, as well as circumferential stresses, on microvessel walls(*34*). In normal brain tissue, this has been shown to yield transient tight junction opening, vascular endothelial sonoporation, and enhanced transcytotic capabilities spanning an estimated 4-6 hour period over which the BBB is open(*35*–*37*). Furthermore, FUS + MB BBB disruption induces decreased expression of P-glycoprotein, a major BBB drug efflux pump, for up to 72 hours in sonicated brain tissue(*38*).

While FUS + MB-mediated permeabilization of the brain tumor vasculature likely shares many features with BBB disruption in normal brain, only a small number of studies have specifically investigated mechanisms involved in FUS BTB opening. FUS + MB application in a

rat C6 glioma model was found to increase pinocytic vessel density in glioma microvessels. This was accompanied by increased mRNA and protein expression of caveolin-1 and caveolin-2, implicating increased transcellular vesicle transport and BTB permeabilization(*39*). FUS + MB BTB opening in a breast cancer brain metastasis model was demonstrated to enhance delivery and penetration of doxorubicin and an antibody drug conjugate. Using physiologically based pharmacokinetic models and high resolution imaging techniques, the investigators concluded that a shift from diffusion-dominated to convection-dominated transport facilitated enhanced delivery and penetration of the tested therapeutics into tumor tissue(*40*). Despite the general lack of mechanistic studies of FUS + MB BTB/BBB opening in brain tumors, it is apparent that this technique does in fact enhance delivery of a wide range of therapeutic molecules to brain tumor tissue. Preclinical studies utilizing this approach for drug and gene delivery to intracranial tumors will be discussed in forthcoming sections.

2.5.2 Passive Cavitation Detection for Monitoring and Control of BTB/BBB Opening

To enhance safety and reproducibility of FUS + MB BTB/BBB opening, methods of acoustic monitoring and feedback control mechanisms have been widely developed and implemented. As discussed above, FUS activation of microbubbles can produce safe BBB opening or induce tissue damage depending upon production of either stable or inertial cavitation of intravascular microbubbles. Passive cavitation detection (PCD) permits monitoring of bubble cavitation behavior in real time by quantifying hallmarks of stable cavitation (harmonic, subharmonic, and ultraharmonic emissions) and inertial cavitation (broadband noise). Active feedback control mechanisms have been developed and applied successfully in both normal brain and brain tumor tissue to achieve levels of stable cavitation sufficient for BTB/BBB opening but well below the threshold for tissue damaging levels of inertial cavitation. For instance, one group has developed a closed-loop control system that enabled delivery of higher

doxorubicin doses (liposomal doxorubicin) to 9L gliosarcoma than in their previous work, and maintained safe exposure levels throughout treatment(*41*). Similar results have been reported in an F98 glioma model, in which feedback control allowed for safe delivery of carboplatin at levels that reduced tumor growth and increased median overall survival(*42*).

2.6 Drug delivery to Brain Tumors with FUS + MB BTB/BBB Opening

2.6.1 Free Chemotherapeutics

FUS + MB BTB/BBB opening has been used for delivery of a wide range of chemotherapeutics. Temozolomide (TMZ), an oral alkylating agent, is currently part of the aggressive standard-of-care treatment protocol for GB; therefore studies have investigated whether FUS can improve its delivery and efficacy(*43*). In a 9L gliosarcoma model, FUS + MB BTB/BBB disruption increased the cerebrospinal fluid (CSF)/plasma ratio and modestly improved treatment outcomes, including progression ratio and median survival time(*44*). Similar results were also obtained in U87 xenografts, in which investigators noted a roughly 2.7-fold increase in TMZ concentration within tumor tissue. FUS + MB BTB/BBB opening did confer therapeutic benefit over TMZ alone, but this effect was dose-dependent and more pronounced at lower TMZ doses(*45*). In syngeneic mouse models of GBM, FUS + MB facilitated enhanced delivery of doxorubicin, conferring a survival benefit and slower disease progression compared to doxorubicin alone(*46*). In a 9L model intratumoral concentrations of doxorubicin were enhanced in FUS + MB treated tumors compared to doxorubicin alone at both 1 and 24 hours post-treatment, indicating enhanced retention of the drug within tumor tissue(*47*). Using microdialysis to measure intratumoral doxorubicin concentration over time, FUS + MB BTB/BBB opening increased drug concentration roughly 10-fold over control tumors at peak concentration, which occurred roughly 45 minutes following treatment, followed by a rapid decline(*48*). Furthermore, in addition to increased doxorubicin delivery (roughly seven-fold),

FUS + MB BTB/BBB enhanced tissue penetration of the drug in HER2-positve breast tumor brain metastasis. Similarly, FUS has also been shown to enhance delivery of bis-chloroethylnitrosourea (BCNU) and carboplatin to brain tumors(*42*, *49*).

2.6.2 Encapsulated Drugs

Encapsulation within or conjugation to delivery agents can allow for more precise targeting of drugs to diseased tissue, thereby limiting systemic toxicity. To this end, FUS has been used in combination with several formulations of chemotherapeutic loaded liposomes, nanoparticles, and microbubbles to further improve drug targeting and treatment of brain tumors. Numerous studies have utilized FUS + MB for enhanced delivery and efficacy of liposomal doxorubicin(*40*, *41*, *50–57*). Increased doxorubicin concentrations and a modest survival benefit was achieved with a single FUS + MB + liposomal doxorubicin treatment. Later studies revealed that efficacy was greatly improved with 3 treatments per week, although signs of toxicity were seen in some of these animals. FUS-mediated delivery of cisplatin-loaded polymeric nanoparticles to orthotopic F98 tumors decreased tumor invasiveness, slowed growth, and improved survival(*56*). Furthermore, advanced theranostic agents can be used in combination with FUS for delivery to brain tumors. For instance, superparamagnetic iron oxide (SPIO)-Doxorubicin (DOX)-conjugated MBs facilitated simultaneous MR imaging of the FUS-mediated particle delivery and release of the chemotherapeutic drug via magnetic targeting(*57*).

2.6.3 Antibodies

Focused ultrasound has also been used for delivery of anti-cancer antibodies in studies aimed at establishing experimental therapeutic efficacy for treating intracranial tumors. For example, the efficacy of HER-2 targeting antibody delivery with FUS has been tested in a brain tumor metastasis model of HER-2 positive breast cancer. In this study, some animals received

no treatment, while treatment groups included the HER-2 receptor targeting antibodies, trastuzumab and pertuzumab, intravenously (i.v.) administered with or without FUS-mediated BTB/BBB opening weekly for a 6-week period of time. A subset of animals in the FUS + antibody group were classified as responders, characterized by a slower tumor growth rate, while there were no responders in the antibody-only group. There was increased survival in the FUS + antibody and antibody only groups compared to untreated animals, but no statistically significant difference between these two groups. No differences were seen between the responders and non-responders by the parameters measured in this study, but elucidating the determining factors between these two groups will likely be important if this approach will ever be translated to the clinic(*58*). FUS has also been used for delivery of the anti-VEGFA monoclonal antibody, bevacizumab, in an intracranial glioma xenograft model. Weekly treatments with FUS, microbubbles, and bevacizumab resulted in decreased tumor growth, increased median overall survival, and decreased vessel area compared to untreated, FUS-only, and bevacizumab-only groups(*59*). Lastly, FUS + MB BTB/BBB disruption in a model of breast cancer brain metastasis increased delivery of the antibody-drug conjugate ado-trastuzumab emtansine (TDM-1) two-fold, and resulted in enhanced tissue penetration of this agent(*40*).

2.6.4 Immunomodulatory Agents

Immunomodulatory agents such as cytokines and targeted immune cells have been delivered via FUS-mediated BTB/BBB opening for treatment of brain tumors. Intraperitoneal administration of interleukin-12 (IL-12) followed by application of FUS and microbubbles resulted in an approximately three-fold increase in IL-12 in an orthotopic glioma model compared to untreated control mice, whereas mice receiving IL-12 without FUS had a roughly two-fold increase. Enhanced delivery of IL-12 with FUS generated the highest CD8+/T-reg ratio, slowed

tumor progression, and the greatest survival benefit(*60*). NK-92 cells are a human natural killer cell line that can be modified to target tumor associated antigens, such as HER-2. In an intracranial model of HER2-positive breast cancer metastasis, FUS administration generated a 10-fold increase in HER2-specific NK-92 cell abundance in the FUS-targeted region after i.v. NK-92 injection when compared to i.v. NK-92 injection without FUS(*61*). With an aggressive treatment regimen consisting of five treatments in the first week, two in the second week, and one in the third week, animals in the FUS + NK-92 group showed a reduction in tumor growth and increase in survival compared to controls(*62*). Taken together, the studies reviewed here demonstrate that FUS is a versatile tool that facilitates delivery of chemotherapeutic based agents, antibodies, and immunomodulatory agents to brain tissue tumors.

2.7 Gene Delivery to Brain Tissue and Brain Tumors with FUS + MB BTB/BBB Opening

For gene delivery to brain and brain tumor tissue, FUS + MBs has been combined with both viral and non-viral gene vectors(*63*–*79*). Adeno-associated virus (AAV) is the most widely used method of viral transfection, whereas a number of different non-viral vectors have been tested, including liposomes, microbubble-plasmid conjugates, and nanoparticles.

2.7.1 Viral Methods for FUS-Mediated Brain Tissue Transfection

Viral methods have mainly utilized AAV vectors to facilitate expression of reporter genes such as LacZ and GFP in the FUS-targeted brain region(*63*, *64*, *72*, *73*, *75*). While some studies reported expression in both neurons and glial cells, use of the synapsin promoter enabled neuron-specific gene expression(*75*)(*63*). Beyond reporter genes, FUS delivery of AAV vectors has been used for delivery of α-synuclein targeted shRNA plasmids, which was able to reduce α-synuclein protein levels in targeted brain regions of transgenic mice(*74*). FUS + MB delivery of

AAV-GDNF (glial derived neurotrophic factor) gene vectors was able to increase dopaminergic neurons and exhibited signs of improved behavioral outcomes in the MPTP mouse model of Parkinson's disease(*70*). Lastly, FUS + MB AAV mediated gene delivery of the light-sensitive protein Channelrhodopsin-2 (ChR2) gene provides proof-of-concept for using FUS as a tool for optogenetics(*71*).

2.7.2 Non-Viral Methods for FUS-Mediated Brain Tissue Transfection

Non-viral methods for FUS-mediated gene delivery include liposomes, bubble-conjugated liposomes, targeted and non-targeted cationic bubble-plasmid conjugates, and polymeric nanoparticles. FUS + MB BBB opening facilitated luciferase and GDNF gene delivery via plasmid containing liposomes(*80*). This group was able to improve upon their GDNF gene delivery system and achieve therapeutic efficacy in an MPTP model of Parkinson's disease by conjugating the plasmid liposomes to microbubbles(*79*). FUS + MB BBB opening in the presence of i.v. plasmid-cationic microbubble conjugates have similarly been demonstrated to have superior transfection capability compared to FUS activation of conventional microbubbles and free plasmid DNA(*69*). Additional variations on these non-viral delivery agents include bubble liposomes and nanomicrobubbles, both of which have been used in combination with FUS + MB BBB opening for gene delivery to the brain(*81*, *82*). Our group has previously developed a non-viral approach for brain tissue transfection via FUS + MB-mediated delivery of polymeric brain-penetrating nanoparticles (BPNs), as will be discussed in forthcoming sections(*83*).

2.7.3 Methods of FUS-Mediated Brain Tumor Transfection

There are a small number of studies that have demonstrated FUS-mediated gene delivery to intracranial C6 glioma tumors, using both viral and non-viral gene vectors. FUS + MB

BTB/BBB opening facilitated delivery of an Adenovirus vector for expression of the thymidine kinase gene and resulted in increased survival with the application the prodrug ganciclovir(*84*). FUS applied in the presence of folate conjugated DNA-loaded cationic microbubbles for delivery of luciferase reporter gene resulted in a 4.7-fold increase in expression compared to direct injection of the plasmid in C6 intracranial tumors(*77*). Additionally, the folate component facilitated uptake and expression, with a 1.5-fold increase in expression when using folate containing microbubbles(*77*). VEGFR2-targeted cationic bubble-plasmid conjugates were used for delivery of luciferase reporter genes as well as thymidine kinase therapeutic gene. This delivery system yielded significantly increased median survival compared to gene delivery via direct injection(*65*). Lastly, FUS utilized with an shRNA liposome complex conjugated to microbubbles was able to silence the targeted gene, decreasing tumor growth and increasing median overall survival(*66*).

2.7.4 FUS + MB BBB Opening for Delivery of Non-Viral Brain-Penetrating Nanoparticles

Our group has previously developed a non-viral gene delivery approach for transfection of brain tissue using focused ultrasound and polymeric “brain-penetrating” nanoparticle (BPN) gene vectors(*83*, *85*, *86*). BPNs are non-viral gene vectors designed to maximize distribution in brain tissue, and thus offer many advantages over other gene carriers. Generally, polymeric non-viral gene vectors have an increased loading capacity, lower cost, and greater ability to tailor physiochemical properties than viral gene carriers. Additionally, non-viral vectors alleviate concerns of pre-existing immunity to naturally occurring viral vectors that could reduce efficacy, as well as safety issues. Furthermore, the dense polyethylene glycol (PEG) coating on our brain-penetrating non-viral gene vectors facilitates increased spreading in brain tissue compared to conventionally PEGylated nanoparticles, resulting in enhanced vector distribution and transfection volume in both healthy brain and brain tumor tissues(*85*, *87*). We have demonstrated

safety and efficacy of this FUS-mediated BPN delivery for transfection of normal brain tissue(*83*). We have also proven therapeutic efficacy in a rat model of Parkinson's disease (PD), in which we were able to achieve durable and therapeutic levels of GDNF transgene expression, thereby leading to restored dopamine levels and dopaminergic neuron content, and reversed behavioral indicators of PD-associated motor dysfunction(*86*). In chapter 3 of this dissertation, we develop this gene delivery approach for use in primary and secondary brain tumor models and investigate several key factors in delivery and transfection.

2.8 FUS Modulation of the Tissue Interstitial Space

Ultrasound has been shown to have effects on brain tissue that can enhance dispersion of agents within the extracellular space, both with and without intravascular microbubbles. Ultrasound application to *ex vivo* brain slices yielded increases in extracellular and perivascular spaces measured by TEM imaging, and increased movement of subsequently injected nanoparticles(*88*). Additionally, transcranial FUS applied to rat brains immediately prior to injection of non-adhesive nanoparticles significantly increased distribution in the tissue(*89*). Furthermore, it has been demonstrated that application of ultrasound to brain tissue with intravascular microbubbles prior to injection of AAV-GFP vectors produced a 3-fold increase in transfection volume(*90*). There has also been evidence that FUS modulation of tumor extracellular space can contribute to favorable delivery and distribution of agents in the tissue. Pulsed-high intensity focused ultrasound (HIFU) significantly increased uptake, penetration, and efficacy of an intravenously administered monoclonal antibody therapeutic in a flank tumor xenograft model(*91*, *92*). In a different study, pulsed HIFU application improved delivery of systemically administered chitosan nanoparticles increased roughly 2.5-fold, enhanced nanoparticle penetration, and was associated with increased blood flow, ECM remodeling, and

decreased collagen content in flank tumor xenografts(*93*). Further, application of pulsed FUS in flank tumors prior to direct injection of naked plasmid DNA increased uptake(*94*).

We recently demonstrated an increase in BPN-mediated transfection with application of FUS prior to direct injection of the nanoparticles by convection-enhanced delivery (CED) in rat brain tissue(*95*). Given this result, we then developed an ultrasound preconditioning approach in which FUS was applied (in the absence of microbubbles) to the targeted tissue prior to FUS + MB-mediated delivery of reporter gene-BPNs across the BBB. FUS pre-conditioning followed by FUS + MB BBB opening resulted in a 5-fold enhancement in reporter gene transfection compared to BBB opening alone. Our results suggested that the achieved increase in transfection is due to modulation of the brain parenchyma rather than modulation of subsequent BBB opening. This study established that FUS preconditioning is a safe and effective method for enhancing FUS-mediated transfection of brain tissue using non-viral gene vectors(*95*). Chapter 4 of this dissertation will explore the use of FUS preconditioning prior to FUS + MB BTB/BBB opening for intracranial tumor transfection.

2.9 FUS Immunomodulatory Effects in the Brain

Most studies of FUS-mediated BBB opening have focused on using this approach to deliver therapeutic agents to the brain; however, it has also come to be appreciated that the procedure itself may exert some immune-related effects. In particular, two different studies have evaluated the molecular effects of focused ultrasound BBB opening in rat brains. The first profiled changes in RNA and protein expression at acute time points following FUS BBB opening. Here, increases in both HSP70 and proinflammatory cytokines were measured within 24 hours. An increase in ionized calcium binding adaptor molecule 1 (Iba1) was also reported, indicating microglial activation, and macrophages from the periphery were found in the sonicated region at six days post-treatment(*96*). Previously, macrophages had only been detected in the brain after

sonicating at higher pressures that induced intracerebral hemorrhage; however, it should be noted that their analysis was limited to 24 hours following FUS(*97*). The second study looked more specifically at RNA expression in brain endothelial cells following FUS-mediated BBB opening. At six hours post sonication, there was an upregulation of pro-inflammatory chemokine and cytokine genes and a downregulation of BBB related transporter genes, which mostly returned to baseline by 24 hours(*98*). Both studies found increases in glial fibrillary acidic protein (GFAP) indicative of astrocyte activation.

Interestingly, FUS-mediated opening of the BBB with microbubbles, independent of the delivery of a drug and/or therapeutic gene, exerts beneficial effects in mouse models of Alzheimer's disease. Indeed, ultrasound treatment has shown reduced plaque load in two studies utilizing different transgenic mouse models(*99*, *100*). In both studies, the treated region displayed increased markers of microglial activation and greater localization of amyloid beta (Aβ) within microglia, suggesting that ultrasound was able to facilitate phagocytic uptake of Aβ, thereby aiding plaque clearance. In the APP23 model, functional tests indicated memory restoration in treated mice(*99*). A phase one clinical trial has been completed in Alzheimer's patients, demonstrating safety and feasibility of FUS and microbubble BBB opening this population(*29*).

One study has also demonstrated that FUS and microbubble application in brain tumors has immunomodulatory effects. Glioma tumors receiving three FUS treatments over a period of 5 days exhibited an increase in the CD8+/T-reg ratio, a metric commonly correlated with improved patient outcome(*60*). Beyond this study, there is currently a gap in knowledge about how FUS + MB BTB/BBB opening alters the brain tumor immune microenvironment. Given the current progression of FUS + MB BTB/BBB opening into clinical trials for patients with metastatic brain tumors and the appeal of using this approach in combination with traditional and immune based therapies, it is crucial to understand how this FUS-mediated BTB/BBB opening modulates the brain tumor tissue at a molecular level. Chapter 5 of this dissertation aims to uncover the effects

of FUS + MB BTB/BBB on the immune microenvironment in a model of melanoma brain metastasis.

2.10 The Cancer Immunity Cycle and the Role of Dendritic Cells in Anti-Tumor Immunity

The findings in chapter 5 will be discussed in the context of generation of an anti-tumor immune response; therefore, the tumor immunity cycle and the role of dendritic cells in this process will be briefly reviewed in this section.

2.10.1 Cancer Immunity Cycle

To generate an antitumor immune response, first tumor neoantigens are released from the tumor and captured by antigen-presenting cells (APCs), primarily dendritic cells (DCs). Additional immunogenic signals, such as proinflammatory cytokines, pathogen-associated molecular patterns (PAMPs), and damage-associated molecular patterns (DAMPs), are required to activate dendritic cells for productive interactions with T cells. Absence of these signals generates tolerance. Dendritic cells can then present these antigens via major histocompatibility (MHC) class I or class II molecules to T cells, normally in the tumor draining lymph node. Mature dendritic cells prime T cells that are specific for the presented antigens, thereby generating effector T cells precisely targeted for tumor antigens. These activated T cells can then traffic to the tumor site, where they recognize their cognate antigen on the MHC I molecules of tumor cells and kill the target cells. Tumor cell killing by cytotoxic T cells releases additional antigens which can support further T cell activation. In an established tumor, mechanisms have developed to disrupt this process and allow the tumor to escape immune detection(*101*). Ultimately, in chapter 5 of this dissertation, we discuss the effects of FUS + MB BTB/BBB opening on intracranial melanoma tumors in terms of how FUS-induced alteration of the tumor microenvironment could

interface with several steps of the cancer immunity cycle, namely antigen capture and presentation, APC priming of T cells, and T cell trafficking and infiltration.

2.10.2 The Role of Dendritic Cells in Anti-Tumor Immunity

In Chapter 5 of this dissertation, much of the discussion revolves around the dendritic cell (DC) population. As discussed above, DCs are professional antigen-presenting cells and act as a bridge between the innate and adaptive immune system. Dendritic cells in peripheral tissue exist in an immature form, in which they primarily endocytose materials and accumulate antigens. Immature DCs are poor antigen presenters and may even contribute to tolerance. Molecules such as PAMPs and DAMPs activate pattern recognition receptors on dendritic cells, providing a maturation stimulus. Upon maturation, DCs downregulate endocytosis and activate machinery involved in antigen processing and presentation. Generation of MHC-peptide complexes becomes more efficient and these molecules have increased stability on the cell surface. Furthermore, DCs upregulate chemokine receptors such as CCR7, inducing migration to lymph nodes. Lastly, the expression of T cell costimulatory molecules and immunostimulatory cytokines are increased in the DCs, equipping them for activation of T cells(*102*).

Chapter 3: Augmentation of Brain Tumor Interstitial Flow via Focused Ultrasound Promotes Brain-Penetrating Nanoparticle Dispersion and Transfection

Colleen T. Curley, Brian P. Mead, Karina Negron, Namho Kim, William J. Garrison, G. Wilson Miller, Kathryn M. Kingsmore, Jennifer M. Munson, Ji Song, E. Andrew Thim, Alexander Klibanov, Jung Soo Suk, Justin Hanes, and Richard J. Price

3.1 Abstract

The delivery of systemically administered gene therapies to brain tumors is exceptionally difficult due to the blood-brain (BBB) and blood-tumor (BTB) barriers. Additionally, the adhesive and nanoporous tumor extracellular matrix hinders therapeutic dispersion. Here, we first developed the use of magnetic resonance (MR) image-guided focused ultrasound (FUS) and microbubbles (MBs) as a platform approach for transfecting brain tumors by targeting the delivery of systemically administered “brain-penetrating” nanoparticle (BPN) gene vectors across the BTB/BBB. Next, using an MRI-based transport analysis, we determined that, after FUS-mediated BTB/BBB opening, mean interstitial flow velocity magnitude doubled, with “per voxel” flow directions changing by an average of 60º. Finally, we observed that FUS-mediated BTB/BBB opening elicited a >100% increase in the dispersion of directly injected BPN through tumor tissue. We conclude that FUS-mediated BTB/BBB opening yields markedly augmented interstitial tumor flow that, in turn, plays a critical role in enhancing BPN transport through tumor tissue.

3.2 Introduction

Glioblastoma (GB) is the most common malignant primary brain tumor. Even with aggressive treatment, the median overall survival for GB patients is only 15 months(*1*, *2*). Further, brain metastases develop in roughly 10-20% of all cancer patients(*3*). Promising new treatments for both primary and metastatic brain tumors, including gene therapy approaches, are constantly under development; however, brain neoplasms present tremendous challenges to effective therapeutic delivery. Indeed, the delivery of systemically administered gene therapies to brain tumors is impeded by significant physical barriers(*103*). First, while blood vessels within both primary and metastatic tumors may be leaky, this feature creates high interstitial fluid pressures that hinder convective transport of systemically administered gene therapies from the bloodstream and into the tissue(*9*, *12*). This is referred to as the blood-tumor barrier (BTB)(*9*). Second, when considering GB specifically, the blood-brain barrier (BBB) becomes a large obstacle to effective treatment because tumor cells invade into surrounding healthy tissue where the BBB remains intact(*8*, *15*). Lastly, the transport of agents that have crossed into the brain tumor tissue compartment is limited by steric and adhesive interactions with the extracellular matrix(*17*).

Magnetic Resonance Image (MRI)-guided focused ultrasound (FUS) with circulating microbubbles (MBs) is a non-invasive approach for safe and reversible opening of the BTB and BBB. Indeed, it is now well-known that FUS application in the presence of intravascular MBs increases vascular permeability, which facilitates the delivery of systemically administered agents into brain tissue(*35*, *36*, *104*). Clinical trials utilizing FUS and MBs for BTB/BBB opening for Alzheimer's disease and brain tumors(*29*, *31*) have been performed, with many others planned or underway. Preclinical work has established BTB/BBB opening with FUS and MBs as an effective method of delivery for antibodies, chemotherapies, and nanoparticles in both normal and diseased brain tissue(*53*, *56*, *83*, *86*, *105–108*). For gene delivery, FUS + MBs has

been combined with both viral and non-viral gene vectors. Viral methods have mainly utilized AAV vectors, while non-viral methods include bubble-conjugated liposomes, as well as targeted and non-targeted cationic bubble-plasmid conjugates(*63*, *65–67*, *74*, *77*, *78*). Our group has previously developed a non-viral gene delivery approach for transfection of brain tissue using focused ultrasound and polymeric "brain-penetrating" nanoparticle (BPN) gene vectors, an approach that may offer advantages over other methods (*83*, *85*, *86*). The first major component of this study entailed testing whether combining MR image-guided FUS + MB-mediated BTB/BBB opening with BPN could elicit effective targeted brain tumor transfection.

The second major component of this investigation entailed determining how FUS + MB-mediated BTB/BBB opening affects both tumor interstitial fluid flow and BPN transport through tumor tissue. Because abnormal tumor vasculature contributes to high interstitial fluid pressure, pressure gradients across vessel walls are normally minimized, thereby limiting convective transport(*9*, *12*). However, recent evidence indicates that FUS + MB-mediated BTB/BBB opening could, in addition to augmenting the delivery of agents across the BTB/BBB, improve the penetration of therapeutics through both normal brain(*90*) and tumor tissue(*40*). To examine whether BTB/BBB opening with FUS and MBs affects interstitial transport in models of GB and brain metastases, we analyzed the spatiotemporal evolution of gadolinium transport via examination of a timed series of T1 contrast-enhanced MR images(*109*). Next, after establishing how FUS + MB-mediated BTB/BBB opening affects interstitial transport, we used a convection-enhanced delivery (CED) approach to assess the relative influence of BTB/BBB opening on BPN delivery versus its influence on BPN transport through tumor tissue. In summary, our results indicate that BTB/BBB opening with FUS and MBs does indeed facilitate brain tumor transfection with BPN and provide evidence that a significant component of tumor transfection may be attributed to the augmented convective transport of BPN through the interstitial space.

3.3 Results

3.3.1 Focused Ultrasound and Microbubbles Facilitates the Delivery of Brain-Penetrating Nanoparticles Across the Blood-Tumor/Blood-Brain Barriers.

We first tested whether the activation of MBs with FUS could target the delivery of systemically administered BPN to primary brain tumors under MR image-guidance. Luciferase plasmid-bearing-BPN (Luc-BPN) made with Cy5-labeled plasmid DNA (particle diameters of ~50 nm) were i.v. injected into athymic nude mice with U87mg brain tumors. The BTB/BBB was opened in and around tumors via MB activation with 1 MHz pulsed FUS (0.45 MPa and 0.55 MPa PNP; measured in water), applied in an 8-spot grid. Acoustic emissions were assessed by passive cavitation detection during BTB/BBB opening. Roughly 6 hours following treatment, whole brain and tumor samples from each animal were imaged for Cy5 fluorescence. Representative fluorescent images are shown in Figures 1A (whole brain) and 1B (dissected tumor). For whole brain images, fluorescence was measured using an ROI drawn to encompass the entire FUS-treated region, thus measuring delivery to the tumor and surrounding tissue. Quantification from whole brain samples (Figure 1C) showed significant increases in Cy5 signal in 0.45 MPa and 0.55 MPa FUS+MB treated brains compared to those receiving only an intravenous injection of BPN and MBs. Quantification of Cy5 signal from tumor samples (Figure 1D) showed a significant increase in the 0.55 MPa treatment group compared to BPN only. The 0.45 MPa group showed a trend towards an increase over BPN only, however this was not statistically significant. Figure 1E-G show confocal images of tumor tissue sections with the cy5-BPN signal is shown in red with and tumor microvessels (BS-I Lectin) shown in green. Figure 1G shows enhanced delivery and penetration of cy5-BPN into tumor tissue with 0.45 MPa FUS, in comparison to tumors receiving no treatment and cy5 BPN only, seen in Figure 1E and 1F, respectively. Acoustic emissions at the sub-harmonic (Figure 1H), 2nd harmonic (Figure 1I), and

3rd harmonic (Figure 1J) were all significantly higher with 0.55 MPa FUS when compared to 0.45 MPa FUS. There were no differences in inertial cavitation at the two pressures (1K).

3.3.2 Brain-Penetrating Nanoparticle-Mediated Transgene Expression is Markedly Enhanced in Brain Tumors Treated with Focused Ultrasound and Microbubbles.

We next tested whether BPN that had been delivered across the BTB/BBB with FUS and MBs were able to elicit significant tumor transgene expression. Luc-BPN were injected i.v. immediately prior to FUS + MB BTB/BBB opening of U87mCherry and B16F1cOVA brain tumors. Luciferase transgene expression was analyzed using *ex vivo* bioluminescence imaging of tumors 3 days post-treatment. Representative *ex vivo* bioluminescence images of U87mCherry tumors are shown in Figure 2A. In addition to the standard total flux bioluminescence measurement, average radiance was also quantified to ameliorate any possible influence of tumor size variability on transgene expression measurements. In both the U87mCherry and B16F1cOVA tumor models, FUS + MB BTB/BBB opening elicited significant ~4-fold increases in both total flux and average radiance compared to mice receiving i.v. Luc-BPN alone (Figure 2B-2E). There were no differences in either total flux or average radiance between the 0.45 MPa and 0.55 MPa PNP FUS groups.

3.3.3 Interstitial Fluid Transport in Brain Tumors is Augmented by the Application of Focused Ultrasound and Microbubbles.

For a subset of mice [n=4 per group x 2 tumor types (U87 mCherry and B16F1cOVA) x 2 PNPs (0.45 MPa and 0.55 MPa) = 16 total], we utilized MRI to analyze the effect of BTB/BBB opening with FUS and MBs on gadolinium transport, both to and within, U87mCherry and B16F1cOVA intracranial tumors(*109*). To first assess BTB/BBB disruption following FUS + MB treatment,

mean grayscale intensity was calculated from pre-FUS and post-FUS T1-weighted contrast enhanced MR images [Figures 3A (U87) and 3D (B16F1cOVA)]. Tumors were visible in the pre-FUS images via gadolinium leakage from tumor vessels, which allowed MR image-targeting of the treatment. Contrast enhancement was apparent in all post-FUS MR images, indicating successful disruption of the BTB/BBB. As expected, mean grayscale intensity within tumors (i.e. ROI referred to as “BTB” and defined by enhancing region in pre-FUS image) significantly increased following FUS + MB treatment, as shown in Figure 3B for U87 tumors and Figure 3E for B16F1cOVA tumors. Additionally, there was a significant increase in mean grayscale intensity in the entire FUS-treated region (i.e. ROI referred to as “BTB+BBB” and defined by enhancing region in the post-FUS image) in U87 and B16F1cOVA tumors (Figure 3C and 3F). Of note, opening the BTB/BBB with 0.55 MPa PNP FUS did not confer a detectable increase in contrast enhancement when compared to 0.45 MPa PNP FUS.

Pre- and Post-FUS T1–weighted contrast enhanced MR image sequences were then used to assess changes in interstitial fluid flow and diffusion. Representative MR imaging series in the U87mCherry tumor model are shown in Figure 4A. These images were input into the post-processing algorithm and an ROI in each animal was chosen to encompass the tumor and a portion of surrounding brain tissue. The algorithm solves for maps of flow velocity magnitude and direction, as well as diffusion coefficient. Figure 4B illustrates pre- and post-FUS flow velocity magnitude maps obtained from the imaging series. Flow velocities are plotted for each voxel within the selected ROI in Figure 4C, showing a shift towards a higher velocity magnitude following FUS BTB/BBB opening in this tumor. Data from all animals showed a roughly two-fold increase in mean flow velocity magnitude following BTB/BBB opening with FUS and MBs at both 0.45 MPa and 0.55 MPa PNPs (Figures 4D). In U87mCherry tumors, intravoxel velocity direction changed by about 60 degrees on average following BTB/BBB opening at both tested FUS pressures (Figure 4E, F, G). For the B16F1cOVA model, representative T1-weighted MR images, flow velocity magnitude maps, and flow velocity voxel plots are shown in Figure 5A, 5B,

and 5C respectively. We found a roughly two-fold increase in mean flow velocity magnitude at both FUS pressures (Figure 5D). In B16F1cOVA tumors, intravoxel velocity direction changed by about 70-80 degrees on average following BTB/BBB opening at both tested FUS pressures (Figure 5E, F, G).

3.3.4 Blood-Tumor Barrier Opening with Focused Ultrasound and Microbubbles Augments Brain-Penetrating Nanoparticle Dispersion Through Brain Tumors.

Finally, we tested whether modulation of interstitial flow with FUS and MBs during BTB/BBB opening could significantly affect BPN dispersion through brain tumor tissue. To this end, we performed FUS + MB-mediated BTB/BBB opening in intracranial U87mCherry tumors immediately prior to the convection-enhanced delivery (CED) of BPN bearing the ZsGreen reporter gene (i.e. ZsGreen BPN). Representative images showing ZsGreen transfection volume in the CED only and FUS + MB BTB/BBB + CED groups are shown in Figure 6A. We found a roughly 2-fold enhancement in transfection volume in tumors treated with FUS + MB BTB/BBB opening prior to CED when compared to those receiving the CED injection only (Figure 6B), indicating that FUS+MB-mediated BTB/BBB opening does indeed substantially augment BPN dispersion through tumor tissue.

3.4 Discussion

The goals of this investigation were (i) to determine the efficacy of BTB/BBB opening with FUS and MBs as a means for targeted brain tumor transfection with systemically administered BPN and (ii) to ascertain whether modulation of the physical tumor microenvironment in conjunction with BTB/BBB opening promotes intratumor BPN transport. Under MR image-guidance, BTB/BBB opening with FUS and MBs elicited a mean 4-fold increase in U87 and B16F1cOVA brain tumor transfection over BPN alone, with some tumors

exhibiting as much as a 16-fold increase in transfection. A T1 contrast enhanced MRI-based analysis of gadolinium transport revealed that interstitial flow in brain tumors increased by an average of 2-fold after BTB/BBB opening, with most voxels also experiencing a marked shift (i.e. mean change of 60º) in interstitial flow direction. BPN that were injected directly into U87 tumors after BTB/BBB opening dispersed far more easily through tumor tissue (i.e. more than a doubling of transfection volume), providing strong evidence that modulation of the physical tumor microenvironment by FUS+MB-mediated BTB/BBB opening enhances BPN distribution throughout tumors after they have been delivered from the bloodstream. In all, this is the first study to demonstrate the successful MR image-guided transfection of both primary and metastatic brain tumors using non-viral gene vectors in combination with FUS and MBs, as well as the first to use an MRI-based analysis to generate spatial maps of interstitial fluid flow changes in response to BTB/BBB opening with FUS and MBs. Our finding that augmented interstitial flow plays a key role in dispersing a non-bioadhesive therapeutic through tumor tissue offers the enticing possibility that this understudied secondary effect of BTB/BBB opening with FUS and MBs can be leveraged to further improve therapeutic outcomes.

The brain-penetrating nanoparticles utilized here are non-viral gene vectors designed to maximize distribution in brain tissue, and thus offer many advantages over other gene carriers. Generally, polymeric non-viral gene vectors have an increased loading capacity, lower cost, and greater ability to tailor physiochemical properties than viral gene carriers. Additionally, non-viral vectors alleviate concerns of pre-existing immunity to naturally occurring viral vectors that could reduce efficacy, as well as safety issues. Furthermore, the dense PEG coating on our brain-penetrating non-viral gene vectors facilitates increased spreading in brain tissue compared to conventionally PEGylated nanoparticles, resulting in enhanced vector distribution and transfection volume in both healthy brain and brain tumor tissues(*85*, *87*). Our group has previously demonstrated safety and efficacy of this FUS-mediated BPN delivery for transfection

of normal brain tissue(*83*). We have also proven therapeutic efficacy in a rat model of Parkinson's disease, in which we were able to achieve durable and therapeutic levels of GDNF transgene expression, thereby leading to restored dopamine levels and dopaminergic neuron content, and reversed behavioral indicators of PD-associated motor dysfunction(*86*).

The use of FUS and BPN to achieve gene expression in brain tumors described here represents a new strategy for brain tumor gene delivery that can overcome many of the challenges associated with more conventional methods. First, this approach is noninvasive, offering an advantage over direct injection methods for delivering gene vectors into brain tumor tissue. While some groups have achieved transfection of brain tumors following systemic administration of gene vectors, many rely upon the enhanced permeability and retention (EPR) effect for delivery into the tumor tissue. Use of the EPR effect alone can be ineffective due to the heterogeneous vascular permeability and high interstitial fluid pressures that characterize the BTB(*9*, *12*). Additionally, in GB, invasive cells infiltrate into normal brain tissue and reside behind the BBB. Thus, they cannot be reached by therapeutics delivered via the EPR effect(*15*). MB activation with FUS has the ability to transiently permeabilize vessels to overcome the BBB and BTB, and allows for precise spatial targeting of the tumors as well as surrounding tissue where invasive cells reside. While the tumors used in this study are not invasive, we designed our treatment approach to target the entire tumor as well as the surrounding edges, which will be a crucial factor for therapeutic efficacy in invasive models of GB. On average, we achieved a 4-fold increase in *ex vivo* bioluminescence in mice treated with FUS + MB BTB/BBB opening and Luc-BPNs compared to those receiving only an i.v. injection of Luc-BPN. We saw similar efficacy in both the U87 and B16F1cOVA tumor models, representing primary and secondary brain tumors, respectively, suggesting that this approach is applicable across tumor models.

The lower PNP used in this study (0.45 MPa) was chosen based on previous studies from our group(*83*, *86*), wherein we safely delivered similar-sized BPN across the BBB in rats

(160g-200g b.w.) using the same albumin-shelled MB formulation and the same 1.1 MHz FUS system. In those studies, detailed histological examinations of brain tissue revealed no signs of damage when applying 0.6 MPa PNP FUS (measured in water). It is known that, at frequencies in the range of 1.0 to 1.25 MHz, the middle region of the skull reduces FUS transmission no more than 20% for rats weighing between 160 and 200 g(*110*). This translates to an estimated non-derated PNP of 0.48 MPa in the rats. Thus, even if FUS attenuation by the skull in mice (measured to be 18% for 1.5 MHz FUS(*111*)) is not considered, the 0.45 MPa PNP used here is still below the known safety threshold we have previously established for these MBs in combination with this FUS system. If considering skull attenuation in mice, this PNP is well below the safety threshold.

From that baseline PNP of 0.45 MPa, we then chose to test whether increasing PNP could improve BPN delivery and transfection, as previous studies have shown enhanced size and volume of BBB opening with increasing PNP(*112*, *113*). A PNP of 0.55 MPa was chosen for this purpose because, while it clearly enhances acoustic signatures associated with stable cavitation [i.e. subharmonic (Figure 1H), 2^{nd} harmonic (Figure 1I), and 3^{rd} harmonic (Figure 1J)] in our system, it does not elicit a detectable increase in broadband signal associated with inertial cavitation, which could indicate the onset of microvascular and/or tissue damage (Figure 1K). Nonetheless, when considering BPN delivery (Figures 1A, 1B, 1C, and 1D), tumor transfection (Figure 2), BTB/BBB opening (Figure 3), and interstitial fluid flow (Figures 4 and 5), we surprisingly observed no statistically significant differences between the 2 PNPs. Clearly, both of the tested pressures generate responses sufficient to (i) deliver ~50 nm-sized BPNs across the BTB/BBB and into the tissue and (ii) alter interstitial transport to promote BPN-mediated transfection (see forthcoming discussion). It is possible that, at least in the context of these specific experiments, our assays were insufficiently sensitive to detect differences between 0.45 MPa and 0.55 MPa and/or that these differences in MB activation simply had no appreciable

impact on key delivery metrics (Figures 2-5). Further studies would be needed to determine the PNP below 0.45 MPa at which BPN delivery and transfection are compromised and whether further increasing BPN above 0.55 MPa yields improved delivery.

It is well established that activating MBs with FUS in the brain yields enhanced vascular permeability, however, there is now mounting evidence that modulation of the interstitial space is also an important factor facilitating agent delivery and distribution in targeted tissues. Very recent work using high resolution imaging techniques coupled with physiologically based pharmacokinetic modelling (PKPB) demonstrated that FUS + MB BTB opening caused a shift from diffusion-dominated to convection-dominated transport in intracranial tumor tissue(*40*). Here, we explored how FUS + MB BTB opening alters the transport of agents in our intracranial tumor models and how this may aid in our ability to transfect brain tumor tissue with our non-viral gene vectors. Utilizing an MRI-based technique to assess transport of gadolinium contrast agent, we measured a roughly two-fold increase in flow velocity magnitude after FUS-mediated BTB/BBB opening, consistent with recent PKPB-derived results (*40*). We postulate that the increase in flow velocity magnitude is due to a post-BTB/BBB opening increase in near-wall pressure, which would then drive fluid flow into the tissue. Beyond increased fluid velocity magnitude, we also saw a roughly 60-degree change in interstitial flow direction. This is consistent with increased mixing within the interstitial space, which could yield more frequent contact between BPN and cells within the tumor, potentially allowing for enhanced uptake.

This MRI-based analysis provides us with a framework for understanding FUS-induced changes in transport of gadolinium in the tumor interstitial space; however, agent size and physiochemical properties play a significant role in determining transport dynamics. As diffusivity within a tissue is dependent, in part, upon particle size, BPN will have a smaller tissue diffusivity as compared to gadolinium chelates. Thus, with limited diffusivity, the movement of larger BPN (~50 nm) through the tissue would be dominated by convection and sensitive to

changes in interstitial flow velocity, a concept illustrated by the Péclet number ($Pe = V_i*L/D$, where v is the velocity, L is the characteristic length in the direction of interest and D is the diffusion coefficient). Conversely, the smaller gadolinium chelates (~0.75 nm) are likely to be transported via both diffusion and convection independent of the interstitial flow velocity magnitude. While it follows that spatiotemporal regions with lower calculated velocities may have a lower distribution of BPN, testing this hypothesis would require assessing BPN delivery and transfection with more spatially precise approaches that allow for comparisons to interstitial flow maps.

The observation that gadolinium flow through tumor interstitial space is increased as a result of MB activation with FUS led us to experimentally test whether FUS + MB BTB/BBB opening also significantly alters transport of our larger (50 nm) BPN gene vectors. We found that FUS + MB-mediated BTB/BBB opening of intracranial U87mCherry xenograft tumors immediately prior to CED injection of BPN resulted in a two-fold enhancement in transfection volume compared to CED injection alone. Of note, this result is consistent with a previous study wherein BBB opening with FUS and MBs enhanced the spread of AAV vectors(*90*) in normal brain tissue. Importantly, the ability of FUS+MB-mediated BTB/BBB opening to promote the spread of BPN supports the concept that enhanced interstitial fluid velocity facilitates the penetration of BPN through tumor tissue, contributing to tumor transfection.

Finally, we note that the MR image-targeted, noninvasive gene delivery approach described here represents a platform that can be combined with many other established and experimental approaches to generate innovative treatment strategies with the potential for superior efficacy. For example, immunotherapies hold much promise for long-lasting therapeutic responses in treatment of extracranial malignancies. The delivery of BPN carrying immunomodulatory genes to brain tumors with FUS and MBs could be used to shift the balance from an

immunosuppressive to an immunostimulatory tumor microenvironment to promote an antitumor immune response(*114*).

3.5 Materials and Methods

3.5.1 Tumor Implantation.

U87mg tumor cells or U87mg cells that had been stably transfected with an mCherry reporter gene (i.e. U87mCherry) were implanted into 6-8-week-old male athymic nude mice purchased from Charles River. B16F1cOVA cells were implanted in 8-10-week-old C57BL6 mice, which were also purchased from Charles River. Mice were anesthetized with a mixture of Ketamine (40 mg/kg; Zoetis, Kalamazoo, MI) and Dextomitor (0.2 mg/kg, Zoetis, Kalamazoo, MI) in 0.9% sterile saline and situated on a stereotaxic frame. Buprenorphine was administered subcutaneously. The surgical site was prepared with alternating scrubs of alcohol and iodine and an incision was made at the midline of the scalp. A drill was used to create the burr hole located 2 mm to the right and 0.5 mm anterior to the bregma. A 10 µl Hamilton syringe with a 26-gauge needle was loaded with tumor cells (1.5×10^8 U87 cells/ml, 2.0×10^8 B16F1cOVA cells/ml). The needle tip was lowered to a depth of 4 mm below the skull surface and then withdrawn 1 mm to a final depth of 3 mm. A total volume of 2 µl of tumor cells (3×10^5 U87mCherry and U87mg cells or 4×10^5 B16F1cOVA cells) were injected over 4 minutes. After one additional minute, the needle was slowly removed from the brain. The incision was closed with sutures and animals were given Antisedan to reverse the anesthesia.

3.5.2 Brain-Penetrating Nanoparticle Fabrication and Characterization.

BPN were prepared as previously described(*85*). Briefly, methoxy-polyethylene glycol-N-hydroxysuccinimide (mPEG-NHS, 5 kDa, Sigma-Aldrich, St. Louis, MO) was conjugated to 25 kDa branched PEI (Sigma-Aldrich) to yield PEG-PEI copolymers, as previously described(*85*, *87*, *115*). Nuclear magnetic resonance (NMR) analysis was conducted to confirm PEG to PEI molar ratio of 50, a ratio previously shown to provide sufficient shielding of the BPN positive surface charge(*85*); 1H NMR (500 MHz, D_2O): δ 2.48-3.20 (br, CH_2CH_2NH), 3.62-3.72 (br,

CH_2CH_2O). The green fluorescent reporter ZsGreen-expressing plasmids driven by the CMV promoter was purchased from Clontech Laboratories Inc. (Mountainview, CA). The luciferase-expressing plasmid driven by human β-actin promoter (i.e. pBAL) was produced and provided by Copernicus Therapeutics (Cleveland, OH). Mirus Label IT Tracker Intracellular Nucleic Acid Localization Kit (MirusBio, Madison, WI) was used to fluorescently tag plasmids with Cy5 fluorophores. BPN were formed by dropwise addition of 10 volumes of labeled or unlabeled plasmids (0.2 mg/mL) to 1 volume of a swirling polymer solution at an optimized nitrogen to phosphate (N/P) ratio of 6. BPN formulations were engineered by condensation of plasmids by a mixture of non-PEGylated PEI (25%) and PEG-PEI (75%). For IVIS imaging, Cy5-labeled plasmids were used to assemble fluorescently-labeled BPN. The plasmid/polymer solution was incubated for 30 minutes at room temperature to spontaneously form BPN. The, BPN were washed twice with 3 volumes of ultrapure distilled water, and re-concentrated to 1 mg/ml using Amicon Ultra Centrifugal Filters (100,000 MWCO; Millipore Corp., Billerica, MA). Plasmid concentration was determined via absorbance at 260 nm using a NanoDrop ND-1000 spectrophotometer (NanoDrop Technologies, Wilmington, DE). Lastly, the hydrodynamic diameters as well as polydispersity index (PDI) and ζ-potentials of BPN were measured by dynamic light scattering and laser Doppler anemometry, respectively, in 10 mM NaCl solution at pH 7.0 using a Nanosizer ZS90 (Malvern Instruments, Southborough, MA).

3.5.3 Blood-Tumor/Blood-Brain Barrier Opening with MR Image-Guided FUS and Microbubbles.

FUS treatments were applied 5 days after B16F1cOVA implantation and 7 days after U87mCherry or U87mg implantation. Mice were anesthetized with a mixture of Ketamine (40 mg/kg; Zoetis, Kalamazoo, MI) and Dextomitor (0.2 mg/kg, Zoetis, Kalamazoo, MI) in 0.9% sterile saline and tail veins were cannulated to allow for multiple intravenous injections. The MR-

guided FUS system (RK-100, FUS Instruments) sat directly on the patient table of a clinical 3T MRI scanner (Siemens Prisma). Mice were placed supine on the MR-guided FUS system with the skull sonically coupled to a 1.1 MHz spherically focused ultrasound transducer (with a 550 kHz hydrophone mounted in the center for passive cavitation detection) immersed in a degassed water bath. For the general treatment procedure, MultiHance gadolinium contrast agent (Bracco Diagnostics) was administered intravenously and a pre-FUS T1-weighted contrast-enhanced MR image of the entire brain was acquired using a custom-built 3-cm loop receive RF coil and three-dimensional spoiled gradient echo pulse sequence. Pulse-sequence parameters for all T1-weighted images were identical: TR/TE = 12/4.35 ms, flip angle = 25°, readout bandwidth = 300 Hz/Px, FOV = 38×77×36 mm, resolution = 0.3 mm isotropic, total time per image = 3:04.

Eight target spots were chosen from this pre-sonication MR image to cover the entire tumor and surrounding tissue. To open the BTB/BBB, albumin-shelled MBs (1×10^5/gram body weight; manufactured as previously described) (*116*) and luciferase plasmid-bearing BPN (Luc-BPN or Cy5 labeled Luc-BPN; 1 µg/gram body weight) were intravenously injected and FUS was applied to the targets using 0.45 MPa or 0.55 MPa PNP (measured in water). FUS was applied in 10 ms pulses with a 2 s pulsing interval (i.e. 0.5% duty cycle) for a total of 2 minutes. Animals were then re-injected with gadolinium contrast agent and post-sonication T1-weighted contrast-enhanced MR images were acquired to confirm BTB/BBB opening. Following treatment, mice were given Antisedan to reverse the anesthesia.

In a subset of the Luc-BPN delivery cohort (n=4 per group x 2 tumor types x 2 PNPs = 16 total, referred to as “TM” for transport mice), this general procedure was varied to include additional MR imaging for transport analysis as described below.

3.5.4 MR Imaging for Transport Analysis.

TM were imaged with MRI using an alternative protocol to permit interstitial tumor transport analysis. For these animals, a three-dimensional T1-weighted MR image was acquired immediately prior to the injection of the contrast agent to obtain the baseline signal intensity in the tissue. The contrast agent was then intravenously injected and a series of four T1-weighted contrast-enhanced MR images were obtained. Following FUS BTB/BBB opening (described previously), a T1-weighted MR image was again acquired to obtain baseline signal intensity for post-FUS measurements. The contrast agent was injected intravenously and a second series of four T1-weighted contrast-enhanced MR images was acquired.

3.5.5 MR Image Analysis for Grayscale Intensity.

For TM, the first T1-weighted MR image in the pre- and post-FUS contrast enhanced imaging series was analyzed for grayscale intensity of gadolinium enhancement. Two different ROIs were analyzed, one encompassing the entire FUS-targeted region, referred to as “BTB+BBB”, and one encompassing only the tumor, referred to as “BTB”. Mean pixel grayscale intensity was quantified within each of these ROIs in the pre-FUS and post-FUS images for each animal. An equivalent ROI was chosen on the contralateral side, and the grayscale intensity was subtracted as background.

3.5.6 Transport Analysis.

We analyzed the spatiotemporal evolution of gadolinium transport in tumors using a recently described approach(*109*). Briefly, for each pre-FUS and post-FUS imaging series, the acquired images were loaded into the post-processing algorithm. The pre-contrast image was subtracted from the post-contrast series to remove background signal. For each animal, the ROI was

chosen to encompass the entire enhancing region from the pre-FUS images as well as a portion of surrounding non-enhancing tissue, and the same ROI was used to analyze pre and post-FUS sequences. The tissue slice analyzed in the algorithm corresponded to the coordinate that was targeted for FUS BTB/BBB opening. The spatiotemporal evolution of solute concentration, in this case gadolinium, can be approximated by a differential equation dependent upon input velocity and diffusion coefficient. Using the gadolinium signal intensity over time acquired in the T1-weighted MR images, the algorithm solves the inverse problem to estimate diffusion coefficients and interstitial fluid velocities within the selected ROI. Using this technique, we obtained spatial maps of fluid velocity magnitude and direction and diffusion coefficient for the selected ROI before and after FUS + MB BTB/BBB opening.

3.5.7 Passive Cavitation Detection.

Acoustic emissions were detected with a 2.5 mm wideband unfocused hydrophone mounted in the center of the transducer. Acoustic signal was captured using a scope card (ATS460, Alazar, Pointe-Claire, Canada) and processed using an in-house built MATLAB algorithm. Acoustic emissions at the fundamental frequency, harmonics (2f, 3f, 4f), sub harmonic (0.5f), and ultra-harmonics (1.5f, 2.5f, 3.5f) were assessed by first taking the root mean square of the peak spectral amplitude (V_{rms}) in each frequency band after applying a 5 kHz bandwidth filter, and then summing the product of V_{rms} and individual sonication duration over the entire treatment period. Inertial cavitation was assessed by summing the product of V_{rms} and individual sonication duration for all remaining emissions (broadband) over the entire treatment period.

3.5.8 Cy5 Ex Vivo Fluorescence Imaging and Confocal Imaging.

Roughly 6 hours following BTB/BBB with FUS and MBs for delivery of Cy5-labeled Luc-BPN delivery to U87mg tumors, mice were euthanized via intraperitoneal injection of Euthasol. Brains were removed and imaged on the IVIS Spectrum for Cy5 fluorescence signal using the 640/680 excitation/emission filter set and auto exposure settings. Tumors were then immediately removed and imaged using the same settings. For whole brain images, an identical circular ROI was used for every sample. For tumor images, the ROIs were drawn around the tumor edges for each sample to encompass the entire tumor. Cy5 fluorescence was quantified for both whole brain and tumor samples using described ROIs and reported as radiant efficiency. Brain tumor tissue was stored at -80 °C immediately following imaging on the IVIS spectrum. Tissues were then fixed in 4% paraformaldehyde, dehydrated in 30% sucrose, and frozen in OCT. Frozen tissues were cut into 5 µm sections using a cryostat (1905, Leica, Buffalo Grove, IL), mounted onto slides, and stained with BS-I Lectin-488. Sections were imaged using a Nikon Eclipse TE2000 confocal microscope (Nikon, Melville, NY) under 60x magnification.

3.5.9 Ex Vivo Bioluminescence Imaging.

Three days following BTB/BBB with FUS and MBs for Luc-BPN delivery, mice were given an intraperitoneal injection of D-luciferin (Gold Biotechnology, St. Louis, MO) at a dose of 150 mg/kg. Five minutes later, mice were euthanized via intraperitoneal injection of Euthasol, and the tumor tissue was harvested. Tumors were incubated in a 1 mg/ml solution of D-luciferin for 3 minutes, and bioluminescence imaging was performed on the IVIS Spectrum using a 3-minute exposure time. Using the Living Image software, ROIs were drawn around the tumor edges to encompass the entire tumor sample. Photon flux was quantified and reported as total flux and average radiance.

3.5.10 Convection-Enhanced Delivery of ZsGreen Brain-Penetrating Nanoparticles After Blood-Tumor/Blood-Brain Barrier Opening with Focused Ultrasound and Microbubbles.

U87mCherry tumor cells were implanted 16 days prior to treatment as previously described. The day 16 time point was chosen so that the tumors would be easier to target with our CED injections. Mice were anesthetized with a mixture of Ketamine (40 mg/kg; Zoetis, Kalamazoo, MI) and Dextomitor (0.2 mg/kg, Zoetis, Kalamazoo, MI) in 0.9% sterile saline. Buprenorphine was administered subcutaneously. Tail veins were cannulated in a subset of mice to facilitate intravenous injection of microbubbles and mice were situated in a stereotaxic frame (Stoelting, Wood Dale, IL). For mice receiving FUS + MB BTB/BBB opening, heads were ultrasonically coupled to a 1 MHz single element FUS transducer (Olympus, Center Valley, NJ) with degassed ultrasound gel. The transducer was positioned so that the focus coincided with the location of the tumor in the right striatum. Albumin-shelled microbubbles were intravenously injected (1 x 10^5 microbubbles/gram) and FUS was applied at a 0.45 MPa PNP with a 0.5% duty cycle (10 ms, every 2 seconds, for 2 minutes). Note that this BTB/BBB opening protocol is identical to that used to deliver Luc-BPN under MR image-guidance. Immediately following sonication, the CED procedure commenced. To prepare for CED, heads were cleaned with alternating wipes of alcohol and iodine. A midline scalp incision was made to expose the skull and a drill was used to create a burr hole at the appropriate location to target the tumor. A Neuros syringe (Neuros 1705, Hamilton, Reno, NV) containing a 33g needle and a 1 mm step was inserted at 1 mm/min to the appropriate depth (coordinates determined from T1-weighted MR images acquired one day prior to CED injections). The infusion rate was set to 0.33 µl/min using a frame-mounted syringe pump (UMP3, World Precision Instruments, Sarasota, USA). A total of 19 µg ZsGreen-BPN in 20 ul 0.9% NaCl was injected. Five minutes following the completion of the injection, the needle was slowly removed at 1 mm/min and the burr hole was filled with sterile bone wax.

3.5.11 Confocal Imaging and Quantification of ZsGreen Transfection Volume.

Approximately 48 hours following CED of ZsGreen BPN, mice were euthanized and transcardially perfused with 10 ml of 2% heparinized 0.9% saline followed by 10 ml of Tris-Buffered Saline with 0.1 g/L calcium chloride. Brains were removed, rapidly frozen to -80ºC, and cut into 100 µm sections using a cryostat (1905, Leica, Buffalo Grove, IL). Every other section within 2-3 mm of the injection site was collected on a slide and mounted with permanent mounting medium (P36970, Invitrogen, Carlsbad, USA). Sections were imaged using a Nikon Eclipse TE2000 confocal microscope (Nikon, Melville, NY) under 4x magnification. Multiple images were taken and stitched together in montages to capture the entire injection site. Volume of transfected tumor tissue was quantified from these images using a MATLAB script similar to previous studies(*87*). Briefly, background fluorescence was subtracted and images were thresholded at 5% of the maximum intensity. The total volume of transgene expression was calculated by multiplying the area of distribution from each slice by the slice thickness and summing values for each slice.

3.5.12 Statistical Analysis.

A detailed description of statistical methods for each experiment is provided in corresponding figure legend.

3.6 Acknowledgments

3.6.1 General.

We kindly thank Roger Abounader for providing the stably transfected U87mCherry cell line.

3.6.2 Funding.

Supported by NIH R01CA164789, R01CA197111, R01CA204968 and R01EB020147 (RJP, JH, and JSS). JMM was supported by NIH R372222563. KMK was supported by a NSFGRF.

3.7 Author Contributions.

CTC and BPM performed experimental work. CTC, BPM, and RJP analyzed the data. CTC, BPM, and RJP conceived experiments, with input from JSS, KKA, and JJM. KN, NK, JSS, and JH provided BPNs. AK provided microbubbles. GWM and WJG developed MR sequences and performed MR imaging. KKA and JJM contributed to the conception and execution of the MRI-based transport analysis. EAT performed analysis of cavitation data. JS sectioned and stained tissue sections. CTC and RJP wrote manuscript.

3.8 Chapter 3 Figures

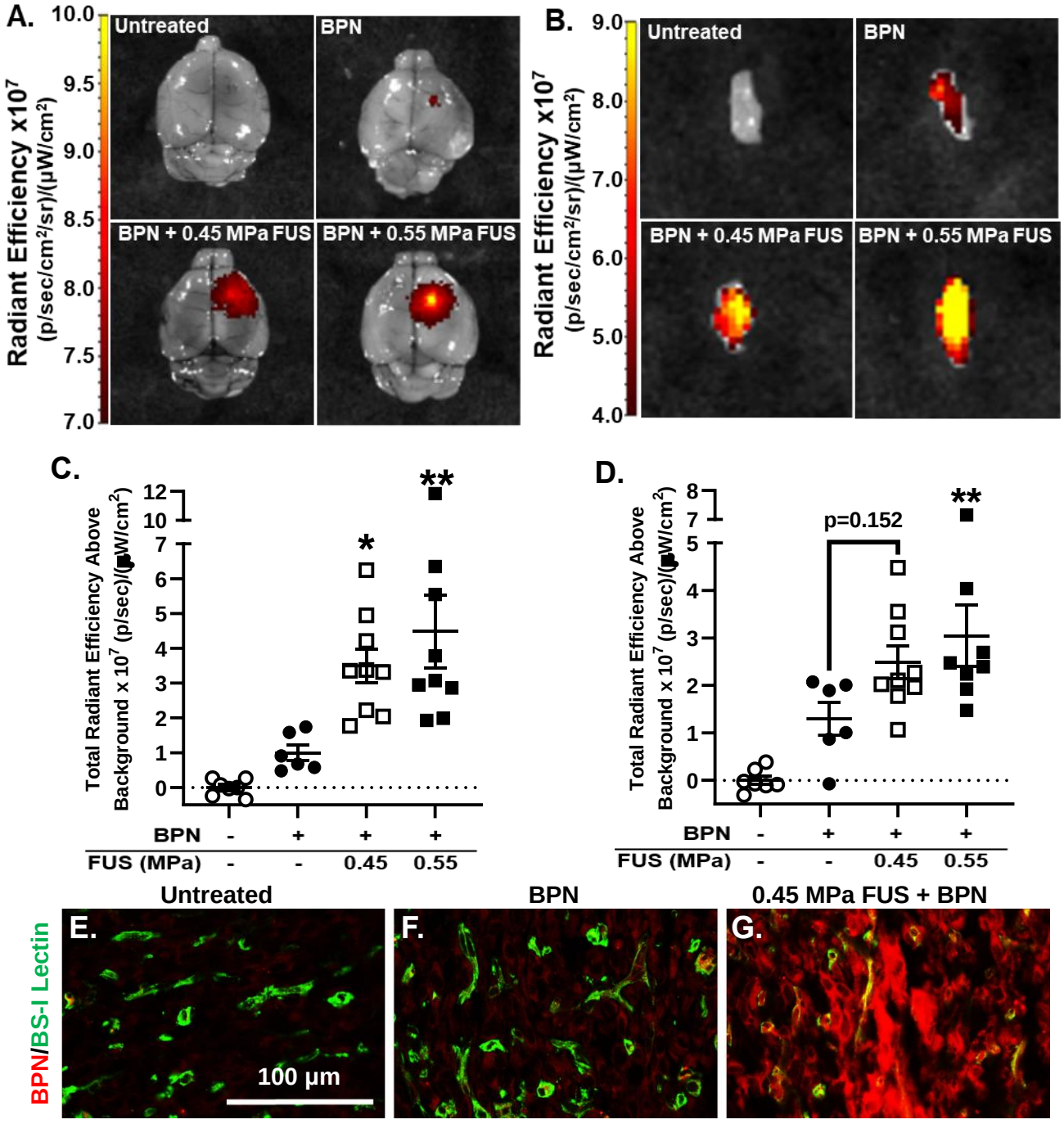

Figure 3.1. MR Image-Guided Delivery of I.V. Administered Brain-Penetrating Nanoparticles (BPN) to U87 Gliomas and Surrounding Brain Tissue with Focused Ultrasound.

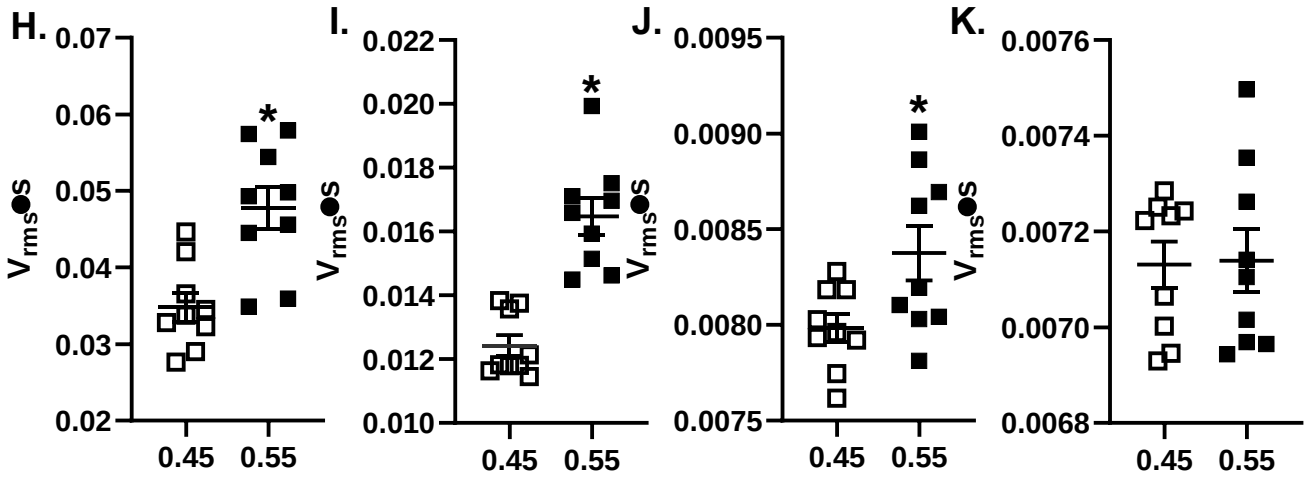

Figure 3.1 (cont.). MR Image-Guided Delivery of I.V. Administered Brain-Penetrating Nanoparticles (BPN) to U87 Gliomas and Surrounding Brain Tissue with Focused Ultrasound. **A**: Fluorescence images of whole brains with U87 tumors after treatment. **B**: Total fluorescence radiant efficiency in whole brains with U87 gliomas. Means ± S.E.M. Means ± S.E.M. *P=0.047 and **P=0.0047 vs. BPN only group. One-way ANOVA followed by Dunnett's multiple comparisons tests. **C**: Fluorescence images of excised U87 tumors after treatment. Tumors are ~2-3 mm in diameter. **D**: Total fluorescence radiant efficiency in excised U87 gliomas. Means ± S.E.M. **P=0.026 vs. BPN only group. One-way ANOVA followed by Dunnett's multiple comparisons tests. **E, F, G:** Confocal images of BPN (Cy5; red) with respect to tumor microvessels (BS-I Lectin; green) showing enhanced delivery and penetration into tumor tissue with 0.45 MPa FUS. **H, I, J, K:** Passive cavitation analyses for sub-harmonic (**H**; *P=0.0014), 2^{nd} harmonic (**I**; *P<0.0001), 3^{rd} harmonic (**J**, *P=0.026), and inertial (**K**; n.s.) emissions. Unpaired t-tests.

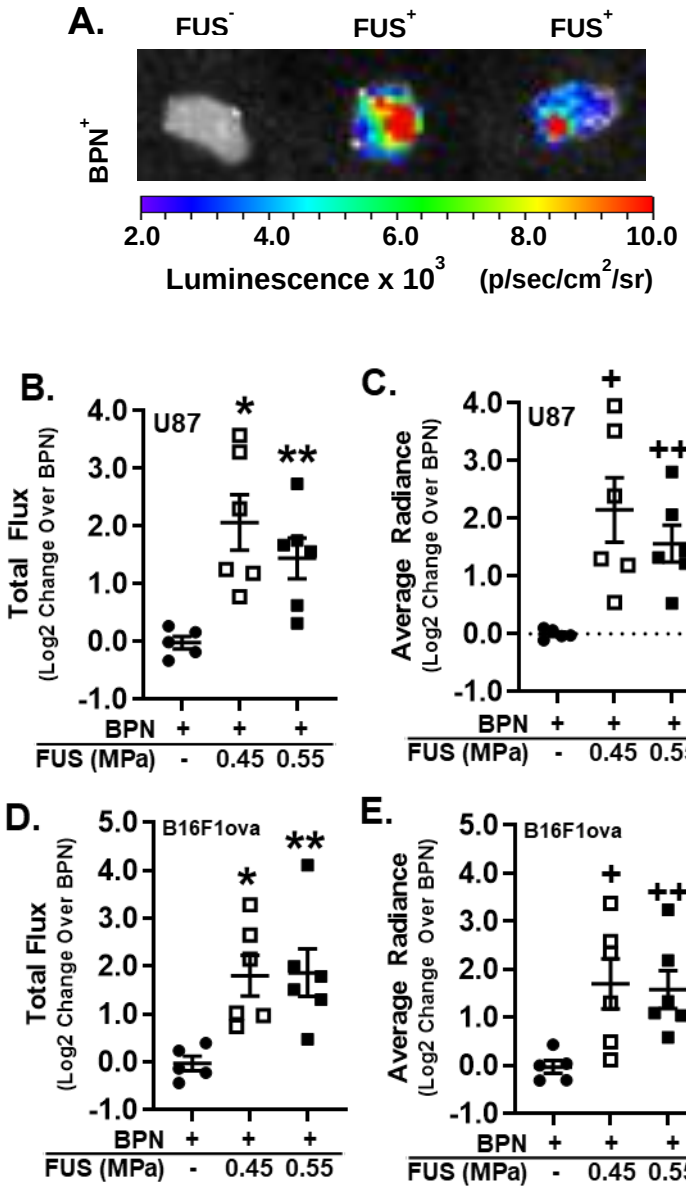

Figure 3.2. MR Image-Guided Transfection of Brain Tumors with I.V. Administered Brain-Penetrating Nanoparticles (BPN) and Focused Ultrasound. A: Bioluminescence images of U87 tumors 3 days after treatment. Tumors are ~2-3 mm in diameter. **B, C**: Scatter plots of luciferase expression in U87 gliomas, presented as Total Flux (B) and Average Radiance (C). Means ± S.E.M. *P=0.004, **P=0.040, $^{+}$P=0.006 and $^{++}$P=0.040 vs. BPN. **D, E**: Scatter plots of luciferase expression in intracranial B16F1ova melanomas, presented as Total Flux (D) and Average Radiance (E). Means ± S.E.M. *P=0.020, **P=0.016, $^{+}$P=0.027, and $^{++}$P=0.040 vs. BPN. Significance assessed in all graphs by One-way ANOVA followed by Tukey's t-tests.

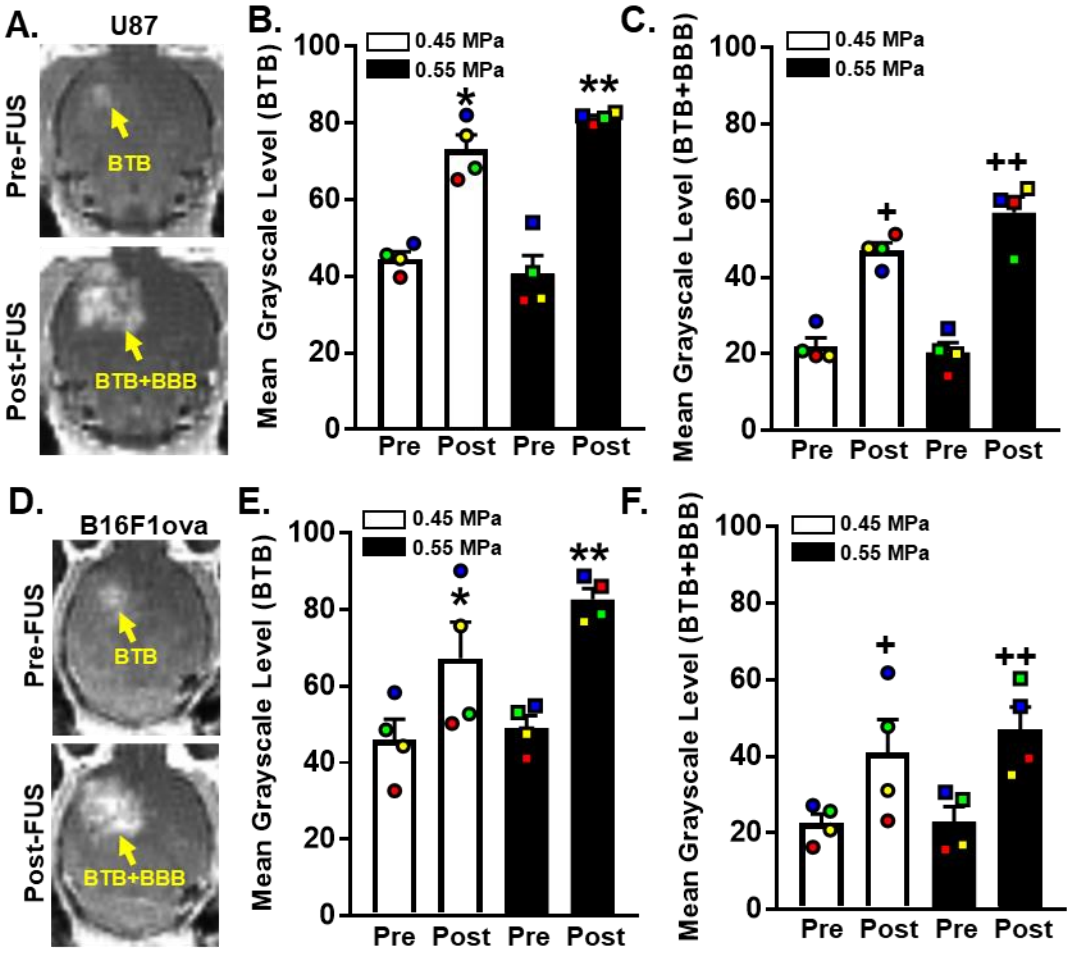

Figure 3.3. Blood-Tumor (BTB) and Blood-Brain (BBB) Barrier Opening after Application of MR Image-Guided FUS as Assessed by T1-Weighted Contrast MRI. A: Pre- and post-FUS T1-weighted contrast MR images of U87 gliomas. **B, C:** Bar graphs of pre- and post-FUS mean grayscale levels in BTB (B) and BTB+BBB (C) ROIs, denoted by yellow arrows in panel A. Paired data points are denoted by common colors and shapes. Bars=S.E.M. *P=0.0005, **P=0.0001, $^{+}$P=0.003, and $^{++}$P=0.0004 vs. "Pre" at same peak-negative pressure. **D:** Pre- and post-FUS T1-weighted contrast MR images of B16F1ova melanomas. **E, F:** Bar graphs of pre- and post-FUS mean grayscale levels in BTB (E) and BTB+BBB (F) ROIs. Bars=S.E.M. *P=0.017, **P=0.0018, $^{+}$P=0.018, and $^{++}$P=0.0053 vs. "Pre" at same peak-negative pressure. Significance assessed in all graphs by Two-way RM ANOVA followed by Sidak's multiple comparison tests.

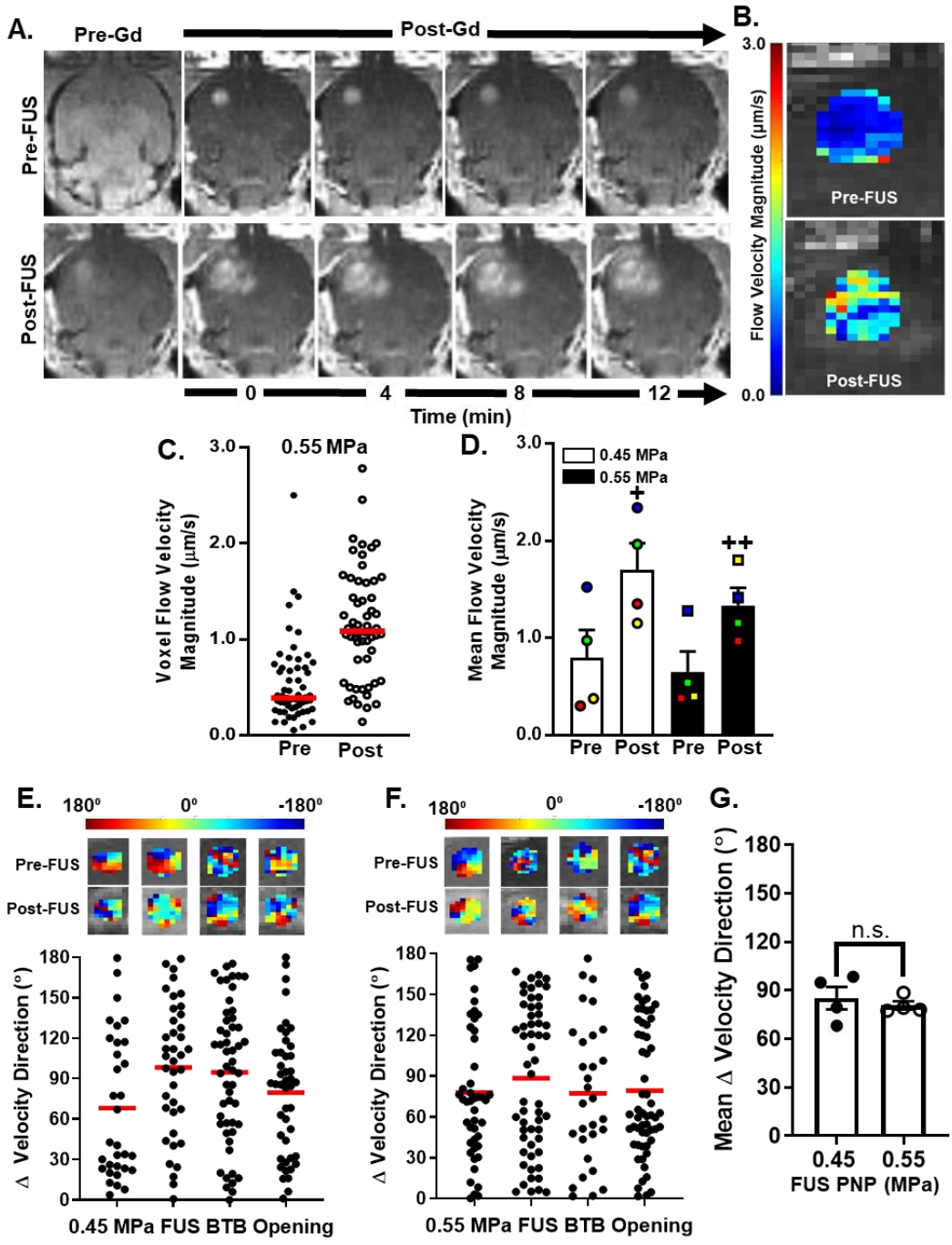

Figure 3.4. Blood-Tumor Barrier Opening with MR Image-Guided FUS Markedly Alters Interstitial Flow Velocity in U87 Gliomas. A: Pre- and post-FUS (0.55 MPa) T1-weighted contrast MR image sequences used for interstitial flow analyses. Gd=gadobenate dimeglumine contrast agent (Multihance®) administration. **B:** Flow velocity magnitude map derived from the MR images in A. **C**: Distribution of pre- and post-treatment voxel flow velocity magnitudes from B. Red lines denote medians. **D:** Plot of and mean flow velocity magnitudes, pre- and post-treatment, with 0.45 MPa and 0.55 MPa FUS. Paired data points are denoted by common colors and shapes. Bars=S.E.M. $^{+}$P=0.006, and $^{++}$P=0.023 vs. "Pre" at same peak-negative pressure. Significance assessed by Two-way RM ANOVA followed by Sidak's multiple comparison tests. **E, F**: Velocity direction changes in individual tumors due to BTB opening with 0.45 MPa (E) and 0.55 MPa (F) FUS. Each data point represents one voxel. **G**: Mean velocity direction changes. Significance tested by unpaired t-test.

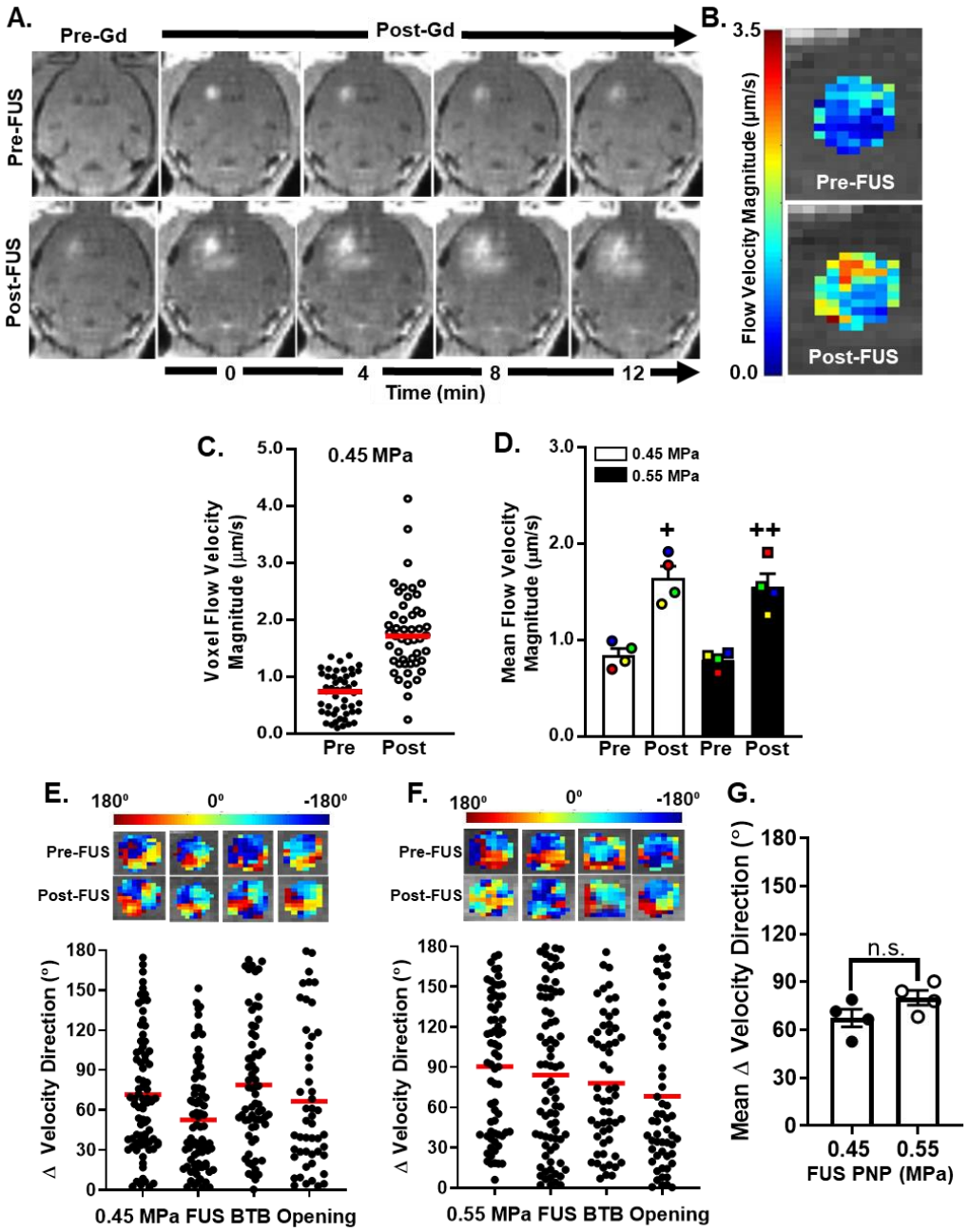

Figure 3.5. Blood-Tumor Barrier Opening with MR Image-Guided FUS Enhances Interstitial Fluid Velocity In Intracranial B16F1cova Melanomas. A: Representative pre- and post-FUS (0.45 MPa) T1-weighted contrast MR image sequences used for interstitial flow analyses. Gd=gadobenate dimeglumine contrast agent (Multihance®) administration. **B:** Flow velocity magnitude map derived from the MR images in A. **C**: Distribution of pre- and post-treatment voxel flow velocity magnitudes in B. Red lines denote medians. **D:** Plot of mean flow velocity magnitudes, pre- and post-treatment, with 0.45 MPa and 0.55 MPa FUS. Paired data points are denoted by common colors and shapes. Bars=S.E.M. $^{+}$P=0.004, and $^{++}$P=0.005 vs. "Pre" at same peak-negative pressure. Significance assessed by Two-Way RM ANOVA followed by Sidak's multiple comparison tests. **E, F**: Velocity direction changes in individual tumors due to BTB opening with 0.45 MPa (E) and 0.55 MPa (F) FUS. Each data point represents one voxel. **G**: Mean velocity direction changes. Significance tested by unpaired t-test.

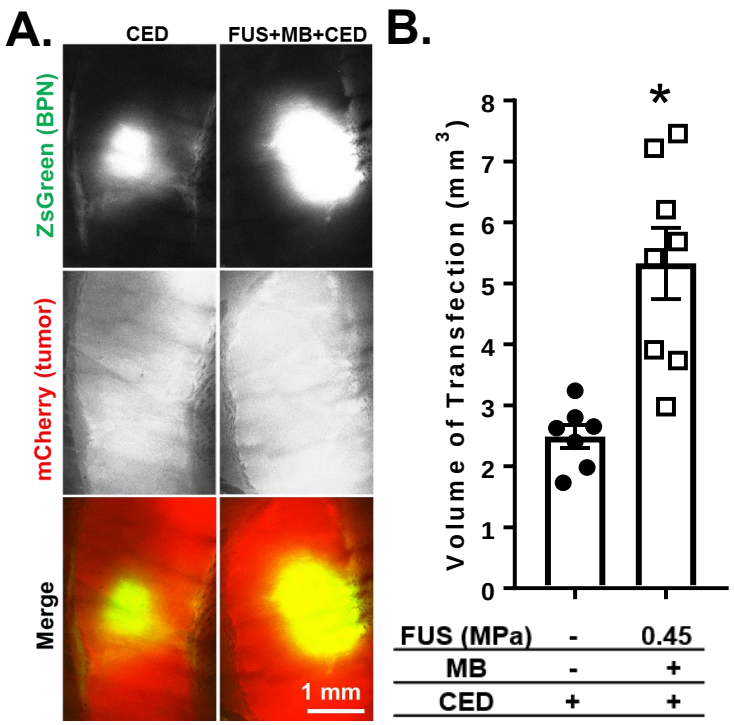

Figure 3.6. BTB Opening with FUS and MBs Augments the Penetration of Brain-Penetrating Nanoparticles through U87 Gliomas. A: Confocal images of ZsGreen transgene expression (green) in mCherry-expressing U87 gliomas (red). **B:** Graph of ZsGreen transfection volumes. *P=0.0008. Unpaired t-test.

Chapter 4: Investigation of Focused Ultrasound Preconditioning for MRgFUS-Mediated BPN Transfection of Intracranial Tumors

4.1 Abstract

Brain tumors present a unique challenge for noninvasive gene delivery approaches, specifically due to the blood-tumor barrier (BTB), Blood-brain barrier (BBB), and a dense, electrostatically charged extracellular matrix (ECM). In the previous chapter of this dissertation, we have demonstrated that focused ultrasound (FUS) and microbubble (MB) BTB/BBB opening facilitates delivery of non-viral brain-penetrating nanoparticle gene vectors (BPN) into brain tumor tissue, enabling significant transfection of intracranial tumors compared to the enhanced permeability and retention effect (EPR). FUS applied at higher duty cycles and pressures immediately before FUS + MB BBB opening in rat brain tissue has proved effective for enhancing transfection over BBB opening alone up to 5-fold. Here, we demonstrate that a similar preconditioning approach in intracranial U87 xenograft tumors was not effective in enhancing transfection achieved by FUS + MB BTB/BBB opening. The preconditioning parameters tested here generated mild to moderate tissue heating, but did not significantly enhance transfection, BTB/BBB opening as measured by acoustic emissions and gadolinium delivery, or interstitial transport properties within treated tissue.

4.2 Introduction

Gene delivery to brain tumors is difficult for many reasons. Specifically, a number of physical barriers impede effective delivery of systemically administered gene vectors into the tissue(*103*). First, leaky vessels in the tumor core contribute to elevated interstitial fluid pressure (IFP) and limited convective transport into the tissue, forming the BTB(*9*, *117*). Second, despite BBB dysfunction throughout much of the tumor, vessel permeability is spatially heterogenous and some tumor vessels are thought to retain BBB-like character(*12*). Furthermore, invasive tumor cells, such as those characteristic of highly invasive glioblastoma (GB), are supplied by normal brain capillaries with intact BBB(*8*, *15*). Lastly, the tumor tissue itself limits therapeutic distribution in the tissue due to the dense lattice of electrostatically charged extracellular matrix (ECM) proteins hindering agent transport(*17*). In this study, we explore the use of focused ultrasound to overcome both vascular and tissue barriers for non-viral, non-invasive gene delivery to brain tumors.

Focused ultrasound (FUS) activation of circulating microbubbles (MBs) is a noninvasive technique for safe, targeted, and reversible opening of the BBB(*35*, *36*, *104*, *118*). Clinical trials have demonstrated successful BBB opening with FUS and MBs in human patients suffering from Alzheimer's disease, brain tumors, and ALS(*29–31*). Preclinically, FUS has been used for the delivery of a wide range of agents, including antibodies, chemotherapeutic drugs, as wells as both viral and non-viral gene vectors, to both normal and diseased brain tissue(*56*, *83*, *86*, *106*). Our group has developed a non-viral gene delivery approach for brain transfection using MR image guided-FUS (MRgFUS) + MBs and plasmid-bearing brain-penetrating nanoparticles (BPNs). We have demonstrated reporter gene transfection of both normal brain and brain tumor tissue using this approach(*83*, *95*). Additionally, we have confirmed therapeutic utility of this approach in a 6-OHDA Parkinson's disease model, in which we were able to reverse behavioral manifestations of disease progression(*86*).

In addition to vascular permeabilization, ultrasound has been shown to have effects on brain tissue that can enhance dispersion of agents within the extracellular space, both with and without intravascular microbubbles. Application of ultrasound to *ex vivo* brain slices yielded increases in extracellular and perivascular spaces measured by TEM imaging, as well as increased movement of subsequently injected nanoparticles(*88*). Transcranial FUS applied to rat brains immediately prior to injection of non-adhesive nanoparticles generated significantly increased particle distribution in the tissue(*89*). Furthermore, it has been demonstrated that application of ultrasound to brain tissue with intravascular microbubbles prior to injection of AAV-GFP vectors resulted in a 3-fold increase in transfection volume(*90*). Similarly, we recently demonstrated an increase in BPN-mediated transfection with application of FUS prior to direct injection of the nanoparticles by convection-enhanced delivery (CED)(*95*). Given this result, we then developed an ultrasound preconditioning approach in which FUS was applied (in the absence of microbubbles) to the targeted tissue prior to FUS + MB-mediated delivery of reporter gene-BPNs across the BBB. FUS pre-conditioning followed by FUS + MB BBB opening resulted in a 5-fold enhancement in reporter gene transfection compared to BBB opening alone. Our results suggested that the achieved increase in transfection is due to modulation of the brain parenchyma rather than modulation of subsequent BBB opening. This study established that FUS preconditioning is a safe and effective method for enhancing FUS-mediated transfection of brain tissue using non-viral gene vectors(*95*).

There has also been evidence that FUS modulation of tumor extracellular space can contribute to favorable delivery and distribution of agents in tumor tissue. Pulsed high intensity focused ultrasound (HIFU) significantly increased uptake, penetration, and efficacy of an intravenously administered monoclonal antibody therapeutic in a flank tumor xenograft model(*91*, *92*). In a different study, pulsed HIFU application improved delivery of i. v. administered chitosan nanoparticles increased roughly 2.5-fold, enhanced nanoparticle

penetration, and was associated with increased blood flow, ECM remodeling, and decreased collagen content in flank tumor xenografts(*93*). Further, application of pulsed FUS in flank tumors prior to direct injection of naked plasmid DNA increased uptake(*94*). While these studies attribute increased agent delivery and penetration to FUS-induced mechanical stresses on the tissue, others have found increased delivery of therapeutic agents using FUS hyperthermia. In a 4T1 breast cancer model of brain metastasis, hyperthermia treatments yielded tissue temperatures in the 42-43 °C range, which increased uptake of systemically administered liposomal doxorubicin and inhibited tumor growth(*119*, *120*). Ultimately, the thermal and mechanical effects of FUS treatments are not mutually exclusive, and thus it is difficult to attribute tissue bioeffects to a particular mechanism without more extensive treatment characterization.

The goal of this study was to test whether a FUS preconditioning approach could be utilized to improve upon intracranial tumor transfection achieved with BPNs and FUS + MB BTB/BBB opening. Based on our previous studies in rats, we tested two different FUS preconditioning protocols and found no improvement in transfection compared to FUS + MB BTB/BBB opening alone, as measured by *ex vivo* bioluminescence of tumor tissue. At the higher pressure tested for FUS preconditioning, we observed significantly more heating, as well as a trend towards decreased gadolinium delivery, signifying the unsuitability of this particular protocol. We saw no differences in the acoustic emissions quantified for the BTB/BBB opening procedure in any of the groups. The magnitude of gadolinium delivery was similar in the BTB/BBB only and 1.5 MPa preconditioning group. Lastly, MRI-based evaluation of pre- and post-FUS interstitial fluid velocity indicated no changes in tumors receiving FUS preconditioning. While preconditioning has proven effective for enhancing transfection in normal brain tissue, additional studies are needed to identify parameters to successfully translate this approach to brain tumor tissue.

4.3 Results

4.3.1 U87 Brain Tumor Transfection Levels with and without FUS Preconditioning.

First, we tested whether FUS preconditioning prior to FUS + MB BTB/BBB opening enhances transfection in an intracranial U87 glioma model. Roughly two weeks following intracranial tumor implantations, mice received FUS + MB BTB/BBB opening (0.45 MPa) and i.v. luciferase plasmid BPN (Luc-BPN) with or without preceding application of FUS preconditioning (3 MPa with a 1% duty cycle or 1.5 MPa with a 2.25% duty cycle, 10-minute duration), or i.v. Luc-BPN only. Acoustic emissions were assessed by passive cavitation detection from the built-in hydrophone during BTB/BBB opening. Three days following treatment, tumor tissue was harvested and *ex vivo* bioluminescence was performed. Representative *ex vivo* bioluminescence images from all groups is shown in Figure 1A. Quantification of bioluminescence signal from tumor samples is presented as total flux and average radiance in Figure 1B and 1C, respectively. All FUS-treated groups have a significantly higher total flux and average radiance than the BPN only group (~5-9-fold increase), but there is no difference in bioluminescence signal between either FUS preconditioning group and the BTB/BBB opening only group. Preconditioning performed in day 7 tumors showed a roughly 4-fold increase in transfection over BPN only, consistent with magnitude of transfection achieved with FUS + MB BTB/BBB opening in our previous study in chapter 3 of this dissertation (Figure S2).

4.3.2 MR Thermometry Measurements During FUS Preconditioning.

MR thermometry imaging was performed for a total of 16 minutes for all preconditioned animals to obtain temperature measurements. Imaging was started 2 minutes prior to initiation of FUS preconditioning, which lasted for 10 minutes, and continued for 4 minutes following the end of sonication. Thermometry images were analyzed to obtain the temperature rise for the sonication regions over time. Figure 2A and 2B show the average temperature profile over time within the

sonicated region for a representative animal treated with the 1.5 MPa and 3 MPa FUS preconditioning protocols, respectively. Plateau temperature rise, calculated as the average of all temperature measurements for the final 2/3 of the sonication, was roughly 3.0 and 5.5 ºC for the 1.5 MPa and 3 MPa preconditioning groups, respectively (Figure 2C). Thermal dose [cumulative equivalent minutes at 43ºC (CEM43)] was calculated using the average temperature rise in the FUS-treated region over the entire 10-minute sonication, and is shown in Figure 2D.

4.3.3 Acoustic Emissions During BTB/BBB Opening with and without Preconditioning.

Acoustic emissions were quantified from passive cavitation signals collected by a hydrophone mounted in the center of the FUS transducer, shown in Figure 3. No significant differences were seen in acoustic emissions at the second harmonic (Figure 3A), fourth harmonic (Figure 3B), sub-harmonic (Figure 3C), or in the broadband signal (Figure 3D) for any of the FUS-treated groups, suggesting similar bubble activity during BTB/BBB opening in all groups.

4.3.4 Grayscale Intensity Analysis of BTB/BBB Opening in Animals with and without Preconditioning.

Pre-FUS and Post-FUS T1-weighted gadolinium-enhanced MR images were analyzed to obtain grayscale intensity in the FUS-treated region. Representative pre and post-FUS MR images are shown in Figure 4A. Grayscale intensity quantification was performed for all animals in the Luc-BPN cohort using two different ROIs, BTB and BTB/BBB. The BTB ROI refers to the enhancing region on the pre-FUS image, which corresponds to the tumor. The BTB/BBB ROI refers to the enhancing region on the post-FUS region, and therefore encompasses the entire FUS-treated region and is composed of tumor and surrounding normal brain tissue. Pre- and post-FUS grayscale intensity measurements for the BTB ROI is shown in Figure 4B. There is a significant

increase in the grayscale intensity in the post-FUS images in the BTB/BBB only group and the 1.5 MPa preconditioning group. Pre- and post-FUS grayscale intensity measurements for the BTB/BBB ROI is shown in Figure 4C. There is a significant increase in the grayscale intensity in the post-FUS images in the BTB/BBB only group and the 1.5 MPa preconditioning group. For the 3 MPa preconditioning group there is a trend towards increased post-FUS signal, but the increase is not statistically significant($p=0.166$). For each treated animal, post-FUS grayscale intensity for the BTB/BBB ROI is increased compared to pre-FUS grayscale intensity, indicating successful BTB/BBB opening. Due to the differences in timing between pre-FUS and post-FUS imaging in BTB/BBB opening only and preconditioning groups (10-minute delay between pre-FUS gad imaging and post-FUS gad imaging), we did not directly compare Post/Pre-FUS ratios of the BTB only and preconditioned groups. We did, however, compare the Post/Pre FUS grayscale intensity ratio of the two preconditioned groups, shown in Figure S1. There was a trend towards decreased gadolinium delivery in the 3 MPa group for both the BTB and BTB/BBB ROI, though this was not statistically significant.

4.3.5 Transport Analysis in Tumors with and without FUS Preconditioning.

For a subset of animals from the Luc-BPN cohort (n=3, one from each treatment group), and a separate set of animals (n=8), additional pre and post-FUS MR imaging was performed to enable analysis of interstitial gadolinium transport. Representative pre-FUS and post-FUS T1-weighted MR imaging series are shown in Figure 5A. Images were loaded into the transport analysis algorithm, and the corresponding pre-contrast image was subtracted to remove baseline tissue signal. Pixels within the specified ROI, which included the tumor and adjacent normal brain tissue, were analyzed to generate flow velocity magnitude maps, as shown in Figure 5B. The bar graphs in Figure 5C and 5D show mean and median flow velocity magnitudes, respectively, for each animal both pre- and post-FUS treatment. FUS treatment

was a significant source of variation identified by a two-way repeated measures ANOVA for mean (p= 0.0046) and median (p=0.0037) flow velocity magnitude. There was a trend towards an increase in post FUS mean and median flow velocity magnitude for all groups, however this was only statistically significant for the post-FUS mean velocity magnitude of the 1.5 MPa preconditioning group. Ratios of Post FUS to Pre FUS mean and median flow velocity magnitudes are shown in Figure 5E and 5F, respectively. There are no significant differences in flow velocity magnitude ratios between the groups, suggesting no difference in alteration of flow velocity magnitude between the BTB/BBB only and preconditioning groups.

4.3.6 Sensitivity Analysis of Transfection Data.

We performed an effect size analysis using the means and standard deviations of our raw bioluminescence data. The 3 MPa group was excluded from this analysis, as significant tissue heating likely obviates it from translation. A one-way ANOVA between the 3 considered groups yields a significant p value of 0.0192. Post-hoc testing using Tukey's multiple comparison's test to compare the BBB only group to each of the other groups, reveals a significant difference between IV NP and BBB only (p= 0.0114) but no difference between BBB only and the 1.5 MPa preconditioning group (p= 0.2026) (Figure S2A). Since no difference was detected between the BBB only and preconditioning group, we were interested in determining the minimum detectable effect size that we were able to detect in the context of our experimental design. Therefore, we used the Gpower program to calculate the sample size, n, required for the detection of a range of effect sizes for a t-test between the BBB only group and the 1.5 MPa group, with the significance level of 0.05 corrected for multiple comparisons(a = 0.05/2 = 0.025)(*121*). The relationship between sample size and detectable effect size between these two groups is shown in Figure S2B. With a total n of 10 (5 in each group), we were able to detect and effect size of d = 2.3 or larger in our study. Using the BBB only group mean and the pooled standard deviation

of these two groups, we calculated the mean differences and fold changes corresponding to effect size(*122*). Given the results of the sensitivity analysis, our study was able to detect a minimum of 1.9-fold change in bioluminescence of the 1.5 MPa preconditioning group over BTB/BBB opening only.

4.4 Discussion

The goal of this study was to test whether FUS preconditioning applied prior to FUS + MB BTB/BBB opening for BPN delivery can be used to enhance transfection of intracranial tumor tissue. We tested two different preconditioning protocols and found no differences in *ex vivo* bioluminescence between tumors treated with preconditioning prior to BTB/BBB opening and those receiving BTB/BBB opening alone. The 1.5 MPa preconditioning protocol led to only mild tissue heating of roughly 3.0 °C, however, tissue heating was significantly increased in the 3 MPa preconditioning group. Despite mild to moderate heating of the tissue, we found no differences in BTB/BBB opening between any of the groups assessed via acoustic emissions. Grayscale intensity analysis of gadolinium delivery validated successful BTB/BBB opening in all groups, but suggested less delivery in the 3 MPa preconditioning group. FUS-induced increases in interstitial convection have been implicated in increased delivery and penetration of agents into tissues. Thus, we quantified pre- and post-FUS fluid velocity magnitude using an MRI-based method, and found no differences between any of the treatment groups.

It is possible that there is an effect of FUS preconditioning on intracranial tumor transfection that is too small to detect in the context of our experimental design. For this reason, we have performed sensitivity analysis to determine our limits of detection for this study. We found that, given the described parameters, we were able to detect a minimum of about a 1.9-fold change between the BBB only and 1.5 MPa preconditioning group. This is roughly equivalent to the fold-increase achieved in normal rat brain with preconditioning at the lower

pressure in our previous study, and thus we believe a reasonable target effect size for this study(*95*). However, it is possible that a true effect of preconditioning does exist here that can only be detected with increased sample sizes, shown in S2. Due to the large variability in our measurements, S2 illustrates that we are nearing the minimum detectible effect size that would be practical with respect to resources. With a doubling of current group sizes, we could detect a smaller 1.5-fold change between these two groups, however increasing group sizes any further only yields minimal gains in detectible effect size. Ultimately, the data presented in this study showed no trend towards improved transfection with FUS preconditioning, and we chose not to pursue more experimentation with these particular preconditioning parameters. While we acknowledge that there may be a small preconditioning effect that is detectable with the addition of more animals, we conclude that no more than a 1.9-fold increase in transfection compared to BBB only can be achieved with the 1.5 MPa preconditioning protocol.

The FUS preconditioning parameters tested in this study were chosen to recapitulate the parameters utilized successfully in normal rat brain tissue. In the rat study, we applied either 2 MPa or 4 MPa peak negative pressure at a 2.25% duty cycle for 10 minutes. Here, we aimed to achieve similar mechanical displacement of the tissue without causing significant tissue heating. Therefore, due to the thinner mouse skull, which results in less attenuation, we reduced the peak negative pressures for mice by 25% to 1.5 MPa and 3 MPa(*110*). We also reduced the duty cycle to 1% in the 3 MPa group to try to minimize heating. MR thermometry shows that the targeted tissue reached a plateau temperature rise of roughly 3.0 °C for the 1.5 MPa preconditioning group and about 5.5 °C for the 3 MPa preconditioning group, which corresponds to an average CEM43°C of 0.15 and 3.7, respectively. The temperature rise and CEM43°C values for the 1.5 MPa group falls between the temperature rises seen at 2 and 4 MPa in normal rat brain tissue, indicating similar level of tissue heating(*95*). However, we saw a significantly higher temperature rise and CEM43°C in the 3 MPa preconditioning group despite

lowering the duty cycle to 1%. This observed temperature rise was much higher than expected, likely due to the larger treatment volume utilized here, which was 8 FUS target spots compared to only 3 spots in the previous rat study.

The unexpected magnitude of brain tissue heating achieved with the 3 MPa preconditioning protocol raises concerns about safety and renders this particular protocol unsuitable for use in the desired application. Indeed, one of four animals in this group reached a plateau temperature rise of 6.4 degrees Celsius, corresponding to a CEM43 °C of 7.6, as seen in Figure 2C and 2D. This is above the threshold for thermal damage previously identified in dog brain tissue(*123*). Additionally, this animal had the lowest bioluminescence measurements and post-FUS gadolinium measurements out of all of the animals receiving FUS treatment, suggesting a possible adverse effect of the heating on agent delivery and tumor transfection. Furthermore, there was no statistically significant increase in grayscale intensity for either of the measured ROIs (BTB only or BTB+BBB) following FUS BTB/BBB opening in the 3 MPa group, Figure 4B and 4C. There was a trend towards a decreased post FUS to Pre FUS grayscale intensity ratio in the 3 MPa preconditioning group compared to the 1.5 MPa preconditioning group (Figure S1 A and B), however, this was not statistically significant.

Although we did not see any improvement in transfection with the FUS preconditioning parameters tested here, we achieved a roughly 5-9-fold increase in transfection in all groups compared to the BPN only group. This is higher than what we reported in Chapter 3 for FUS + MB BTB/BBB opening for BPN delivery. This difference is likely due to differing timepoints between the previous and current studies. Here, treatments were performed more than two weeks following tumor implantation, whereas the previously reported results were from tumors treated only one week after implantation. We chose to treat later-stage tumors in this study to increase the total volume of tumor tissue, since we hypothesized that FUS modulates the tissue extracellular space. Previous work examining FUS + MB-mediated drug delivery during tumor

progression found that FUS + MB BTB/BBB opening only increased BTB permeability in early stage tumors, as measured by the transfer coefficient of a gadolinium contrast agent, K_{trans}(*50*). However, this study also assessed doxorubicin concentration following delivery of liposomal-doxorubicin (~100 nm), and found that FUS + MB BTB/BBB disruption was able to increase doxorubicin concentration by at least two-fold at all treatment time points, suggesting that FUS can enhance delivery of larger drug carriers regardless of tumor stage and size(*50*). Contrary to these findings, our MR contrast-based measurements show similar post-FUS increases in grayscale intensity as the smaller tumors treated in chapter 3 of this dissertation, suggesting that FUS-induced BTB permeability (even to small MR contrast agents) is independent of tumor size. This differential finding may be driven by differences in the tumor models as well as in the MRI-based measurement method. Here, our ability to transfect these larger tumors with BPNs at a similar (or greater) level is consistent with the finding that FUS-mediated delivery of liposomal-doxorubicin was independent of tumor size/stage. In this study, the observed trend towards enhanced transfection in these larger tumors could be due to a number of factors, for instance increased vessel density, and may depend heavily on the particular tumor model. Future studies will be needed to investigate this further.

Our group has previously identified FUS-induced increased interstitial fluid velocity in brain tumors as a potential key mechanism for enhanced BPN-mediated transfection, as shown in chapter 3 of this dissertation. For this reason, we assessed whether preconditioning of brain tumor tissue prior to FUS + MB BTB/BBB opening alters the magnitude of post-FUS velocity increase. We found that all FUS treatment groups exhibited a similar trend towards increased post-FUS flow velocity magnitude, regardless of whether they received preconditioning prior to BTB/BBB opening. This suggests that the FUS preconditioning protocols tested here are not differentially affecting fluid flow compared to BTB/BBB opening alone. We acknowledge that the post-FUS fluid velocity increases seen here are modest in comparison to our previously

reported FUS-induced doubling of interstitial fluid velocity. This could be an artifact of differences between the two studies, or could have a basis in tumor physiology at different time points. Here, our imaging protocol consisted of only 3 post contrast T1-weighted MR images, compared to 4 used in our previous study. The decreased number of time steps analyzed in the algorithm reduces the resolution of the measurements. Additionally, the images for transport analysis used in this study were acquired 2-3 weeks following tumor implantations, meaning the tumors were significantly larger than those analyzed in our previous study. As previously mentioned, it has been demonstrated that K_{trans} measurements of BTB permeability in FUS-treated tumors were dependent on tumor size, so perhaps FUS-mediated changes in interstitial transport of gadolinium are similarly tumor size-dependent(*50*). If this is the case, contributing factors could include increased vessel leakiness and degree of BBB disruption, and elevated interstitial fluid pressure (IFP) in larger tumors. (*50*)(*124*). Future studies should determine whether smaller magnitude of FUS-mediated increase in flow velocity seen here is due to increased tumor volumes or is an artifact of differences in image acquisition.

Despite previous success in normal brain tissue, we were unable to utilize FUS preconditioning to enhance BPN-mediated transfection of intracranial tumors receiving subsequent FUS + MB BTB/BBB opening with the tested parameters. There are numerous differences in this current study that may contribute to this outcome. Here, we are using mice instead of rats as our animal model, and are testing the approach in a tumor model as opposed to normal brain tissue. Despite compensating FUS parameters for skull attenuation, differences in skull thickness, brain size and geometry, as well as tissue morphology and mechanical properties may contribute to varied bioeffects at the focus of the two tissues. Furthermore, there may be differences in how the tissues respond to the same level of mechanical and/or thermal perturbation. For instance, expression level or even localization of certain mechanosensitive ion channels may be altered in tumor tissue, impeding the normal physiological response. An in-

depth characterization of the tissue bioeffects and mechanism of FUS preconditioning in rat brain tissue will be necessary to begin to interrogate differential tissue responses. Ultimately, FUS preconditioning is still a desirable method to enhance transfection of brain tumor tissue, but further work is needed to devise an effective protocol.

4.5 Materials and Methods

4.5.1 Tumor Implantation.

U87mCherry tumor cells (U87mg cells that had been stably transfected to express the mCherry reporter gene) were implanted into 6-8 week old male athymic nude mice purchased from Charles River, as previously described in chapter 3. Briefly, mice were anesthetized with a mixture of ketamine (40 mg/kg; Zoetis, Kalamazoo, MI) and Dextomitor (0.2 mg/kg, Zoetis, Kalamazoo, MI) in 0.9% sterile saline and buprenorphine was administered. Mouse heads were stabilized on a stereotaxic frame and the surgical site was prepared with alternating scrubs of alcohol and iodine. A midline scalp incision was made and a burr hole was drilled 2 mm to the right and 1 mm anterior to the intersection of the bregma and midline of the skull. U87mCherry tumor cells were loaded into a 10 µl Hamilton syringe, which was then placed in the burr hole and lowered to a depth of 4 mm below the skull and withdrawn 1 mm, for a final depth of 3 mm below the skull surface. A total volume of 2 µl of cell suspension (1.5×10^8 cells/ml, 3×10^5 cells total) was injected over the course of 4 minutes. The needle was slowly removed after one additional minute. Mice were sutured and moved to a heating pad for recovery. Anesthesia was reversed with Antisedan.

4.5.2 BPN Characterization.

BPN were prepared as previously described(*85*). Briefly, methoxy-polyethylene glycol-N-hydroxysuccinimide (mPEG-NHS, 5 kDa, Sigma-Aldrich, St. Louis, MO) was conjugated to 25 kDa branched PEI (Sigma-Aldrich) to yield PEG-PEI copolymers, as previously described(*85*, *87*, *115*). Nuclear magnetic resonance (NMR) analysis was conducted to confirm PEG to PEI molar ratio of 50, a ratio previously shown to provide sufficient shielding of the BPN positive surface charge(*85*); 1H NMR (500 MHz, D_2O): δ 2.48-3.20 (br, CH_2CH_2NH), 3.62-3.72 (br, CH_2CH_2O). The luciferase-expressing plasmid driven by human β-actin promoter (i.e. pBAL)

was produced and provided by Copernicus Therapeutics (Cleveland, OH). BPN were formed by dropwise addition of 10 volumes of labeled or unlabeled plasmids (0.2 mg/mL) to 1 volume of a swirling polymer solution at an optimized nitrogen to phosphate (N/P) ratio of 6. BPN formulations were engineered by condensation of plasmids by a mixture of non-PEGylated PEI (25%) and PEG-PEI (75%). The plasmid/polymer solution was incubated for 30 minutes at room temperature to spontaneously form BPN. The, BPN were washed twice with 3 volumes of ultrapure distilled water, and re-concentrated to 1 mg/ml using Amicon Ultra Centrifugal Filters (100,000 MWCO; Millipore Corp., Billerica, MA). Plasmid concentration was determined via absorbance at 260 nm using a NanoDrop ND-1000 spectrophotometer (NanoDrop Technologies, Wilmington, DE). Lastly, the hydrodynamic diameters as well as polydispersity index (PDI) and ζ-potentials of BPN were measured by dynamic light scattering and laser Doppler anemometry, respectively, in 10 mM NaCl solution at pH 7.0 using a Nanosizer ZS90 (Malvern Instruments, Southborough, MA).

4.5.3 FUS Preconditioning and BTB/BTB Opening

FUS preconditioning and BTB/BBB opening treatments were applied 16 days after U87mCherry implantation. Mice were anesthetized with a mixture of Ketamine (40 mg/kg; Zoetis, Kalamazoo, MI) and Dextomitor (0.2 mg/kg, Zoetis, Kalamazoo, MI) in 0.9% sterile saline and tail veins were cannulated to allow for multiple intravenous injections. Mice were positioned supine on an MR-guided FUS system (RK-100, FUS Instruments), which was placed on the patient table of a clinical 3T MRI scanner (Siemens Prisma). Mouse skulls were sonically coupled to a 1.1 MHz spherically focused ultrasound transducer immersed in a degassed water bath. For the general treatment procedure, MultiHance gadolinium contrast agent (Bracco Diagnostics) was administered intravenously and a pre-FUS T1-weighted contrast-enhanced MR image of the entire brain was acquired using a custom-built 3-cm loop receive RF coil and three-dimensional spoiled gradient

echo pulse sequence. Pulse-sequence parameters for all T1-weighted images were identical: TR/TE = 12/4.35 ms, flip angle = 20°, readout bandwidth = 300 Hz/Px, FOV = 38×77×36 mm, resolution = 0.3 mm isotropic, total time per image = 4:05.

Eight target spots were chosen from this pre-sonication MR image to cover the entire tumor and surrounding tissue. In animals receiving FUS pre-conditioning, FUS was applied to the target spots at either 1.5 MPa with a 2.25% duty cycle (45 ms pulses every 2 seconds) or 3 MPa with a 1% duty cycle (20 ms pulses every 2 seconds) for a total of 10 minutes. Similar to our previous reports, we intravenously injected albumin-shelled MBs (1 x 10^5/gram body weight; manufactured as previously described) (*116*) and luciferase plasmid-bearing BPN (Luc-BPN; 1 µg/gram body weight) and FUS was applied to the targets using 0.45 MPa PNP (measured in water) to open the BTB/BBB. The FUS pulsing protocol consisted of 10 ms pulses with a 2 s pulsing interval (i.e. 0.5% duty cycle) for a total of 2 minutes. Gadolinium contrast agent was re-injected and post-FUS T1-weighted contrast-enhanced MR images were acquired to confirm BTB/BBB opening. Following treatment, mice were removed to a heating pad and given Antisedan to reverse the anesthesia.

The standard MR imaging procedure was varied in some mice (referred to as Tm) to acquire additional pre- and post-FUS MR images for transport analysis, as described below. Tm consisted of three animals from the Luc-BPN delivery cohort (one from each group), as well as a separate cohort of mice receiving BTB/BBB opening with or without preconditioning 19 days following tumor implantation.

4.5.4 MR Thermometry.

MR single-slice PRF-shift-based thermometry images were acquired starting two minutes prior to initiation of FUS preconditioning procedure and continued until 4 minutes after the end of FUS

preconditioning sonication. The imaging slice was oriented axially with respect to the brain, and centered at the axial coordinate corresponding to the center of the region targeted for FUS treatment. Pulse sequence parameters for the thermometry imaging were as follows: TR/TE = 78/9.0 ms, flip angle = 40°, readout bandwidth = 80 Hz/Px, in-plane FOV = 96×96 mm, in-plane resolution = 0.75×0.75 mm, slice thickness = 2 mm, time per frame = 10 s. Temperature rise over time for each animal was obtained by taking the average temperature rise of all the sonicated pixels in each thermometry image obtained during the 10-minute preconditioning procedure. The plateau temperature rise for each animal was then calculated by averaging the temperature rise values from the final 7:30 of the sonication period. CEM43 was calculated from mean of the pixel averaged temperature rise values over the entire 10-minute treatment period.

4.5.5 MR Imaging for Transport Analysis.

For Tm, the general MR imaging protocol was varied to obtain images for interstitial tumor transport analysis. Briefly, the baseline signal intensity in the tissue was obtained via a three-dimensional T1-weighted MR image, which was acquired immediately prior to the injection of the contrast agent. Following intravenous administration of the contrast agent, a series of three T1-weighted contrast-enhanced MR images were obtained. Following FUS BTB/BBB opening (described previously), the same imaging procedure was repeated, first obtaining a T1-weighted MR image prior to reinjection of contrast to obtain baseline signal intensity for post-FUS measurements. The contrast agent was injected intravenously and a second series of three T1-weighted contrast-enhanced MR images was acquired. All T1-weighted images collected for this purpose used pulse sequence parameters identical to those of the three-dimensional spoiled gradient-echo T1-weighted sequence described above.

4.5.6 Quantification of Grayscale Intensity from MR Images.

For Luc-BPN cohort, the pre- and post-FUS contrast enhanced MR images were analyzed for grayscale intensity of gadolinium enhancement. Analysis was performed on the MR image slice corresponding to the slice targeted for FUS treatment. Two different ROIs were analyzed, one encompassing the entire FUS-targeted region, referred to as “BTB+BBB”, and one encompassing only the tumor, referred to as “BTB”. Mean pixel grayscale intensity was quantified within each of these ROIs in the pre-FUS and post-FUS images for each animal. An equivalent ROI was chosen on the contralateral side, and the grayscale intensity was subtracted as background.

4.5.7 Transport Analysis.

We analyzed the gadolinium transport in tumors similarly to the previous chapter. Briefly, each of the acquired MR imaging series were loaded into the post-processing algorithm. Background signal was removed by subtracting the pre-contrast image from the corresponding post-contrast series. A unique ROI was chosen for each animal to perform both pre- and post-FUS transport analyses. ROIs were chosen to include the entire enhancing tumor region from pre-FUS images, as well as surrounding brain tissue immediately adjacent to tumor. Analysis was performed on the MR tissue slice corresponding to the coordinate which was targeted for FUS BTB/BBB opening. The input value for time per slice for each MR imaging series was obtained by dividing the total time of image acquisition for the series by the number of images in the series. As previously described, the algorithm utilized here uses changes in gadolinium signal intensity throughout the images to estimate diffusion coefficients and interstitial fluid velocities within the selected ROI. We performed this transport analysis on tumors receiving FUS BTB/BBB opening both with and without our specified preconditioning protocols.

4.5.8 Passive Cavitation Detection Analysis.

Acoustic emissions were quantified during the 2-minute FUS + MB BTB/BBB opening protocol for Luc-BPN mice. Emissions were detected with a 2.5 mm wideband unfocused hydrophone mounted in the center of the transducer, captured using a scope card (ATS460, Alazar, Pointe-Claire, Canada), and analyzed using an in-house built MATLAB algorithm, as previously described in chapter 3. Briefly, a 0.2 kHz bandwidth filter was applied to the fundamental frequency, harmonics (2f, 3f, 4f), sub harmonic (0.5f), and ultra-harmonics (1.5f, 2.5f, 3.5f). For each frequency band, the root mean square of the peak spectral amplitude was calculated, multiplied by the individual sonication duration, and summed up over the entire treatment duration. Broadband emissions were obtained by summing the product of V_{rms} and individual sonication duration for all remaining emissions not in a specified frequency band over the entire treatment period.

4.5.9 Ex Vivo Bioluminescence Imaging of Tumors.

Bioluminescence imaging was performed three days after FUS treatments as described in the previous chapter. Briefly, D-Luciferin (Gold Biotechnology, St. Louis, MO) was administered to each mouse at a dose of 150 mg/kg via intraperitoneal injection. Mice were euthanized five minutes later via intraperitoneal injection of Euthasol. Tumor tissue was harvested and incubated for 3 minutes in a 1 mg/ml solution of D-luciferin. Samples were inserted into the IVIS spectrum and bioluminescence images were acquired using a 3-minute exposure time. ROIs were drawn in the Living Image software to encompass the entire tumor sample and photon flux was quantified as both total flux and average radiance. Reported values had the average background measurement from untreated brain tumor samples subtracted and were normalized to the BPN only group. Values are displayed as log2 fold change over the BPN only group.

4.5.10 Sensitivity Analysis.

Using the G*power software package, we performed a sensitivity analysis on the total photon flux measurements(*121*). The 3 MPa preconditioning group data was excluded due to significant heating limiting the clinical relevance of the approach. The purpose was to determine the minimum detectable effect size between the BBB only group and the 1.5 MPa preconditioning group in the context of a post-hoc multiple comparison's test of a One-way ANOVA. In the G*power software we selected sensitivity power analysis for a two-tailed t-test between two independent means. Alpha was set to 0.025 to correct for 2 multiple comparisons (BBB only group compared to each of the two other groups) and power was set to 0.8. A sample size (n) of 5 for each group was input to reflect the experimental design. A plot for total n values (n/2 per group) versus effect size was generated for n values from 10 to 100. For each effect size of interest we were able to use the Cohen's D effect size formula and pooled standard deviations of the two groups to calculate the detectable mean difference(*122*). The mean difference was converted to a fold-change by inputting the mean value of the BBB only group measured in our study.

4.6 Chapter 4 Figures

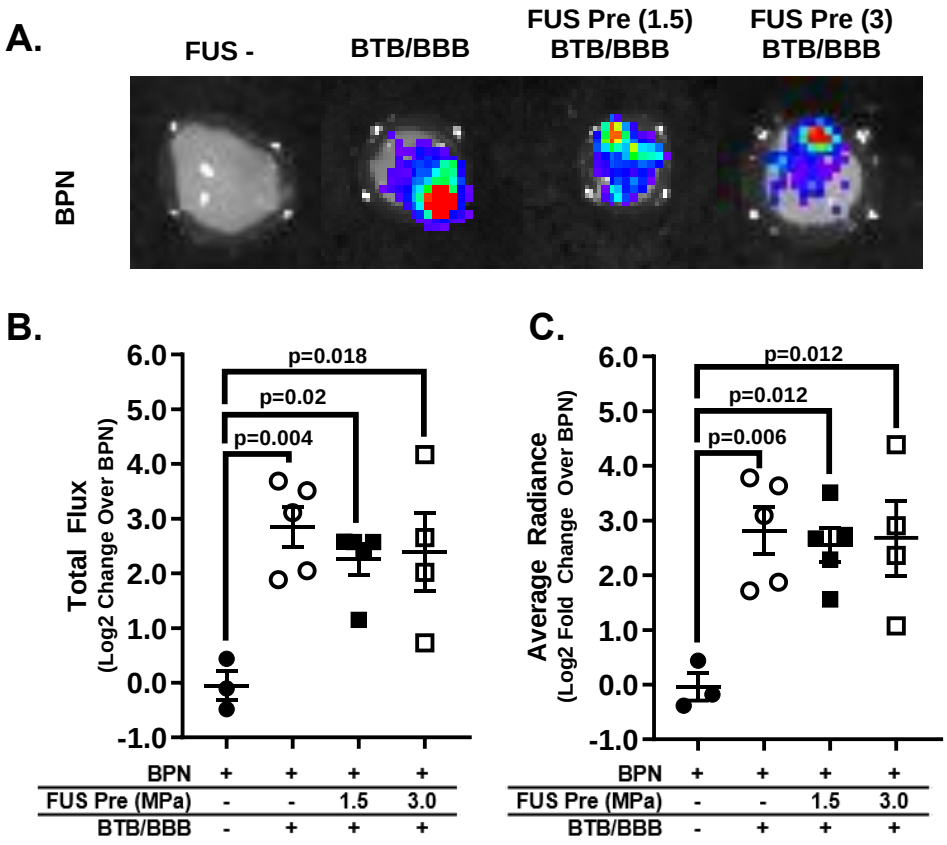

Figure 4.1. U87 Brain Tumor Transfection Levels with and without FUS Preconditioning. A: Representative *ex vivo* bioluminescence images of U87 glioma tumor tissue 3 days following treatment. **B, C:** Scatter plots of *ex vivo* bioluminescence measurements expressed as total flux (B) and average radiance (C). Mean ± SEM. Significance assessed by a One-Way ANOVA followed by Tukey's Multiple Comparisons Test.

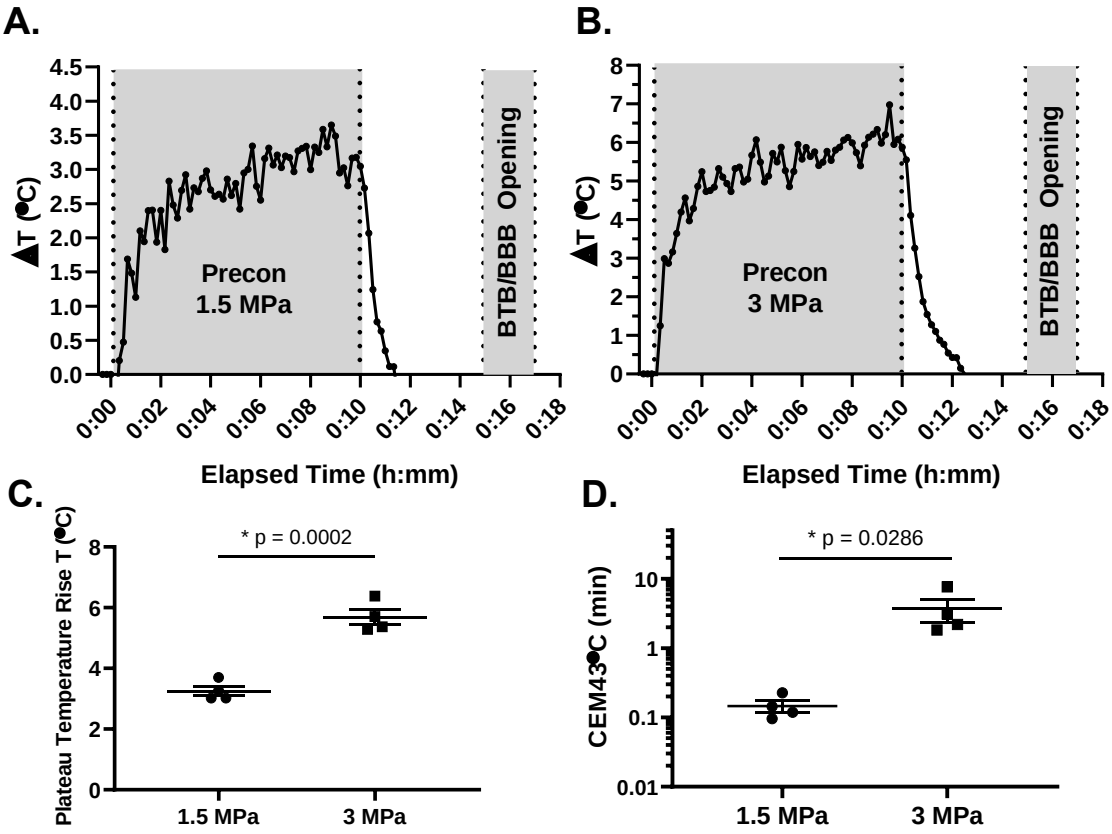

Figure 4.2. MR Thermometry Measurements During FUS Preconditioning. A, B: Representative temperature traces acquired over during (A) 1.5 MPa and (B) 3 MPa FUS preconditioning. **C, D:** Scatter plots of plateau temperature rise and CEM43°C. Mean ± S.E.M. Significance assessed via (C) unpaired T test and (D) Mann Whitney test.

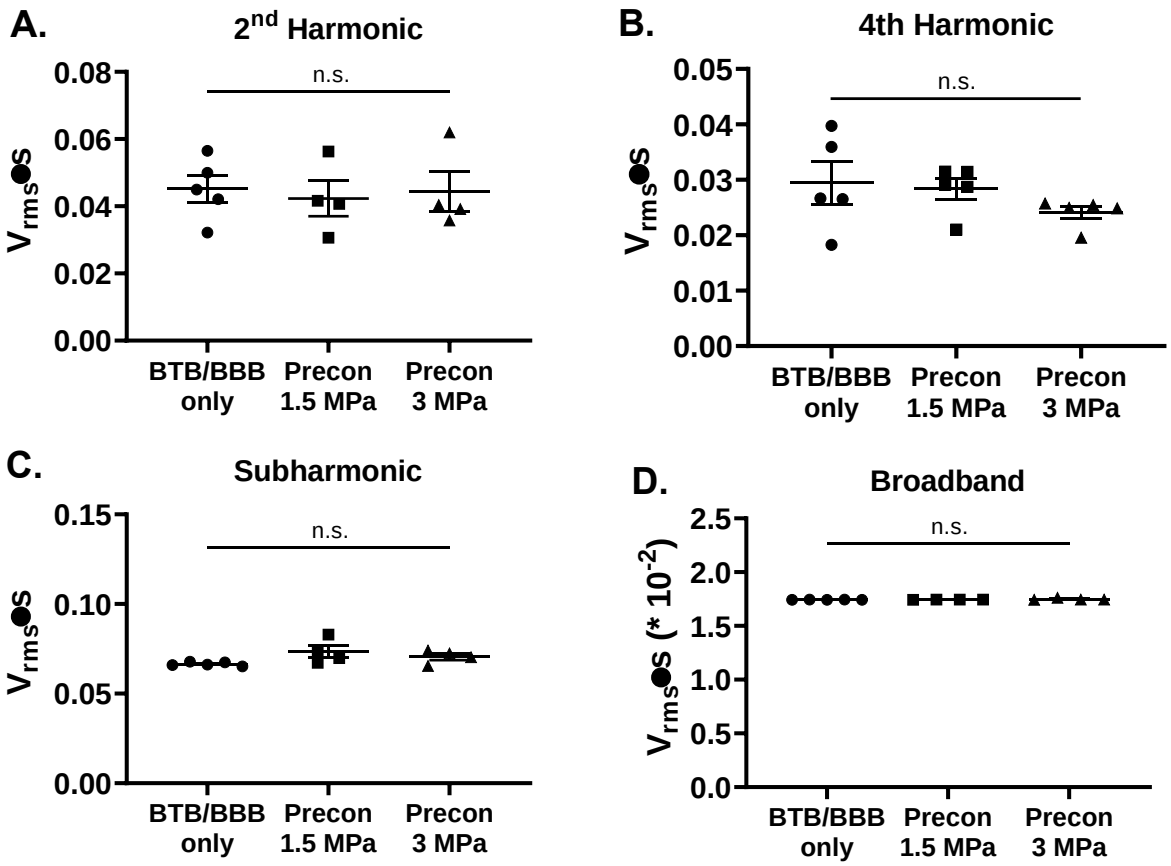

Figure 4.3. Acoustic Emissions During FUS + MB BTB/BBB Opening with and without Preconditioning. A, B, C, D: Quantification of acoustic emissions at the 2nd Harmonic (A), 4th Harmonic (B), Subharmonic (C), and broadband emissions (D). Significance assessed using One-way ANOVAs.

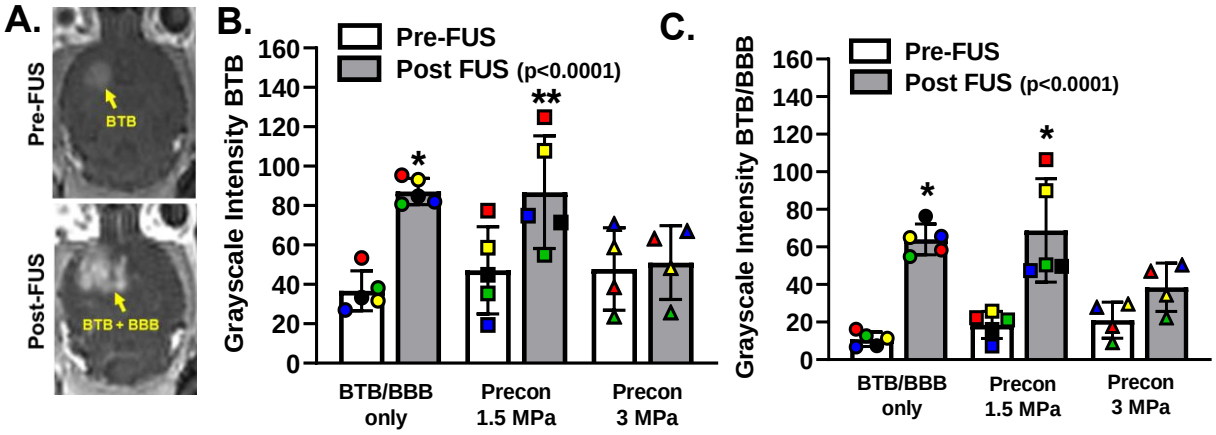

Figure 4.4. Confirmation of BTB/BBB Opening Following FUS Treatment. A: Representative Pre-FUS and Post-FUS T1-weighted contrast enhanced MR images (BTB/BBB opening only group). Yellow arrow on Pre-FUS image indicates the tumor and represents ROI used to quantify BTB opening, whereas the yellow arrow on the Post-FUS image indicates FUS-treated tissue and represents the ROI used for quantification of BTB/BBB opening. **B, C:** Bar graph showing quantification of pre and post-FUS grayscale intensity for the BTB (B) and the BTB/BBB (C). Mean ± S.E.M. Paired data points are denoted by common colors and shapes. Significance assessed using a Two-Way Repeated Measures ANOVA, followed by Sidak's Multiple Comparisons Test, *p<0.0001, **p = 0.0001.

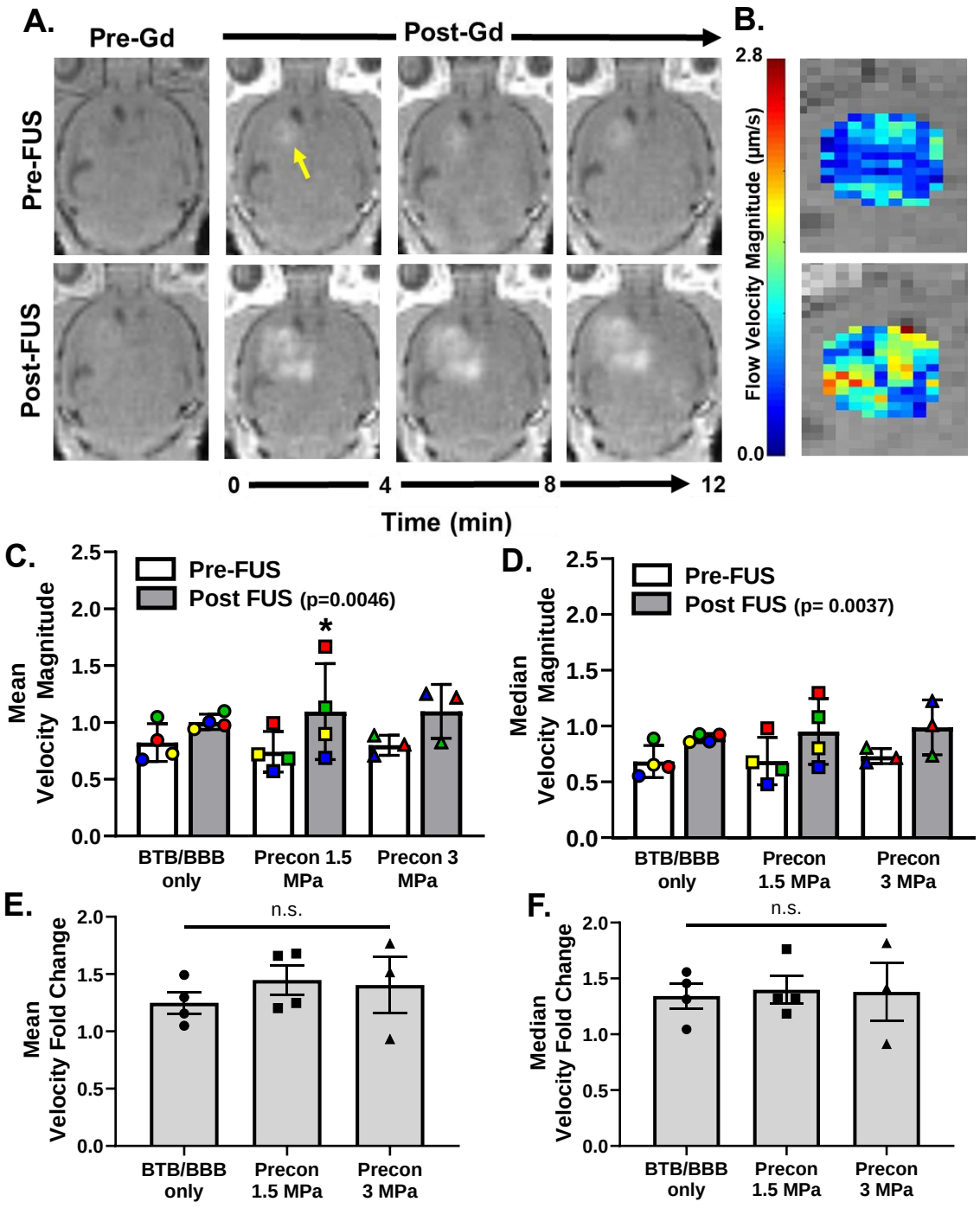

Figure 4.5. FUS Preconditioning Does Not Alter Change in Post-FUS Interstitial Fluid Velocity. A: Representative T1-weighted pre-FUS and post-FUS T1-weighted MR imaging series used for transport analysis (from animal in the1.5 MPa Preconditioning group). **B:** Pre and Post-FUS interstitial flow velocity magnitude maps obtained from transport analysis (from same animal shown in A). **C, D:** Bar graphs showing mean (C) and median (D) interstitial fluid velocity magnitude. Mean ± S.E.M. Paired data points are denoted by common colors and shapes. Significance assessed by Two-way repeated measures ANOVA followed by Sidak's Multiple Comparisons Test. *p = 0.0499.

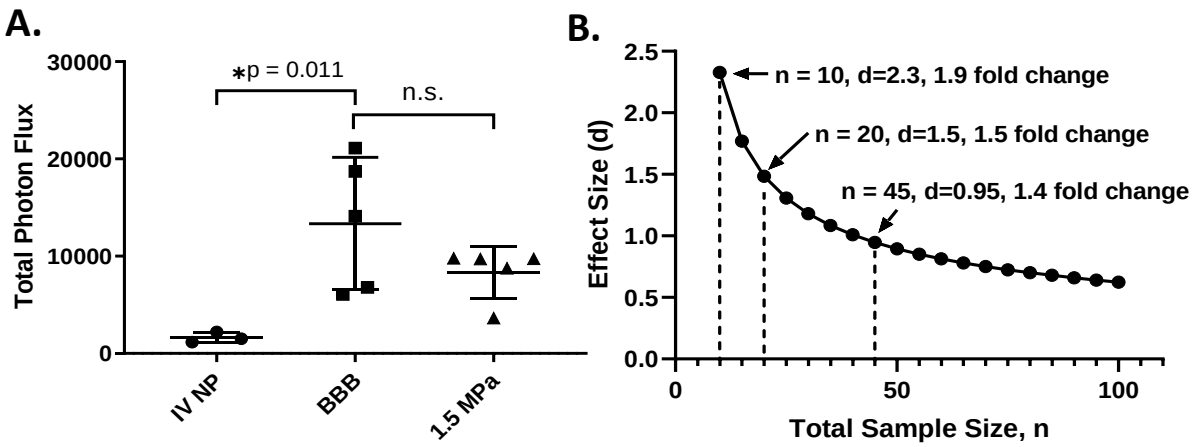

Figure 4.6. Sensitivity Power Analysis. A: Scatter plot of *ex vivo* bioluminescence measurements expressed as total photon flux. Mean ± SEM. Significance assess by a One-Way ANOVA followed by Tukey's Multiple Comparisons Test of each group compared to BBB only. B: Plot of total sample size vs. Cohen's d effect size for post-hoc comparison of BBB only to 1.5 MPa, in the context of Post-Hoc testing performed in (A).

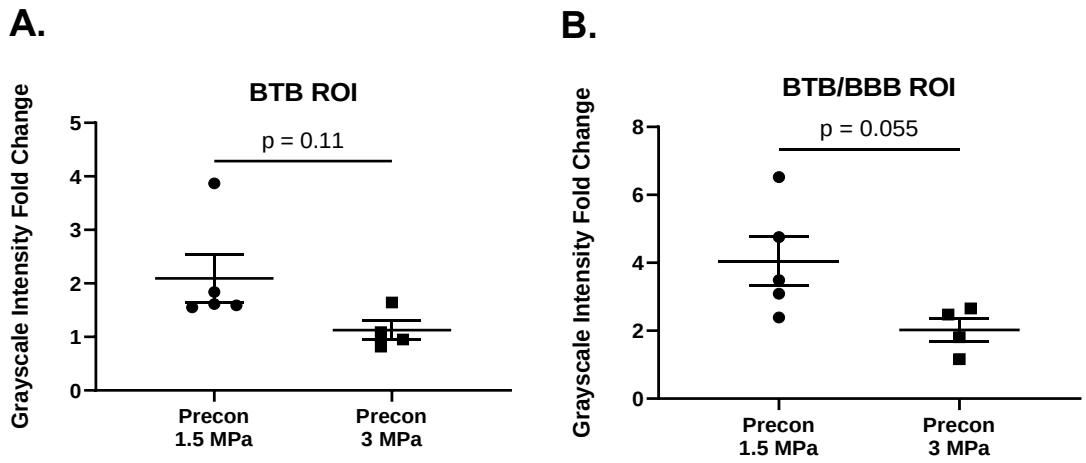

Figure 4.S1. Comparison of Grayscale Intensity Fold Change in FUS Preconditioning Groups. A, B: Scatter plots of post-FUS grayscale intensity fold change for the two preconditioning groups. Analysis performed for the (A) BTB ROI and the (B) BTB/BBB ROI. Mean ± S.E.M, significance assessed using (A) the non-parametric Mann Whitney test and (B) an unpaired t test.

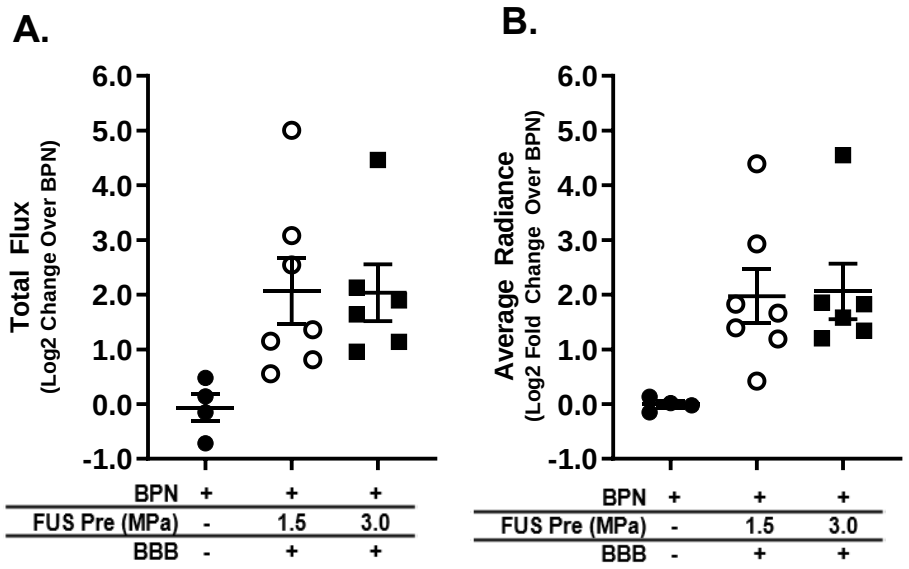

Figure 4.S2. U87 Transfection Levels with and without FUS Preconditioning in Day 7 Tumors. A, B: Scatter plots of *ex vivo* bioluminescence measurements expressed as total flux (A) and average radiance (B). Tumors treated at day 7 post implantation and imaged 3 days after treatment. Mean ± SEM.

Chapter 5: Immunomodulatory Effects of FUS + MB BTB/BBB Opening in Intracranial Melanoma Tumors

5.1 Abstract

The activation of microbubbles (MBs) with pulsed focused ultrasound (FUS) for blood-brain and blood-tumor barrier (BTB/BBB) opening permits the image-targeted delivery of therapeutic agents to brain tissue. While several studies have investigated the acute effects of FUS-mediated BBB opening on normal brain tissue, similar studies are lacking in the context of intracranial tumors. Furthermore, given the current progression of this technology into clinical trials for patients with metastatic brain tumors and the appeal of using this approach in combination with traditional and immune based therapies, it is crucial to understand how this FUS-mediated BTB/BBB opening modulates the tissue at a molecular level.

Here, we first elucidate how FUS-induced opening of the BTB/BBB in intracranial melanomas (B16F1cOVA) alters the gene expression signatures within the tissue. Using bulk RNA sequencing of tumor tissue, we found increased expression of genes related to proinflammatory cytokine and chemokine signaling, pattern recognition receptor signaling, and antigen processing and presentation. Next, we use flow cytometry analysis to assess the innate immune cell populations within the tumor, meninges, and CNS draining lymph nodes of FUS-treated animals. These studies revealed alterations in antigen loading within the dendritic cells in the tumor and meninges, as well as increased expression of the DC maturation marker CD86 in the meninges. However, we found no significant changes in cell numbers in the tumors or meninges, and no evidence of enhanced DC maturation in the tumor or draining lymph nodes of FUS-treated animals. Staining for the MHC-SIINFEKL peptide complex on DCs showed no significant changes in the analyzed tissues; however, we observed a trend towards increased MHC-SIINFEKL peptide complex expression on the DCs of the superficial cervical lymph nodes of FUS-treated animals. Lastly, we found no differences in adhesion molecule expression on tumor endothelial cells or homing of activated T cells in FUS-treated animals. We conclude that, while FUS-mediated BTB/BBB opening of immunogenic intracranial B16F1cOVA tumors with a clinically relevant paradigm elicits some signatures of inflammation, the response is mild,

transient, and unlikely to elicit a systemic response against the tumor independent of administration of immune adjuvants.

5.2 Introduction

Secondary brain tumors, arising from metastatic spread of extracranial malignancies, are the most common type of brain tumor(*14*). Up to 20% of cancer patients develop brain metastases, and this number will only increase as treatments for primary disease extend patient survival(*3*). Malignant melanoma has one of the highest propensities for metastasizing to the brain(*125*). Following the development of brain metastases, patients are faced with a significantly worse prognosis and limited treatment options. Immune checkpoint inhibitors are a class of immunotherapeutic antibodies that have shown remarkable success in a subset of melanoma patients, and recent evidence has demonstrated some efficacy for these therapies in patients with metastatic brain tumors(*126*, *127*). Still, questions remain regarding the ability of these agents to penetrate the brain parenchyma due to the blood-tumor barrier and the ability of brain tumors to respond, given their unique immunological milieu.

A number of factors may contribute to poor penetration and limited efficacy of therapeutics in secondary brain tumors. Like primary brain tumors, metastatic brain tumors develop leaky vasculature. This results in high interstitial fluid pressure and limited convective transport of agents into the tissue, referred to as the blood-tumor barrier(BTB)(*14*). Despite regions of high vascular permeability, studies have shown varying permeability between, and even within, single metastatic lesions(*13*). Additionally, delivery of therapeutic agents to brain metastases is significantly lower compared to peripheral metastases, possibly owing to retention of blood-brain barrier-like properties within a subset of vessels(*14*). Beyond challenges to effective therapeutic delivery, the brain has long been thought of as immunologically quiescent. Given these limitations, methods that may improve penetration and efficacy of immunotherapeutics in metastatic brain tumors are greatly needed.

Focused ultrasound applied in the presence of circulating microbubbles has the ability to improve delivery and penetration of agents into brain tumor tissue, and therefore is an attractive modality for use in combination with traditional and immune based therapies targeted to

intracranial tumors(*40*, *58*). Clinical trials have proven safety and efficacy of FUS + MB BBB and/or BTB opening in human patients with Alzheimer's disease, ALS, and glioblastoma, with a study currently underway in patients with brain metastases of Her2+ breast cancer (NCT03714243)(*29–31*). Additionally, it is possible that FUS + MB BTB opening can modulate the immune microenvironment, which could augment the efficacy of immune-targeted therapies. In normal brain tissue, FUS + MB BBB opening was shown to induce a sterile inflammatory response, with acute release of damage-associated molecular patterns(DAMPs), proinflammatory cytokines and chemokines, and trophic factors(*96*). This response was mostly resolved within 24 hours of treatment.

Given the potential for FUS to be used along with immunotherapeutic agents, as well as the progression of FUS into clinical trials of patients with metastatic brain tumors, it is important to understand how FUS modulates the immune landscape of secondary brain tumors. Here, we investigate the effects of FUS + MB BTB/BBB opening on several aspects of the melanoma brain tumor immune microenvironment, as well as effects in the meninges and draining lymph nodes. First, we used bulk RNA sequencing of treated and untreated intracranial B16F1cOVA (B16 melanoma tumor cells that express the chicken ovalbumin antigen with the secretion sequence deleted) to profile FUS-induced changes of the tumor tissue transcriptome 6 and 24 hours post treatment. Sequencing revealed increased RNA expression of several proinflammatory cytokines and chemokines, pattern recognition receptors, MHC class I genes, elements involved in processing and presentation of peptide antigens via MHC class I in FUS-treated tumors. These results suggested alterations in the innate immune cell infiltrates in the tumor and/or associated secondary lymphoid tissue, such as the meninges and tumor-draining lymph nodes. Therefore, we utilized a similar B16 cell line expressing ZsGreen as a fusion protein with the immunodominant MHC class I and class II peptide epitopes derived from OVA to assess FUS-induced changes in these cell population. Specifically, we performed flow cytometry to evaluate innate immune cell numbers, dendritic cell expression of maturation

markers, and dendritic cell tumor antigen uptake and presentation in FUS-treated tumors(*128*). We detected an increase in CD11b+ myeloid cells in the deep cervical lymph nodes (DCLNs) two days following FUS treatment, which could be due to recruitment to the tumor draining site based on release of chemotactic factors. We observed increased CD86 expression and decreased ZsGreen antigen load in the meningeal dendritic cells 2 days post FUS, supporting the notion that FUS has the ability to modulate maturation of DCs. We also found an increased percentage of ZsGreen positive dendritic cells in FUS-treated tumors two days post FUS, suggesting increased antigen uptake or exposure. There were no significant changes in cell numbers in the tumors, meninges, or superficial cervical lymph nodes (SLNs), and no evidence of enhanced DC maturation in the tumor or draining lymph nodes of FUS-treated animals either 2 or 4 days following treatment. Additionally, we stained for the SIINFEKL peptide-MHC class I (H-2K^{b}) complex on DCs (MHC-SIINFEKL), a marker for presentation of the OVA257-364 peptide via MHC I. We found no significant changes in the analyzed tissues at either timepoint; however, we observed a trend towards increased MHC-SIINFEKL expression on the DCs of the superficial cervical lymph nodes of FUS-treated animals. Lastly, based on the previously observed FUS-mediated transcriptional changes in proinflammatory cytokines, we tested whether FUS could lead to enhanced homing of activated T cells to the tumor site. We found no changes in expression of cell adhesion molecules on tumor endothelial cells and no changes in activated T cell homing in FUS-treated tumors/meninges 24 hours post sonication.

5.3 Results

5.3.1 Confirmation of FUS + MB BTB/BBB Opening in B16F1cOVA Tumors.

Figure 1 shows T1-weighted gadolinium enhanced MR images acquired pre- and post-FUS BTB/BBB opening in a B16F1cOVA brain tumor. The enhancing region in the pre-FUS image

corresponds to the brain tumor, whereas the larger enhancing region in the post-FUS image signifies enhanced gadolinium delivery, and thus successful BTB/BBB disruption.

5.3.2 Differentially Expressed mRNA Transcripts in FUS-Treated Tumors at 6 Hours and 24 Hours via RNA Sequencing.

RNA sequencing was performed on FUS-treated and sham intracranial melanoma tumors samples harvested 6 and 24 hours following treatment. Figure 2A shows the global gene expression of all samples plotted with respect to the first two principal components. For the 6 hour samples there is clustering of the FUS-treated and sham samples, demonstrating that FUS treatment is accounting for a significant amount of variation within gene expression of these samples. At 24 hours, there is significant overlap of the treated and untreated samples, suggesting that FUS perturbation of gene expression is almost resolved at 24 hours. In FUS-treated tumors, there were 203 transcripts that were significantly differentially expressed at the 6 hour time point and 37 transcripts at 24 hours, as shown in Figure 2B and 2C. Several transcripts for solute carrier proteins, as well as blood-brain barrier related transcripts were differentially expressed in tumors 6 hours post-FUS, shown in Figure 3A. Figure 3B and 3C show differential gene expression data from selected proinflammatory cytokines (3B) and chemokines/vascular cell adhesion molecules involved in immune cell recruitment (3C). Lastly, differential expression of genes related to pattern recognition receptor signaling and MHC class I antigen processing are shown in Figure 3D and 3E, respectively.

5.3.3 Differentially Expressed Pathways in FUS-Treated Tumors at 6 Hours and 24 Hours Post-Treatment.

Gene set enrichment analysis of RNA sequencing data revealed numerous differentially expressed pathways in FUS-treated tumors at 6 hours and 24 hours post-treatment. Figure 4

shows normalized enrichment scores (NES) for significantly enriched gene sets related to specific aspects of the proinflammatory response in the tumor. Specifically, gene sets associated with proinflammatory cytokine signaling, chemokine signaling and chemotaxis, pattern recognition receptor signaling, and antigen processing and presentation are highlighted due to possible roles in supporting generation of an antitumor immune response.

5.3.4 Immune Cell Representation in Tumors, Meninges, and Draining Lymph Nodes of Intracranial B16ZsGreenOVA Tumor Bearing Animals with and without FUS + MB BTB/BBB Opening.

Given the increased expression of numerous proinflammatory cytokines, including IL6 and TNF, and chemokines involved in immune cell chemotaxis, we were interested in looking at the numbers of innate immune cells and lymphocytes in the tissue via flow cytometry. We observed no changes in any of the evaluated cell types, which included dendritic cells (CD11c hi) and myeloid cells (CD11b+), as well as specific cellular subsets of dendritic cells (CD11c hi CD11b+ and CD11c hi CD103+) and myeloid cells(macrophages: CD11b+ F4/80+, monocytic myeloid cells: CD11b+ Ly6C hi, and granulocytic myeloid cells: CD11b+ Ly6C mid) in FUS-treated tumors two days and four days post treatment (Figure 5). Additionally, we saw no significant changes abundance of these cell populations at either time point in the meninges of FUS-treated animals, shown in Figure 6. We also looked at both the deep cervical (DCLNs) and superficial cervical lymph nodes (SLNs), which are considered to be CNS-draining lymph nodes(*129*). We observed a significant increase in the myeloid (CD11b+) cell population in the DCLNs of sonicated animals 2 days after treatment (Figure 7B). Additionally, there was a trend towards increased numbers of dendritic cells, as well as the macrophages and granulocytic myeloid cells 2 days post-FUS in the DCLN, but no changes were seen at the later time point (Figure 7A, C- E). While these changes are interesting, we should be cautious of these

observations given the low overall cell numbers isolated from the DCLNs. No differences were observed in the SLNs at either time point (Figure 8). Staining for markers of conventional CD11b+ and CD103+ dendritic cells revealed that the CD11c hi dendritic cell population in all assessed organs was primarily composed of CD11b+ dendritic cells. This is consistent with the literature reporting that CD103+ DCs make up a minority of myeloid cells in human and mouse tumors(*130*). (Figures 5,6,8, subset information not shown for DCLNs due to low cell numbers).

5.3.5 Expression of Specific DC Activation Markers in Intracranial B16ZsGreenOVA Tumors with and without FUS + MB BTB/BBB Opening.

The gene set enrichment analysis of the RNA sequencing data revealing a significant increase in pattern recognition receptor signaling in tumors at both 6 and 24 hour post FUS. Specifically, the leading edge of this pathway included significantly increased expression of pattern recognition receptor genes Clec7a and CD14 and TLR signaling adaptor protein Pik3ap1 (Figure 3E)(*131–134*). These expression signatures support the notion that damage-associated molecular patterns (DAMPs) may be produced and/or released in response to FUS modulation of the tissue, which can activate dendritic cells through these pattern recognition receptors. Since dendritic cells are antigen-presenting cells crucial to initiation of an antitumor immune response, we stained for CD86 and MHC II expression on dendritic cells to assess maturation state. In the tumor-resident dendritic cells, we observed no changes in CD86 at either time point and no changes MHC II expression 4 days after treatment, as shown in Figure 9. In the meninges, we observed no changes in the proportion of DCs expressing CD86, but there was a significant increase in the amount of CD86 expressed in CD86+ DCs two days post FUS, with no changes observed at 4 days (Figure 10A, B). No differences were seen in MHC II expression in DCs at day 4 post treatment (Figure 10C, D). Additionally, we observed no significant

changes in expression of either marker in the DC population within the deep cervical and superficial cervical lymph nodes (Figure 11, Figure 12A-E).

5.3.6 Antigen Uptake and Presentation in DCs in Intracranial B16ZsGreenOVA Tumor-Bearing Animals with and without FUS + MB BTB/BBB Opening.

RNA sequencing indicated significant upregulation of several genes related to antigen processing and presentation. These genes included the subunit of the immunoproteasome PSMB8, which preferentially processes peptides for presentation on MHC class I, TAP1 and TAP2 transporters involved in shuttling of peptides into the endoplasmic reticulum for MHC class I loading, and classical MHC I genes H2-K1 and H2-D1(Figure 3D)(*135*, *136*). Additionally, gene set enrichment analysis showed a significant increase in antigen processing and presentation of exogenous peptide via MHC class 1 molecules in FUS-treated tumors. For this reason, we aimed to assess antigen uptake and presentation in DCs of FUS-treated animals compared to control. Tumor cells used in these studies were stably transfected to express MHC-restricted peptides derived from OVA in frame with ZsGreen fluorescent protein, allowing us to use ZsGreen fluorescence as a marker for antigen uptake in the tumor and meningeal DCs. Additionally, we stained for the SIINFEKL peptide MHC class I (H-2K^{b}) complex on DCs, a marker for presentation of the OVA257-364 peptide via MHC I. In tumor tissue we detected an increased percentage of ZsGreen positive CD11c hi dendritic cells two days after FUS treatment, but no difference was seen in ZsGreen geometric mean fluorescence (GMF) in this population (Figure 13A, B). The increase was driven by the CD11b+ dendritic cell subset (Figure 13C, D). We saw no changes in MHC-SIINFEKL staining on DCs in the tumor (Figure 13E, F). In the meninges, there were no changes in percentage of ZsGreen+ DCs, or MHC-SIINFEKL staining, however there was a significant decrease in ZsGreen GMF two days post

FUS (Figure 14). There was a strong trend towards increased MHC-SIINFEKL staining in the superficial lymph node DCs 2 days post FUS (Figure 12F).

5.3.7 Endothelial Cell Adhesion Molecule Expression in Intracranial B16ZsGreenOVA Tumors with and without FUS + MB BTB/BBB Opening.

We stained for expression of cell adhesion molecules E-selectin, ICAM-1, and VCAM-1 on tumor endothelial cells (CD31+ population) 24 hours post FUS + MB BTB/BBB opening in intracranial B16F1cOVA and B16F1 tumors. In B16F1cOVA tumors, we saw no differences in percentage of endothelial cells expressing the assessed cell adhesion molecules in FUS-treated tumors (Figure 15A-C). In the less immunogenic B16F1 tumors, we found a significant decrease in the percentage of endothelial cells expressing E-selectin in FUS-treated tumors (Figure 15D); however, we saw no changes in the other two cell adhesion molecules (Figure 15E, F).

5.3.8 Activated T cell homing in B16ZsGreenOVA Tumors and Meninges with and without FUS + MB BTB/BBB Opening.

Results from RNA sequencing showed increased expression of proinflammatory cytokines and chemokines 6 hours post FUS. We were interested in whether FUS treatment could enhance the ability of activated T cells to home to the tumor site, possibly through release of these soluble mediators. To test this, we performed FUS + MB BTB/BBB opening in both B16F1cOVA and B16F1 tumors 6 days after tumor implantation. The following day, roughly 24 hours post treatment, a mixture of activated Pmel T cells and activated non-specific T cells was adoptively transferred a via tail vein injection. Pmel T cells are T cells isolated from Pmel transgenic mice. These cells express T cell receptors specific for the melanoma antigen gp100, which is expressed in both B16F1cOVA and B16F1 cell lines. Tumors and meninges were harvested 5 hours after adoptive cell transfer and transferred cell numbers in these tissues were assess via

flow cytometry. Cell numbers were normalized to the number of transferred cells in the spleen to account for variations in the injection. We found no differences in the number of activated Pmel or non-specific T cells in the tumor or meninges of either tumor type (Figure 16).

5.4 Discussion

In this study we characterized the effect of FUS + MB BTB/BBB opening in intracranial melanoma tumors on multiple facets of the immune landscape in the tumor, meninges, and CNS draining lymph nodes. Bulk RNA sequencing of tumor tissue revealed increased expression of several proinflammatory cytokines and chemokines, as well as genes involved in pattern recognition receptor signaling and antigen processing and presentation via MHC class I in FUS-treated tumors. We then utilized a similar B16 cell line expressing ZsGreen tagged MHC class I and class II dominant OVA peptides to assess FUS effects on innate immune cell numbers, dendritic cell expression of maturation markers, and dendritic cell tumor antigen uptake and presentation via flow cytometry. We found an increased number of CD11b+ myeloid cells in the DCLN 48 hours after treatment, as well as increased CD86 expression and decreased ZsGreen antigen load in the meningeal dendritic cell population. The percentage of ZsGreen-positive dendritic cells in FUS-treated tumors was increased two days post FUS, suggesting enhanced antigen uptake or exposure. Lastly, we tested whether FUS + MB BTB/BBB opening could enhance expression of endothelial cell adhesion molecules or homing of subsequently administered activated T cells to the tumor site. We found no changes in expression of cell adhesion molecules on tumor endothelial cells and no changes in activated T cell homing in FUS-treated tumors/meninges 24 hours post sonication. Here we observed that FUS-mediated BTB/BBB opening of immunogenic intracranial B16F1cOVA tumors elicits some signatures of inflammation. Ultimately, however, the response is mild, transient, and unlikely to elicit a systemic response against the tumor without administration of immune adjuvants.

5.4.1 Comparison of Response to MB Activation with FUS in Brain Tumors to Normal Brain Tissue

Despite vast differences between brain tumor tissue and normal brain, we observed proinflammatory signatures in FUS-treated tumors similar to the sterile inflammatory response (SIR) previously described in normal brain tissue(*96*, *98*). Since the blood-brain barrier is meant to maintain homeostasis in the brain, BBB disruption by any means represents a significant perturbation of the local microenvironment. For instance, BBB opening alters the ionic balance in the tissue and facilitates extravasation of serum proteins, which can induce cellular stress responses and activation of microglia(*137*). Additionally, if applied with enough energy, FUS may induce mechanical damage in neurons and astrocytes, all which may yield the release of damage-associated molecular patterns (DAMPs) to initiate the SIR cascade. In contrast, within brain tumors, the blood-brain barrier is already disrupted, cells are rapidly dividing and exposed to solid and mechanical stresses, and the microenvironment is characterized by tumor mediated immunosuppression. Despite these differences, we similarly observed a transient proinflammatory response in the tissue, characterized by increased proinflammatory cytokine, chemokine, and cell adhesion molecule transcripts 6 hours post-FUS, which included TNF, IL-6, Ccl2, Ccl12, Cxcl10, Cxcl1, and Icam-1. We did not, however, see increases in e-selectin or p-selectin at the RNA level, as seen in normal brain tissue. Additionally, gene set enrichment analysis of our RNA sequencing data provided evidence for increased pattern recognition receptor signaling (likely in response to DAMPs), interferon gamma mediated signaling, and NF-kappa B signaling, consistent with observations at the RNA and protein level in normal brain tissue(*96*).

Since we saw increased expression of several cytokines implicated in stimulation of cell adhesion molecule expression and observed increased Icam-1 at the RNA level, we also assessed protein expression of cell adhesion molecules on tumor endothelial cells 24 hours post-FUS. We did not see differences in protein expression of E-selectin, Icam-1, or Vcam-1.

While the previous study in normal brain tissue did not report protein data on E-selectin or Vcam-1, investigators reported a 4-fold increase in Icam-1 protein 24 hours post FUS BBB opening, whereas here we saw no change in Icam-1 protein expression 24 hours post FUS (despite detecting an elevation at the transcript level 6 hours post-FUS)(*96*). It is possible that even with increases in cytokines following FUS treatment, brain tumor endothelial cells do not respond to these stimuli in the same manner as normal vasculature. Furthermore, we saw higher expression of these cell adhesion molecules in B16F1cOVA tumors compared to contralateral brain tissue (data not shown), suggesting that the tumor endothelial cells may already be in a more activated state. Thus, further activation by FUS-induced cytokines may not be possible.

5.4.2 Putative Antigen-Presenting Cell Response Mechanisms

FUS + MB BTB/BBB opening induced increases in several chemokine transcripts involved in innate immune cell chemotaxis; however, we observed few changes in cell numbers in the tumor, meninges, and tumor-draining lymph nodes of FUS-treated animals compared to control. Two days after FUS treatment, there was a significant increase in the overall myeloid cell population in the deep cervical lymph nodes. Additionally, there were general trends towards increased dendritic cells (CD11c hi), macrophages (CD11b+ F4/80+), and granulocytic myeloid cells (CD11b+ Ly6C mid) in the DCLNs of FUS-treated animals 48 hours post treatment. Increases could be due to the chemokine (such as CCL2) induced innate immune cell recruitment through high endothelial venules and/or TNF and IL-6 mediated retention of cells in the draining lymph node site of the inflammatory insult(*138–140*). However, given the low overall cell number isolated from the DCLNs, it is important to note that these differences may not be physiologically meaningful. Additionally, within the tumor site, we observed trends toward increased dendritic cell and myeloid cell numbers 4 days post FUS, suggesting possible

recruitment into the site of inflammation. Since we are only seeing snapshots of overall cell numbers at particular time points, more direct experiments would be needed to make definitive conclusions about FUS-induced changes in cell trafficking.

Dendritic cells are professional antigen-presenting cells that act as a bridge between the innate and adaptive immune system; therefore, these cells are commonly recognized as the most important antigen-presenting cells in the generation of an antitumor immune response(*102*). In peripheral tissue, DCs exist in an immature form in which they primarily endocytose materials and accumulate antigens. Immature DCs are poor antigen presenters and may even contribute to tolerance. Molecules such as PAMPs and DAMPs activate pattern recognition receptors on dendritic cells, providing a maturation stimulus. Additionally, upon maturation DCs downregulate endocytosis, activate machinery involved in antigen processing and presentation and thus express higher levels of MHC-peptide complexes, and increase expression of T cell co-stimulatory molecules, making them effective T cell activators(*102*). Here we observed enhanced gene expression signatures related to pattern recognition receptor signaling and antigen processing and presentation both 6 and 24 hours following FUS treatment via bulk RNA sequencing. Based on these changes, we chose to interrogate several aspects of the DC population in the tumor, as well as in the meninges and tumor draining lymph nodes. Though further experiments would be needed to examine whether expression signatures in the meninges and lymph nodes mirror those seen in the tumor, it is possible that these sites are exposed to soluble factors released in the tumor upon FUS treatment and may also exhibit responses in the DC population. Furthermore, upon maturation, DCs are known to migrate to draining lymph nodes, thus it is possible that DCs from the tumor site are trafficking to the meninges, DCLNs, and SLNs, which could manifest as changes in the DC populations of these tissues. These characteristics highlight the importance considering the dynamic nature of these cell populations when interpreting these results.

First, since stimulation of pattern recognition receptors via damage-associated molecular patterns (DAMPs) can stimulate dendritic cell maturation, we assessed expression of two DC maturation markers, CD86 and MHC II. Two days after treatment, the meningeal dendritic cell population expressed significantly higher levels of CD86, a T cell costimulatory molecule that is upregulated upon maturation. It is unclear why CD86 expression was increased in the meninges, but not the tumor or draining lymph nodes of FUS-treated animals. As mentioned previously, dendritic cell maturation can prompt DC migration to the lymph nodes, so it is possible that once DCs in the tumor receive the maturation stimulus they migrate away from the tumor site, thus we are unable detect changes in maturation within the tumor DC population. This could be the source of the DCs expressing increased levels of CD86 in the meninges. However, here we do not detect increased DC maturity in the draining lymph nodes of FUS-treated animals, as would be expected if matured DCs were trafficking to the nodes. To further interrogate these questions, we could perform experiments dedicated studying DC trafficking in response to FUS + MB BTB/BBB opening.

Additionally, we looked at ZsGreen uptake and MHC-SIINFEKL expression to assess antigen uptake and presentation. Along with increased CD86 expression, the dendritic cells isolated from the meninges showed lower ZsGreen fluorescence. This could be due to degradation of the antigen, and indicative of a switch from an immature phagocytic phenotype to a more mature phenotype for lymphocyte priming(*102*). The increased percentage of ZsGreen-positive dendritic cells in the tumors of FUS-treated mice suggests increased antigen exposure or availability within the tumor following FUS. Factors such as increased antigen from cell death, increased phagocytosis, or enhanced distribution of antigen throughout the tumor from FUS-induced changes in interstitial transport (as elucidated in chapter 3 of this dissertation) could contribute to this finding. Staining for the MHC-SIINFEKL complex on dendritic cells revealed a trend towards increased abundance within the superficial cervical lymph nodes of FUS-treated animals. If dendritic cells within the tumor have increased processing and presentation of

peptide antigen via MHC class I, as detected via RNA seq, they could then traffic to the lymph nodes where they can display MHC-SIINFEKL complexes.

5.4.3 MHC Class I Molecule Response and Mechanisms

RNA sequencing revealed that at 6 hours post FUS the increased expression of both classical MHC I molecules, H2-K1 and H2-D1. In fact, H2-K1, the MHC class I molecule that presents the OVA257-264 peptide, was the most significantly differentially expressed gene in FUS-treated tumors at the 6 hour time point. As discussed previously, this could be due to increased expression on antigen-presenting cells such as dendritic cells, which would be beneficial for priming of an antitumor immune response. However, it is also possible that the tumor cells are upregulating expression of class I MHC molecules. Furthermore, the increased gene signatures related to antigen processing and presentation could also be occurring in the tumor cells, as opposed to antigen-presenting cells. This fits with the fact that we did not see increased expression of the MHC-SIINFEKL complex on DCs within the tumor or meninges. Future studies should determine whether this response is occurring in tumor cells, as this could also be beneficial to anti-tumor immunity by making the tumor cells more visible to tumor specific effector T cells. It is known that downregulation of MHC I expression is one mechanism used by tumor cells to evade detection by the immune system(*141–144*). Expression of MHC I and genes involved in antigen processing in presentation have been shown to be increased in response to type I and type II interferons(*135*, *145*). Though we did not observe an increase of IFN gamma, alpha, or beta at the transcript level, gene set enrichment indicated increased interferon gamma and type I interferon signaling. Thus, it is possible that an acute release of interferons led to increased MHC I expression and expression of genes related to antigen processing and presentation in the tumor and/or tumor-infiltrating immune cell populations(*135*, *145*).

5.4.4 Microglial Responses to FUS + MB BTB/BBB Opening

Here, we have focused mostly on studying responses in the dendritic cell population due to their importance in bridging innate and adaptive immunity and generating antitumor responses; however, other cell types in the brain may be important in responding to FUS in brain tumors. Microglia and perivascular macrophages express pattern recognition receptors, and therefore have the ability to respond to DAMPs(*146*, *147*)(*133*). Stimulation of microglia via DAMPs has been observed in response to CNS injury and infection and microglia have been shown to be activated in response to FUS + MB BBB opening in normal brain tissue(*96*)(*133*).Furthermore, microglia have been reported to also act as antigen-presenting cells in the brain parenchyma. For these reasons, future studies should interrogate the microglial cell population in response to FUS.

5.4.5 T Cell Responses to FUS + MB BTB/BBB Opening

The relatively early time points chosen here to evaluate tissue responses to FUS treatments are more conducive to detecting changes in the dendritic cell component of the anti-tumor immune response rather than T cell responses, since de novo T cell responses take longer to manifest. Given the limited and transient nature of the proinflammatory response generated by FUS, we hypothesize that we would not detect FUS-induced increases in T cell activation, however future studies could investigate this further. While we did not assess de novo T cell response, we did investigate the ability of FUS + MB BTB/BBB opening to augment homing of adoptively transferred activated T cells to intracranial melanoma tumors. We found no differences in T cell homing to tumors with FUS + MB BTB/BBB opening, but this result could be dictated by the timing of the adoptive transfer relative to the FUS treatment as well as the time of the tissue harvest. For instance, accumulation of HER-2 specific NK-92 cells in a model of

HER2+ breast cancer brain metastasis was found to depend upon timing of the cell injection, with greater accumulation achieved when cells were administered immediately prior to FUS BTB/BBB disruption(*61*). Future studies should also investigate whether homing of activated tumor specific T cells can be enhanced by administering cells prior to FUS + MB BTB/BBB disruption.

5.5 Conclusion

In this chapter, we have used RNA sequencing and flow cytometry to assess acute immune responses to FUS + MB BTB/BBB opening in intracranial melanoma tumors. This response was characterized by enhanced gene signatures related to proinflammatory cytokines, chemokines, pattern recognition receptor signaling and antigen processing and presentation. Additionally, the flow cytometry data supports the notion that FUS can increase antigen presence or distribution within the tumor and contribute to dendritic cell maturation. Further work should aim to interrogate the role of microglia in this response, as well as distinguish which cell types exhibit enhanced antigen processing and presentation. Overall, the observed response to FUS + MB BTB/BBB opening in intracranial melanoma tumors is mild and transient; however, we contend that understanding this response will be useful for the rational design of FUS-mediated therapeutic delivery approaches.

5.6 Materials and Methods

5.6.1 Animals.

Wild-type male C57black6 mice were purchased from Charles River or NCI at 8-10 weeks of age. Male CD45.1 mice for adoptive transfer experiments were purchased at 8-10 weeks of age from NCI.

5.6.2 Tumor Implantation.

Mice were anesthetized with a mixture of ketamine (40 mg/kg; Zoetis, Kalamazoo, MI) and Dextomitor (0.2 mg/kg, Zoetis, Kalamazoo, MI) in 0.9% sterile saline. Mouse heads were depilated and buprenorphine was administered subcutaneously. Mice were then placed on a stereotaxic frame to position and secure the heads. The surgical site was prepared with alternating scrubs of alcohol and iodine and a midline scalp incision was made. A burr hole was drilled 2 mm to the right and 1 mm anterior to the intersection of the bregma and midline of the skull, to target the striatum as the injection site. B16F1, B16F1cOVA cells, or B16ZsGreenOVA (obtained from the Krummel lab) were loaded into a 10 ul Hamilton syringe mounted on the stereotaxic frame. The syringe was then placed in the burr hole and lowered to a depth of 4 mm below the skull and withdrawn 1 mm, for a final depth of 3 mm below the skull surface. A total volume of 2 ul of cell suspension (either 1e5, or 4e5 cells total) was injected over the course of 4 minutes. Almost all experiments utilized a cell implantation of 4e5 tumor cells, however, since B16F1 tumors were found to grow faster than B16F1cOVA tumors, 1e5 B16F1 cells were implanted for the endothelial cell adhesion molecule experiment. After one additional minute, the needle was slowly removed from the brain. Mice were sutured and moved to a heating pad for recovery. Anesthesia was reversed with Antisedan.

5.6.3 BTB/BBB Opening with MR Image-Guided FUS and Microbubbles.

Depending on experimental design and cell number implanted, FUS treatments were applied at either day 3 or day 6 tumor cell. Mice were anesthetized with a mixture of Ketamine (40 mg/kg; Zoetis, Kalamazoo, MI) and Dextomitor (0.2 mg/kg, Zoetis, Kalamazoo, MI) in 0.9% sterile saline and tail veins were cannulated to allow for multiple intravenous injections. The MR-guided FUS system (RK-100, FUS Instruments) sat directly on the patient table of a clinical 3T MRI scanner (Siemens Avanto). Mice were placed supine on the MR-guided FUS system with the skull sonically coupled to a 1.1 MHz spherically focused ultrasound transducer (with a 550 kHz hydrophone mounted in the center for passive cavitation detection) immersed in a degassed water bath. For the general treatment procedure, MultiHance gadolinium contrast agent (Bracco Diagnostics) was administered intravenously and a pre-FUS T1-weighted contrast-enhanced MR image of the entire brain was acquired using a custom-built 3-cm loop receive RF coil and three-dimensional spoiled gradient echo pulse sequence. Pulse-sequence parameters for all T1-weighted images were as follows: TR/TE = 11/5.33 ms, flip angle = 15°, readout bandwidth = 250 Hz/Px, FOV = 46×67×45 mm, resolution = 0.35 mm isotropic, total time per image = 3:05. Sonication pattern was chosen based on the tumor size at the time of treatment. Either a single target spot (day 3 treatment) or a grid of 4 spots (100,000 or 400,000 cells, day 6 treatment) were chosen from this pre-sonication MR image to cover the entire tumor and surrounding tissue. To open the BTB/BBB, albumin-shelled MBs (1×10^5/gram body weight; manufactured as previously described) were intravenously injected and FUS was applied to the targets using specified peak negative pressures (0.5 MPa measured in water). FUS was applied in 10 ms pulses with a 2 s pulsing interval (i.e. 0.5% duty cycle) for a total of 2 minutes. Animals were then re-injected with gadolinium contrast agent and post-sonication T1-weighted contrast-enhanced MR images were acquired to confirm BTB/BBB opening. Once the treatment was completed, mice were given Antisedan to reverse the anesthesia and allowed to recover on a heating pad.

5.6.4 RNA Sequencing.

For RNA sequencing, 400,000 B16F1cOVA cells were implanted into the brain as previously described, 3 days prior to FUS treatment. For FUS treatment, a single sonication spot was applied in the presence of circulating microbubbles at the tumor location. Tumor tissue was harvested 6 hours and 24 hours following FUS application for treated and sham mice. Immediately following euthanasia, sham and FUS-treated tumors were excised, placed in RNAlater (Qiagen) and stored at -80 °C. RNA extraction was performed using the RNeasy Mini Kit (Qiagen). mRNA was isolated using the NEBNext Poly(A) mRNA Magnetic Isolation Module (New England Biolabs, Ipswich, Massachusetts) followed by library preparation using the NEBNext Ultra II Directional RNA Library Prep Kit for Illumina (New England Biolabs). Sequencing was performed using a NextSeq 500 (Illumina, San Diego, California) at a target depth of 25 million 2 x 75 bp paired end reads per sample. Reads were quasi-mapped to the mouse genome (mm10 assembly, modified to include the cOVA transgene) and quantified at the transcript level using Salmon v0.11.2 followed by summary to the gene level using tximport v1.10.1(*148*, *149*). Differential gene expression was performed with DESeq2 v1.22.2(*150*). Gene set enrichment analysis was performed with the MSigDB canonical pathways gene sets using FGSEA v1.8.0 run with 100,000 permutations(*151*, *152*).

5.6.5 Flow Cytometry Analysis of Post-FUS Immune Cell Infiltration.

Tumors, meninges, superficial lymph nodes, deep cervical lymph nodes, spleen, and blood were harvested at day 5-8 after tumor injection. Tumors, lymph nodes, and spleen were homogenized and filtered through 70 µm mesh. Meninges were separated from the skull cap and filtered through 70 µm mesh. Spleens and blood were treated with RBC lysis (Sigma). Samples were stained for viability, treated with CD16/32 antibody to block Fc receptors, and then stained with dextramer (in T cell panels). Staining was done in FACS buffer (PBS, BSA,

sodium azide) with normal mouse serum. Next samples were stained with a variety of surface markers (see below) and then preserved using FACS lysis (BD). Samples were acquired on an Attune NxT flow cytometer and the data was analyzed using Flowjo and Prism software. Staining Panel: Aqua Live/dead, CD16/32, CD45, CD45.1, CD45.2, Thy1.1, , CD8, CD4, OVA dextramer, CD44, PD1, Tim3, TIGIT, CD27, CD25, CXCR3, PD1, CD69, CD11b, CD11c, MHCII, CD86, MHC SIINFEKL, F4/80, Ly6C, CD103.

5.6.6 Flow Cytometry Analysis of Endothelial Cell Adhesion Molecule Expression.

Tumors were harvested 24 hours following FUS + MB BTB/BBB opening. The tumors were minced and placed in digestion media containing 0.42U/ml Liberase TM (Roche). Samples were digested at 37 °C for 15 minutes and triturated every 5 minutes. Samples were homogenized (using glass homogenizers) and filtered through 70 µm filters. Subsequently, all samples were centrifuged at 1500 rpm for 15 minutes. The pellets were resuspended in CD45+ magnetic beads (Miltenyi Biotech) with Fc Block (1:1000) and incubated for 15 minutes at 4 °C. Samples were washed with AwesomeMacs Buffer and centrifuged at 1500 rpm for 5 minutes. Samples were separated with autoMACS Pro Separator with POSSEL AutoMACS protocol. The CD45 negative fraction was pelleted and stained with CD31 endothelial cell panel. Cells were Fc blocked and stained with fluorescent antibodies for CD31, CD45, E-sel, Icam, Vcam1 and Live/dead stain. Cells were fixed in 2% PFA and run on Attune flow cytometer. FlowJo software was used for analysis.

5.6.7 Activated T cell Adoptive Transfer

Activated cells were generated by culturing splenocytes in vitro with CD3/CD28/IL2 or after transferring Pmel IV into naïve mice and primed with CD40 (100 ug), polyI:C (75 ug), and gp100 (200 ug). CD8 T cells were then magnetically enriched and roughly 1 million cells were

transferred via tail vein injection 24 hours following FUS + MB BTB/BBB opening. Tumors and meninges were harvested 5 hours after cell transfer. CD45 antibody was given IV 3-5 minutes prior to harvest to label circulating cells.

5.7 Chapter 5 Figures

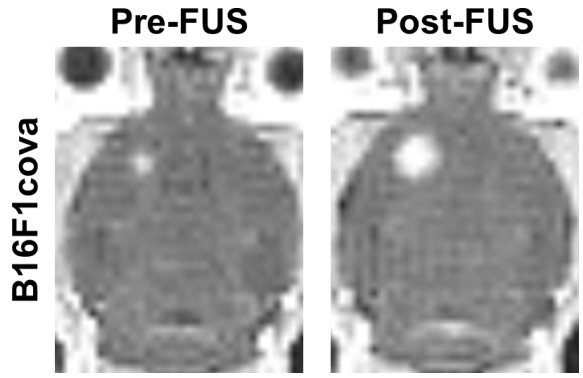

Figure 5.1. FUS + MB BTB/BBB Opening in Intracranial B16F1cOVA Tumors. Representative pre- and post-FUS T1-weighted contrast-enhanced MR images. The enhancing region in the pre-FUS image corresponds to the brain tumor, whereas the larger enhancing region in the post-FUS image corresponds to the region of FUS + MB BTB/BBB opening.

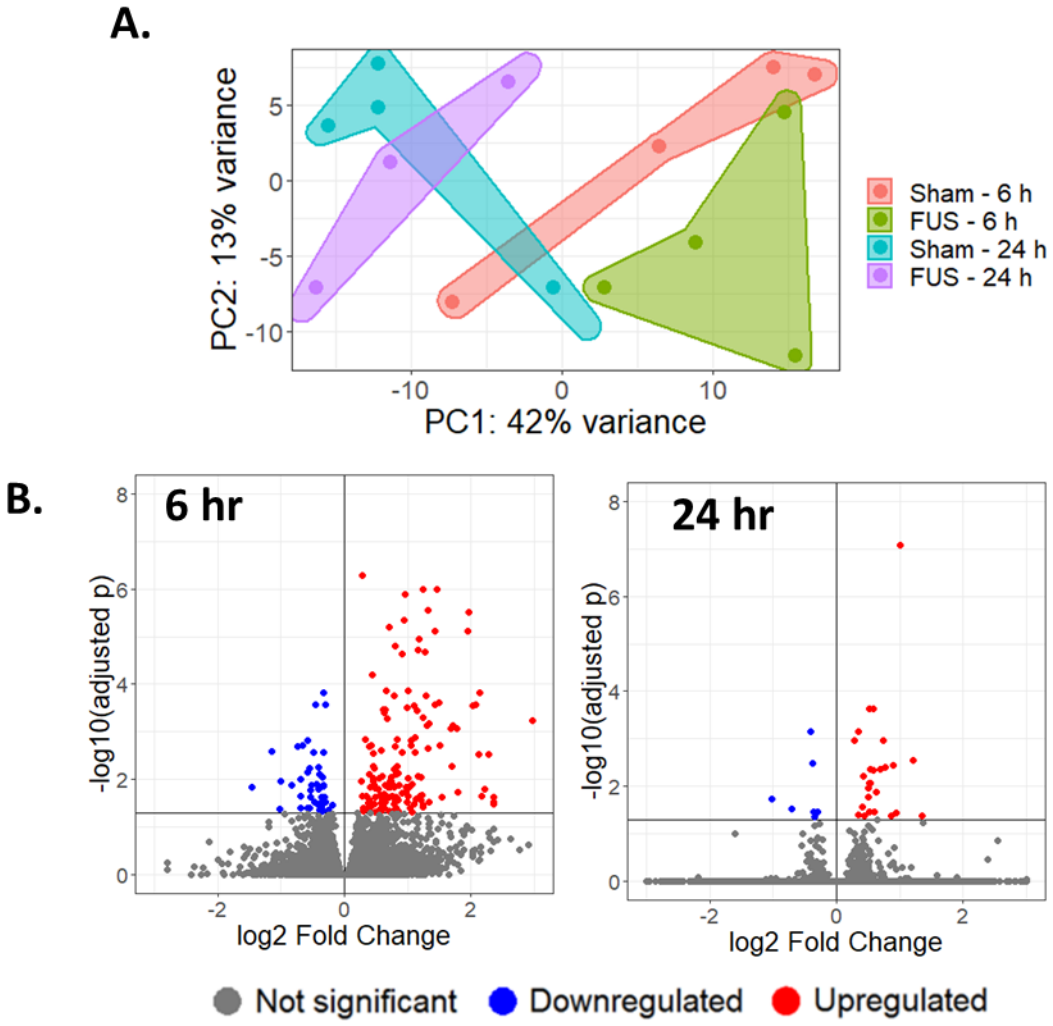

Figure 5.2. Differential Gene Expression in FUS-Treated Tumors Compared to Sham-Treated Tumors. A: Principal component analysis of gene expression in FUS-treated and sham B16F1cova tumor samples 6 hours and 24 hours post treatment. **B:** Volcano plots showing significantly upregulated and downregulated genes in FUS-treated tumors compared to sham at 6 and 24 hours post treatment.

		6 hrs		24 hrs	
A.	Transporters/BBB	Log2	Adj p	Log2	Adj p
	Slc15a3	**0.942513**	**4.44E-06**	0.103292	0.999895
	Slc10a6	**2.137894**	**1.49E-04**	0.309589	0.999895
	Slc11a1	**0.822037**	**0.007941**	0.529008	0.270422
	Slc5a6	**-0.57672**	**0.039549**	0.133011	0.999895
	Slc15a4	**-0.39534**	**0.04428**	0.051539	0.999895
	Slc45a3	**-0.6889**	**0.02245**	-0.15424	0.999895
	Emp1	**0.525128**	**0.01622**	0.15129	0.999895
B.	Pro-Inflammatory Cytokines	Log2	Adj. p	Log2	Adj. p
	TNF	**1.792403**	**0.018198**	0.408634	0.999895
	IL6	**2.361456**	**0.023245**	-0.93612	0.999895
	Il1a	0.545878	0.81108	0.608632	0.999895
	Il1b	1.225635	0.842485	-0.37423	0.999895
	Ifng	0.782711	NA	-1.97984	NA
C.	Immune Cell Recruitment/Differentiation	Log2	Adj p	Log2	Adj p
	Ccl2	**3.14785**	**6.12E-09**	-0.12281	0.999895
	Ccl12	**1.949103**	**7.66E-06**	0.115067	0.999895
	Cxcl16	**0.950491**	**1.27E-06**	0.585241	0.999895
	Cxcl10	**2.167761**	**0.022088**	-0.04575	0.999895
	Ccl7	**2.112608**	**0.002939**	-0.3557	0.999895
	Cxcl1	**2.972499**	**5.95E-04**	-0.81335	0.999895
	Ccr2	0.725025	0.490373	**0.886435**	**0.003636**
	CD86	0.57483	0.206593	0.373832	0.819596
	Selp	1.300102	0.280927	-0.20929	0.999895
	Sele	0.906384	0.781308	-0.40213	0.999895
	Icam1	**0.767556**	**0.047331**	0.152733	0.999895
	Vcam1	0.038301	0.998775	0.318232	0.999895

Figure 5.3. Differential Expression of Selected mRNA Transcripts in FUS-Treated Versus Sham Tumors. A,B,C,D,E: Log2 fold change and adjusted P values of FUS-treated vs. sham tumors at 6 hours and 24 hours post treatment. Data is displayed for selected mRNA transcripts related to (A) Transporters/BBB (B) Proinflammatory cytokines (C) Immune cell recruitment/differentiation

D.

MHC Class I Antigen Processing and Presentation	6 Hours		24 Hours	
	Log2	Adj p	Log2	Adj p
H2-K1	**0.64163**	**1.49E-13**	0.204644	0.999895
H2-Q4	**0.915322**	**3.56E-12**	0.289701	0.999895
H2-Q7	**1.341052**	**6.77E-04**	0.299279	0.999895
H2-D1	**0.459109**	**0.009491**	0.222217	0.999895
H2-Q6	**1.234532**	**1.04E-06**	0.194679	0.999895
TAP1	**0.794733**	**1.56E-05**	0.414386	0.523313
TAP2	**0.396064**	**0.030531**	0.034373	0.999895
Psmb8	**0.645394**	**3.35E-04**	**0.60201**	**0.034829**
Psmb9	0.53227	0.096283	0.513256	0.999895

E.

Pattern Recognition Receptor Signaling	Log2	Adj p	Log2	Adj p
Clec7a	**1.494235**	**2.45E-04**	0.379404	0.999895
CD14	**1.22101**	**0.021522**	-0.15285	0.999895
Pik3ap1	**0.591057**	**0.044624**	0.363744	0.999895
CD36	0.555943	0.058241	0.482748	0.422907
Tlr13	0.365067	0.073072	0.412456	0.51637
Nlrc5	0.594911	0.302429	0.497443	0.068501
CD180	0.028602	0.998775	0.424431	0.136437
Marco	0.417119	0.998775	2.391994	0.357045

Figure 5.3 (Cont.) Differential Expression of Selected mRNA Transcripts in FUS-Treated Versus Sham Tumors. D,E: Log2 fold change and adjusted P values of FUS-treated vs. sham tumors at 6 hours and 24 hours post treatment. Data is displayed for selected mRNA transcripts related to (D) MHC class I antigen presentation and processing and (E) Pattern recognition receptor signaling.

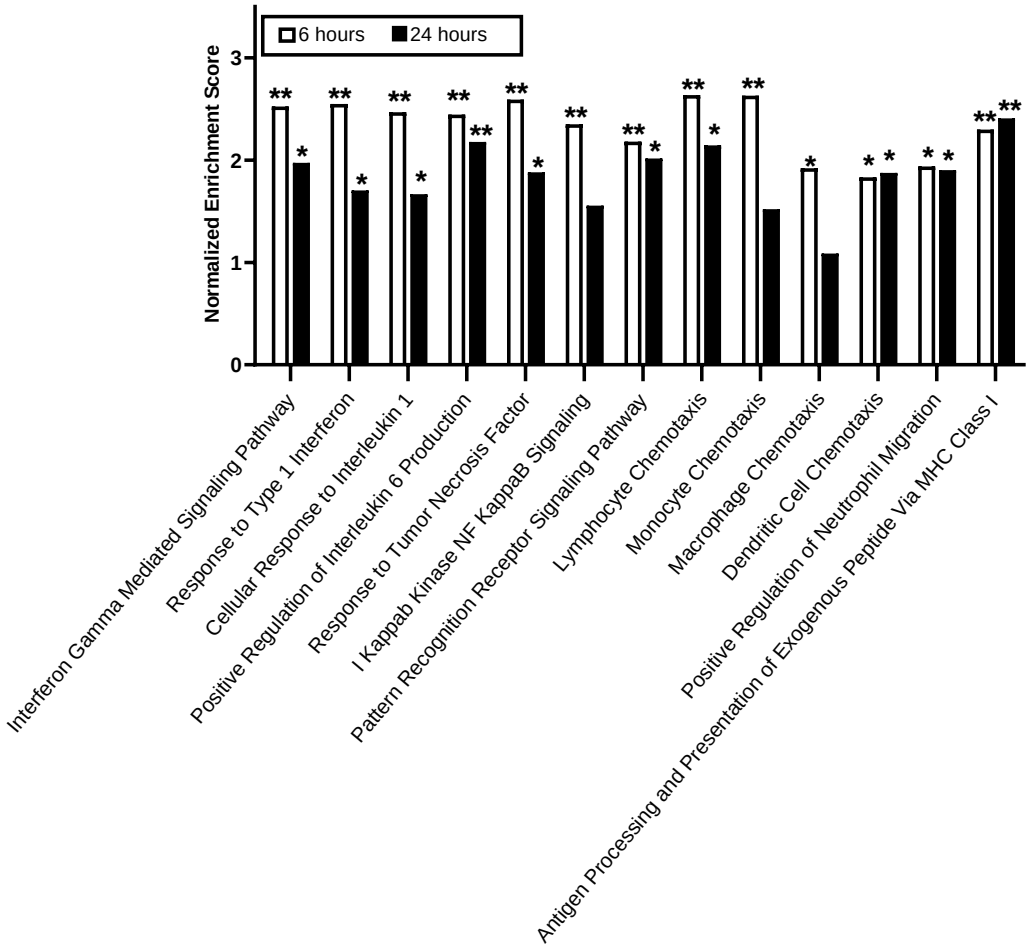

Figure 5.4. Significantly Enriched Pathway in FUS-Treated Tumors by Gene Set Enrichment Analysis Normalized enrichment scores for selected pathways 6 and 24 hours post-FUS BTB opening. **adj. p<0.001, *adj p<0.05.

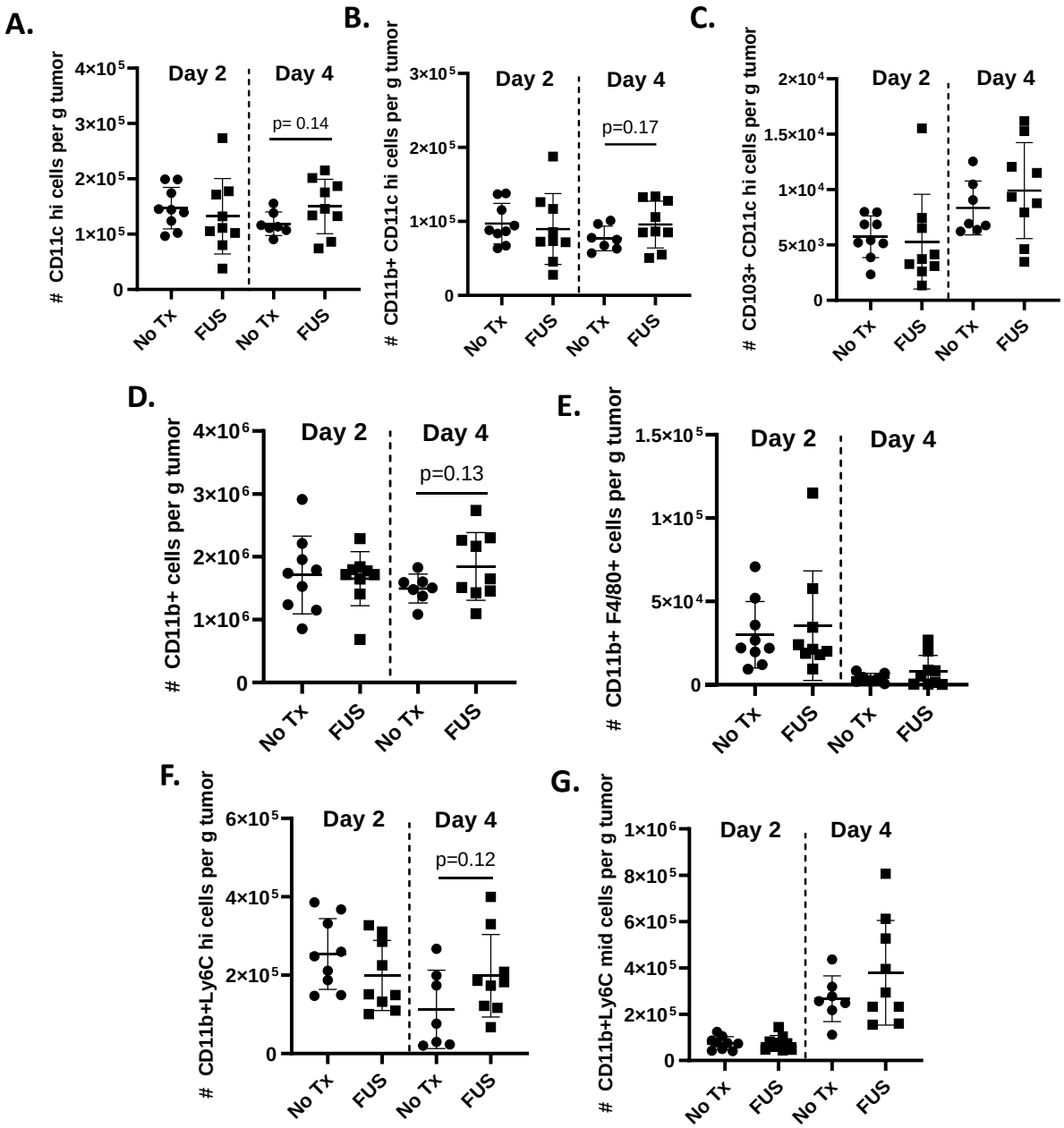

Figure 5.5. Innate Immune Cell Populations in FUS-Treated and Control Tumors. A,B,C: Number of (A) dendritic cells and (B,C) dendritic cell subsets per gram of tumor two and four days post treatment assessed by (A) CD11c hi (B) CD11c hi CD11b+ (C) CD11c hi CD103+. **D,E,F,G:** Number of (D) myeloid cells and (E,F,G) myeloid cell subsets per gram of tumor two and four days post treatment assessed by (D) CD11b+ (E) CD11b+ F4/80+ (F) CD11b+ Ly6C hi (G) CD11b+ Ly6C mid. Significance assessed by unpaired T tests between untreated and FUS BTB treated tumors at each time point.

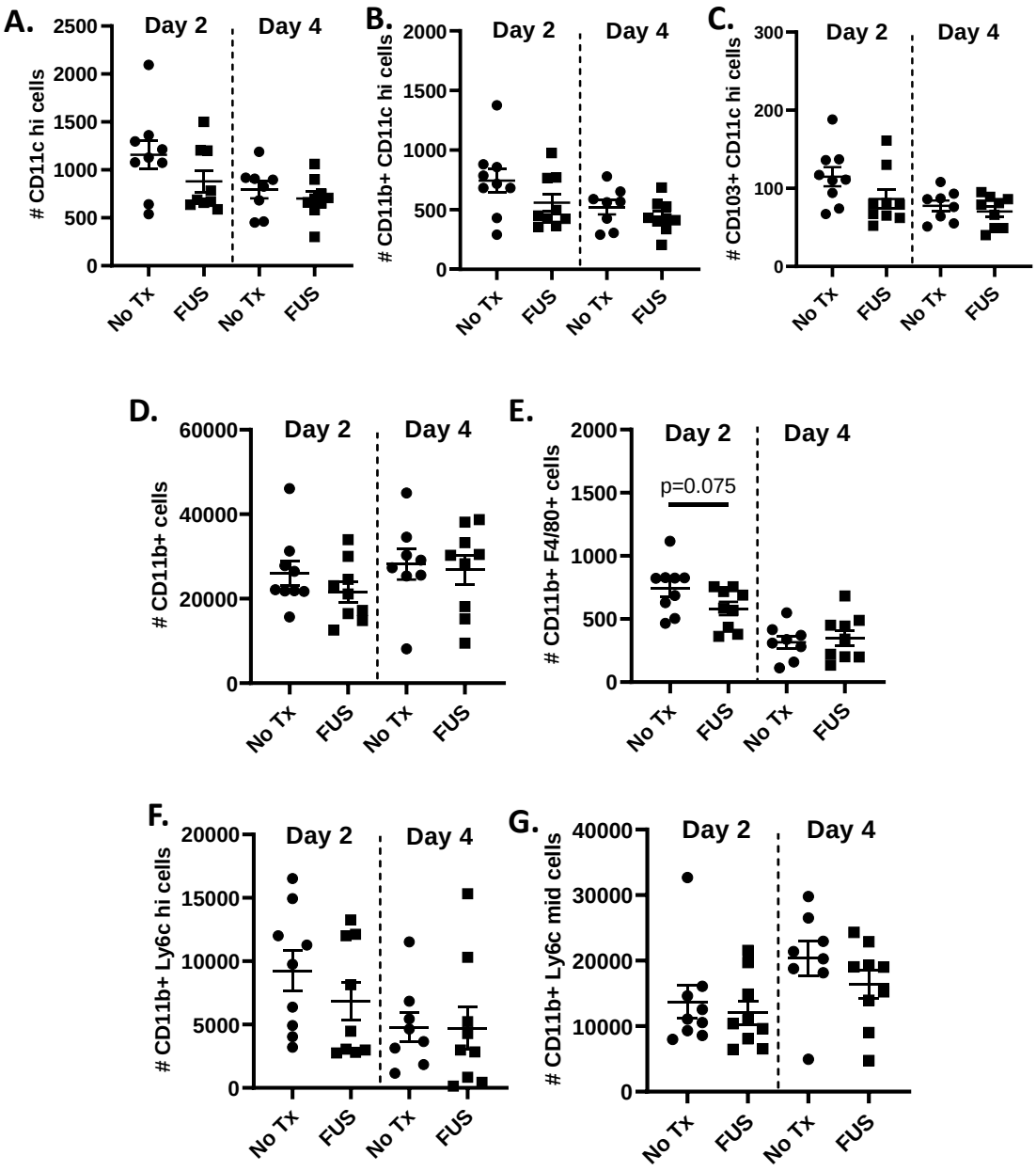

Figure 5.6. Innate Immune Cell Populations in the Meninges of FUS-Treated and Control Animals. A,B,C: Number of (A) dendritic cells and (B,C) dendritic cell subsets in the meninges two and four days post treatment assessed by (A) CD11c hi (B) CD11c hi CD11b+ (C) CD11c hi CD103+. **D,E,F,G:** Number of (D) myeloid cells and (E,F,G) myeloid cell subsets in the meninges two and four days post treatment assessed by (D) CD11b+ (E) CD11b+ F4/80+ (F) CD11b+ Ly6C hi (G) CD11b+ Ly6C mid. Significance assessed by unpaired T tests between untreated and FUS BTB treated tumors at each time point.

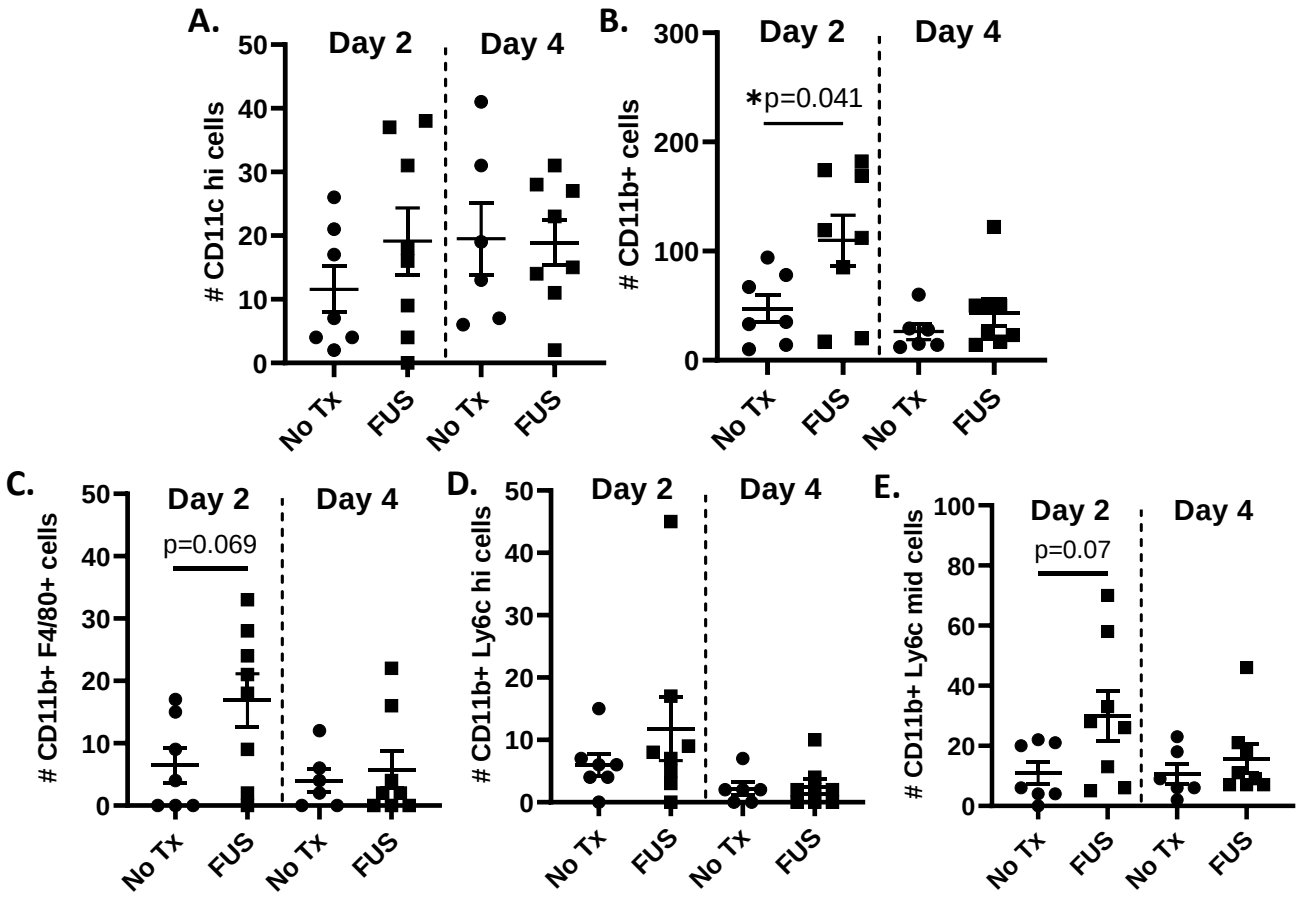

Figure 5.7. Innate Immune Cell Populations in the Deep Cervical Lymph Nodes of FUS-Treated and Control Animals. A: Number of dendritic cells in the deep cervical lymph nodes two and four days post treatment assessed by CD11c hi. **B,C,D,E:** Number of (B) myeloid cells and (C,D,E) myeloid cell subsets in the deep cervical lymph nodes two and four days post treatment assessed by (B) CD11b+ (C) CD11b+ F4/80+ (D) CD11b+ Ly6C hi (E) CD11b+ Ly6C mid. Significance assessed by unpaired T tests between untreated and FUS BTB treated tumors at each time point.

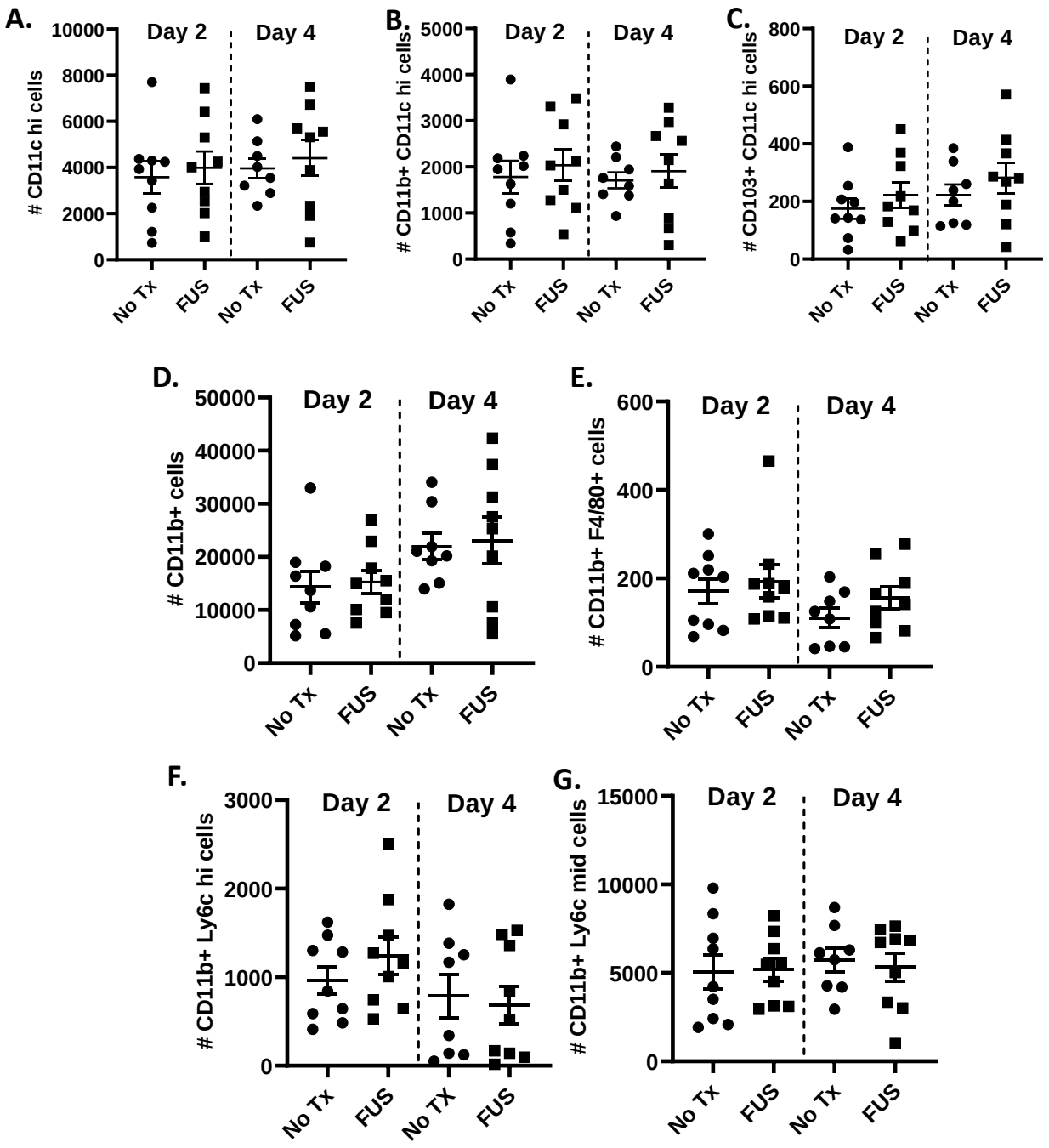

Figure 5.8. Innate Immune Cell Populations in the Superficial Cervical Lymph Nodes of FUS-Treated and Control Animals. A,B,C: Number of (A) dendritic cells and (B,C) dendritic cell subsets in the Superficial Cervical Lymph Nodes two and four days post treatment assessed by (A) CD11c hi (B) CD11c hi CD11b+ (C) CD11c hi CD103+. **D,E,F,G:** Number of (D) myeloid cells and (E,F,G) myeloid cell subsets in the Superficial Cervical Lymph Nodes two and four days post treatment assessed by (D) CD11b+ (E) CD11b+ F4/80+ (F) CD11b+ Ly6C hi (G) CD11b+ Ly6C mid. Significance assessed by unpaired T tests between untreated and FUS BTB treated tumors at each time point.

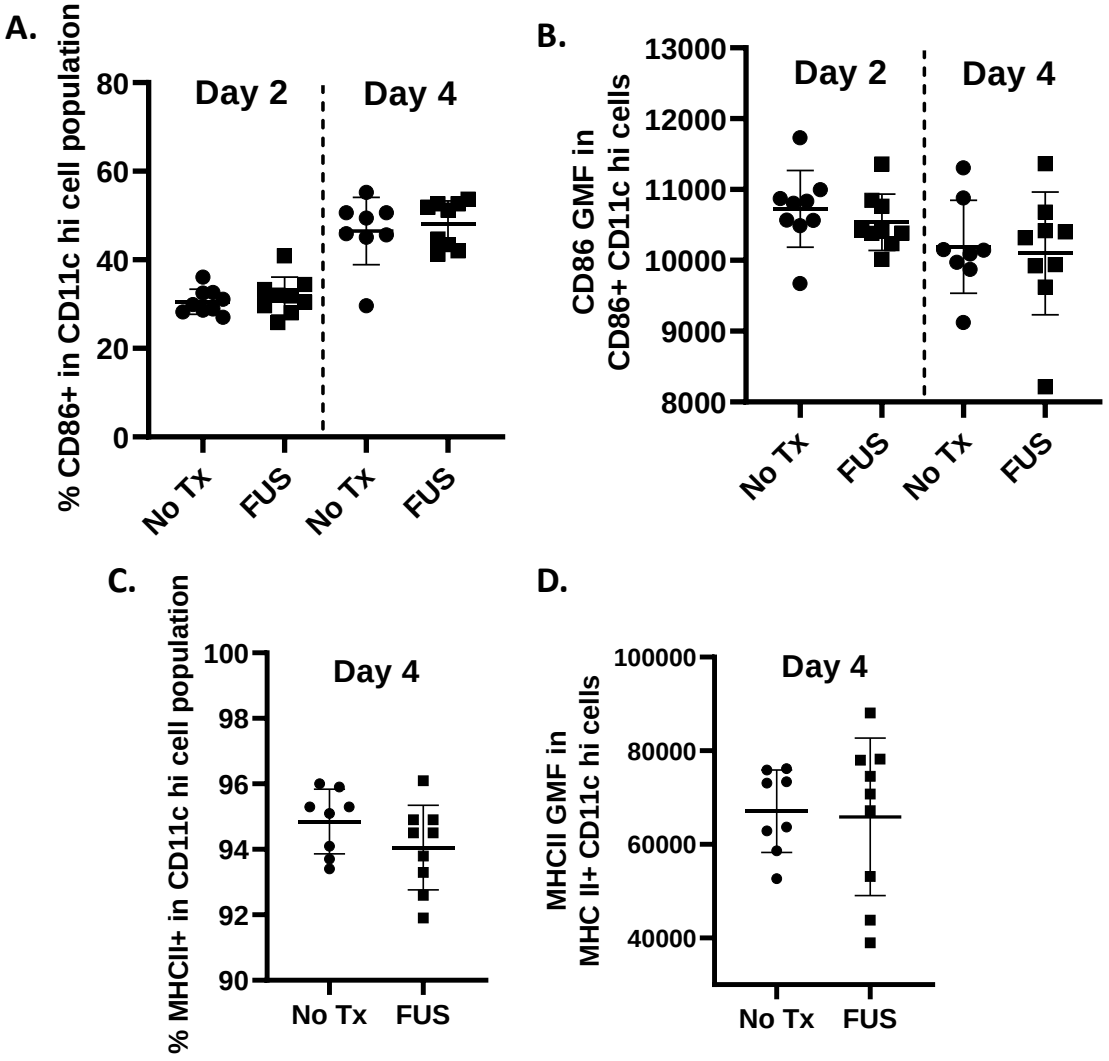

Figure 5.9. Expression of DC activation markers in FUS-Treated and Control Tumors. A,C: Percentage of dendritic cells expressing (A) CD86 or (C) MHCII in FUS-treated and control tumor 4 days post treatment. **B,D:** Geometric mean fluorescence of (B) CD86 in CD86 positive DCs or (D) MHCII in MHCII positive DCs from FUS-treated and control tumors 4 days after treatment. Significance assessed by unpaired T tests between untreated and FUS BTB treated tumors at each time point.

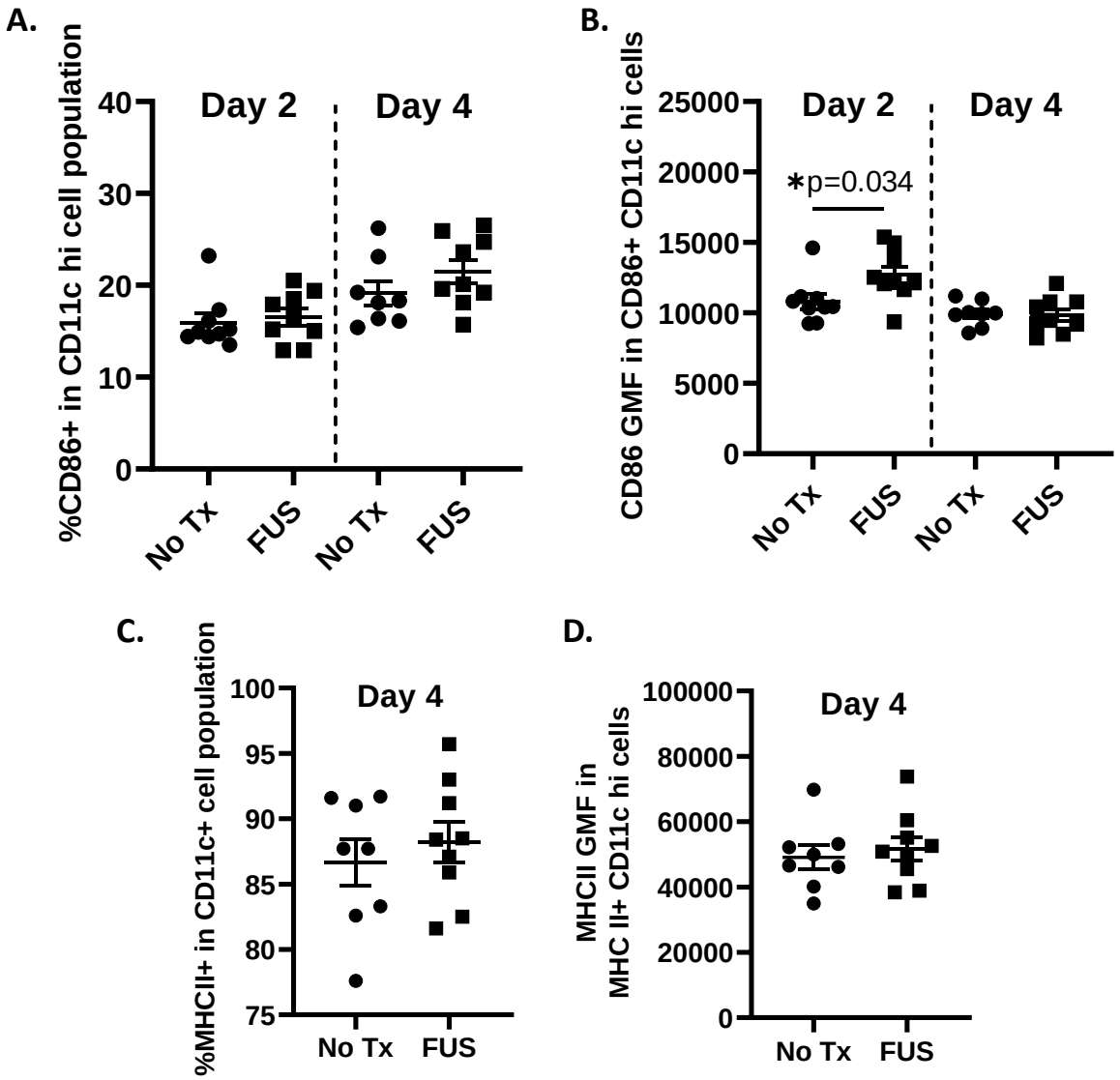

Figure 5.10. Expression of DC activation markers in the Meninges of FUS-Treated and Control Animals. A,C: Percentage of dendritic cells expressing (A) CD86 or (C) MHCII in the meninges of FUS-treated and control animals 4 days post treatment. **B,D:** Geometric mean fluorescence of (B) CD86 in CD86 positive DCs or (D) MHCII in MHCII positive DCs in the meninges of FUS-treated and control animals 4 days after treatment. Significance assessed by unpaired T tests between untreated and FUS BTB treated tumors at each time point.

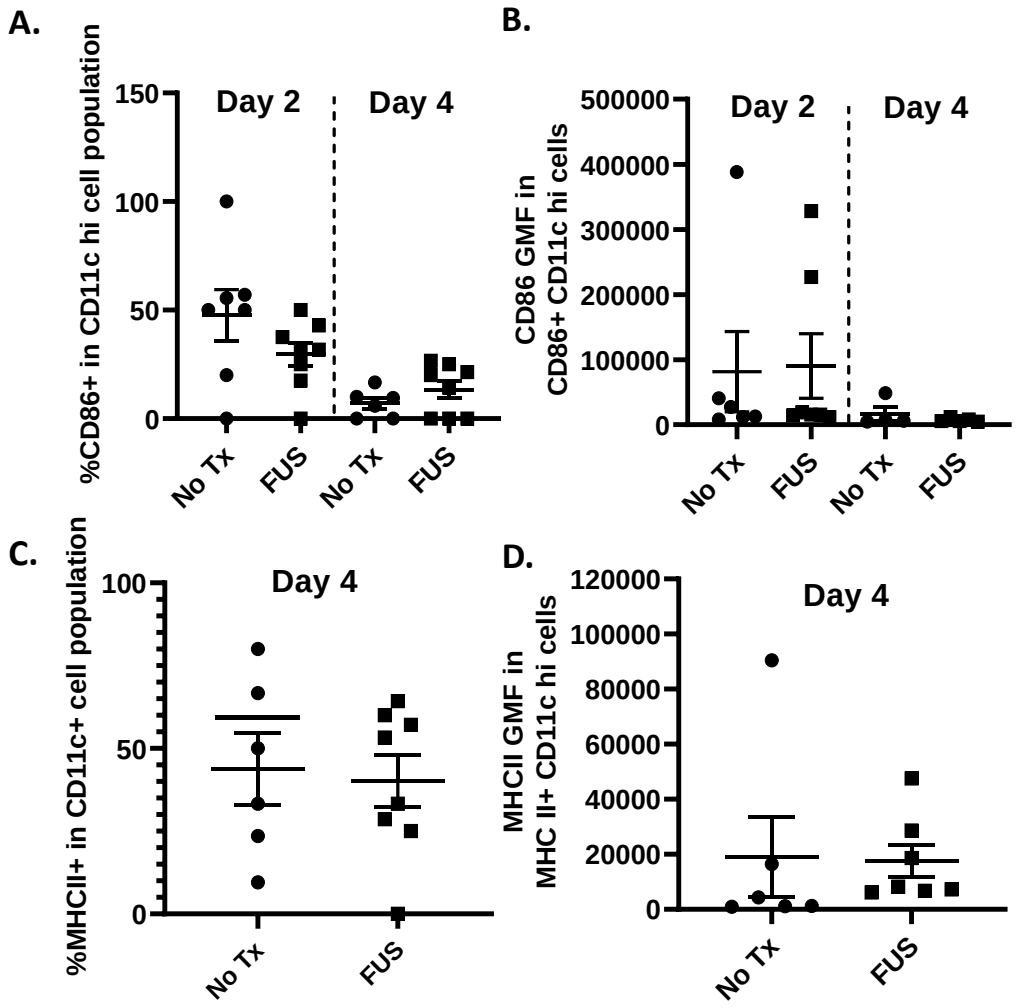

Figure 5.11. Expression of Specific Activation Markers on Dendritic Cells in the Deep Cervical Lymph Nodes of FUS-Treated and Control Animals. A,C: Percentage of dendritic cells expressing (A) CD86 or (C) MHCII in the deep cervical lymph nodes of FUS-treated and control animals 2 and 4 days post treatment. **B,D:** Geometric mean fluorescence of (B) CD86 in CD86 positive DCs or (D) MHCII in MHCII positive DCs in the deep cervical lymph nodes of FUS-treated and control animals 4 days after treatment. Significance assessed by unpaired T tests between untreated and FUS BTB treated tumors at each time point.

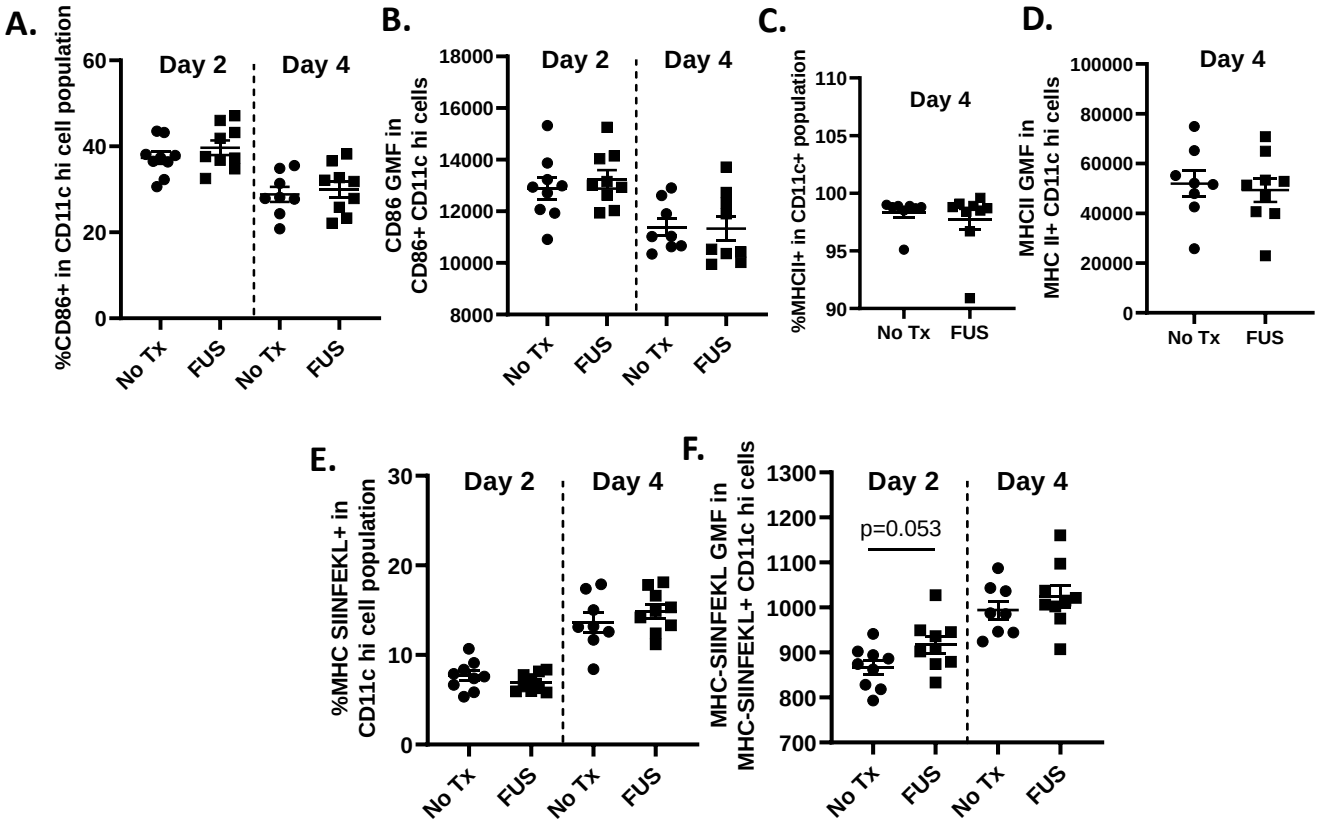

Figure 5.12. Expression of Specific Activation and Antigen Presentation Markers on Dendritic Cells in the Superficial Cervical Lymph Nodes of FUS-Treated and Control Animals. A,C,E: Percentage of dendritic cells expressing (A) CD86 (C) MHCII or (E) MHC-SIINFEKL in the superficial cervical lymph nodes of FUS-treated and control animals 2 and 4 days post treatment. **B,D,F:** Geometric mean fluorescence of (B) CD86 in CD86 positive DCs (D) MHCII in MHCII positive DCs or (F) MHC-SIINFEKL in MHC-SIINFEKL positive DCs in the superficial cervical lymph nodes of FUS-treated and control animals 2 and 4 days after treatment. Significance assessed by unpaired T tests between untreated and FUS BTB treated tumors at each time point.

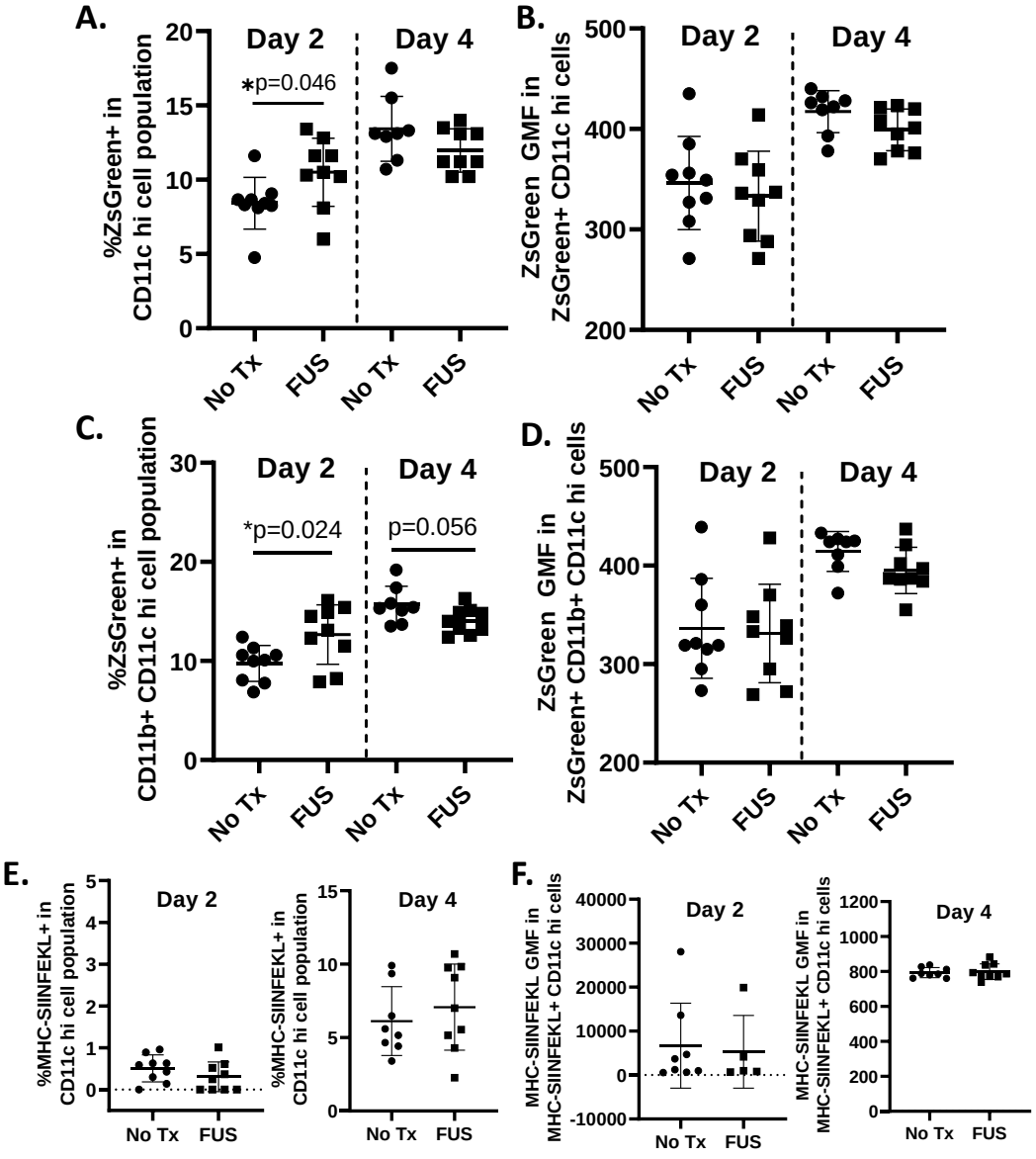

Figure 5.13. Antigen Uptake and Presentation in DCs of FUS-Treated and Control Tumors. A,C,E: Percentage of (A,C) ZsGreen positive cells in the (A) dendritic cell and (C) CD11b+ dendritic cell populations or (E) MHC-SIINFEKL positive dendritic cells in FUS-treated and control tumors 2 or 4 days after treatment. **B,D,F:** Geometric mean fluorescence of (B,D) ZsGreen in the ZsGreen positive (B) dendritic cell and (D) CD11b+ dendritic cell populations or (F) MHC-SIINFEKL in the MHC-SIINFEKL positive dendritic cell population of FUS-treated and control tumors 2 or 4 days after treatment. Significance assessed by unpaired T tests between untreated and FUS BTB treated tumors at each time point.

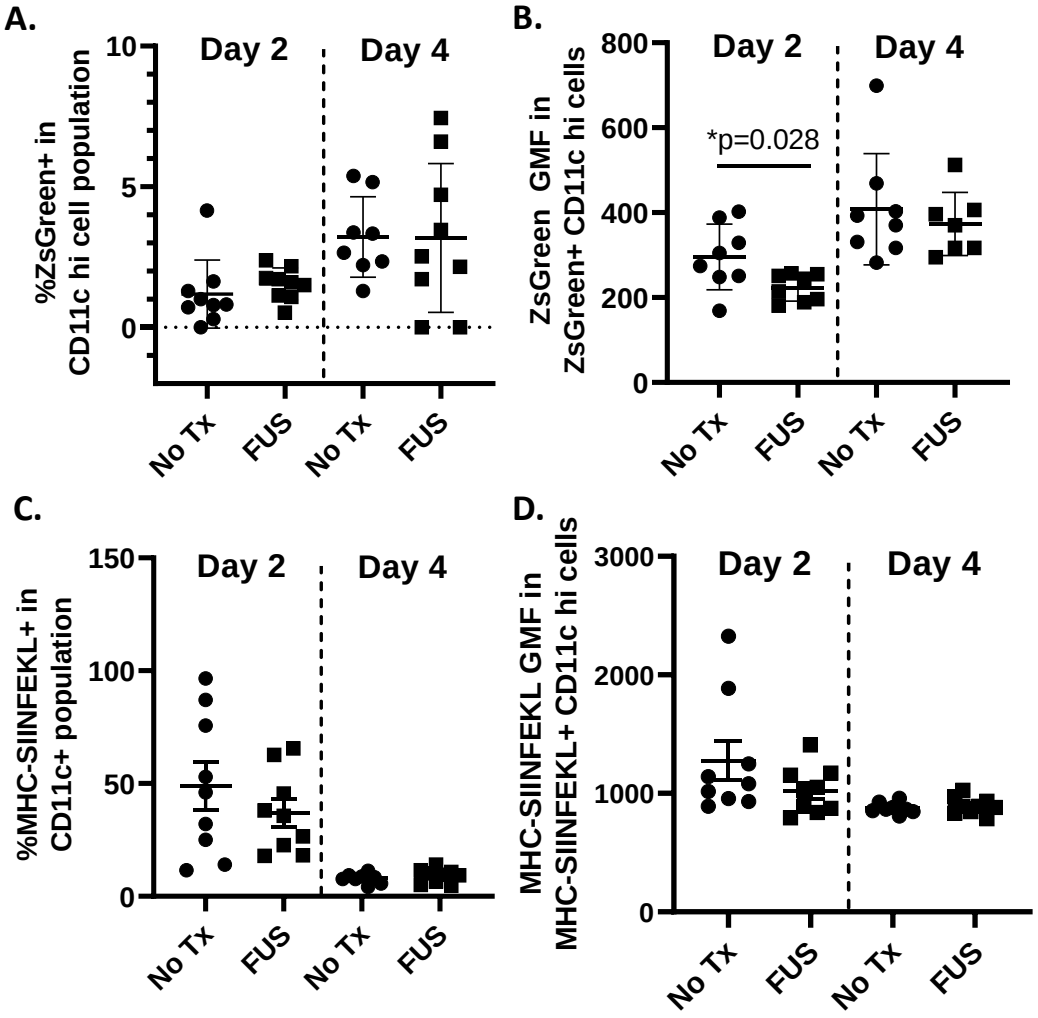

Figure 5.14. Antigen Uptake and Presentation in DCs in Meninges of FUS-Treated and Control Animals. A,C: Percentage of (A) ZsGreen positive or (C) MHC-SIINFEKL positive dendritic cells in the meninges of FUS-treated and control animals 2 or 4 days after treatment. **B,D,:** Geometric mean fluorescence of (B) ZsGreen in the ZsGreen positive or (D) MHC-SIINFEKL in the MHC-SIINFEKL positive dendritic cell population in the meninges of FUS-treated and control animals 2 or 4 days after treatment. Significance assessed by unpaired T tests between untreated and FUS BTB treated tumors at each time point.

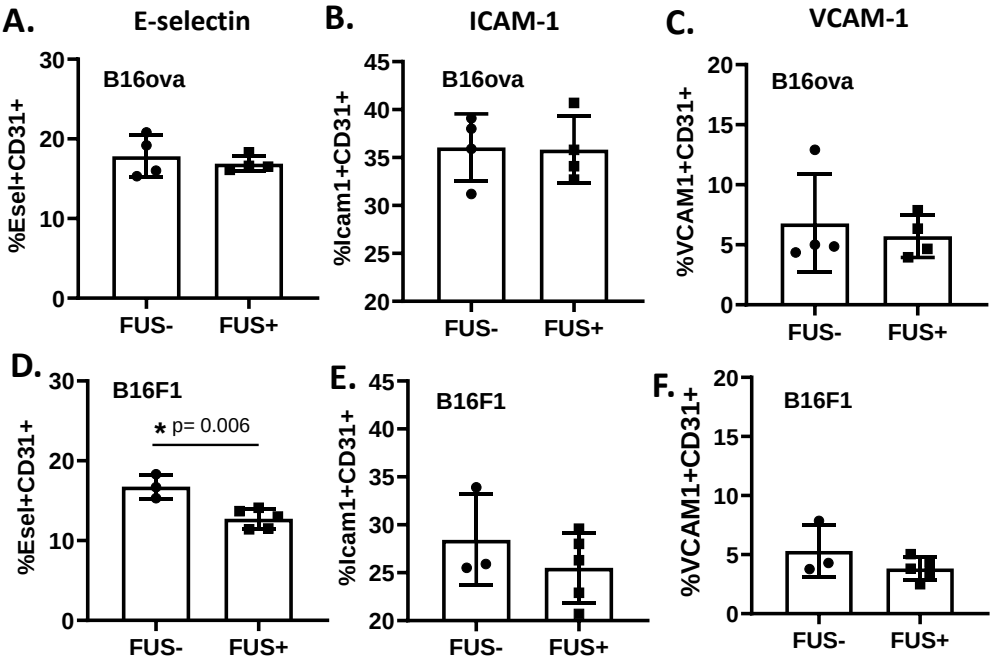

Figure 5.15. Endothelial Cell Adhesion Molecule Expression on the Vasculature of FUS-Treated and Untreated Tumors. A,B,C: Percentage of endothelial cells expressing (A) E-selectin (B) ICAM-1 or (C) VCAM-1 from FUS-treated and control B16ova tumors. **D,E,F:** Percentage of endothelial cells expressing (D) E-selectin (E) ICAM-1 or (F) VCAM-1 from FUS-treated and control B16F1 tumors. . Significance assessed by unpaired T tests

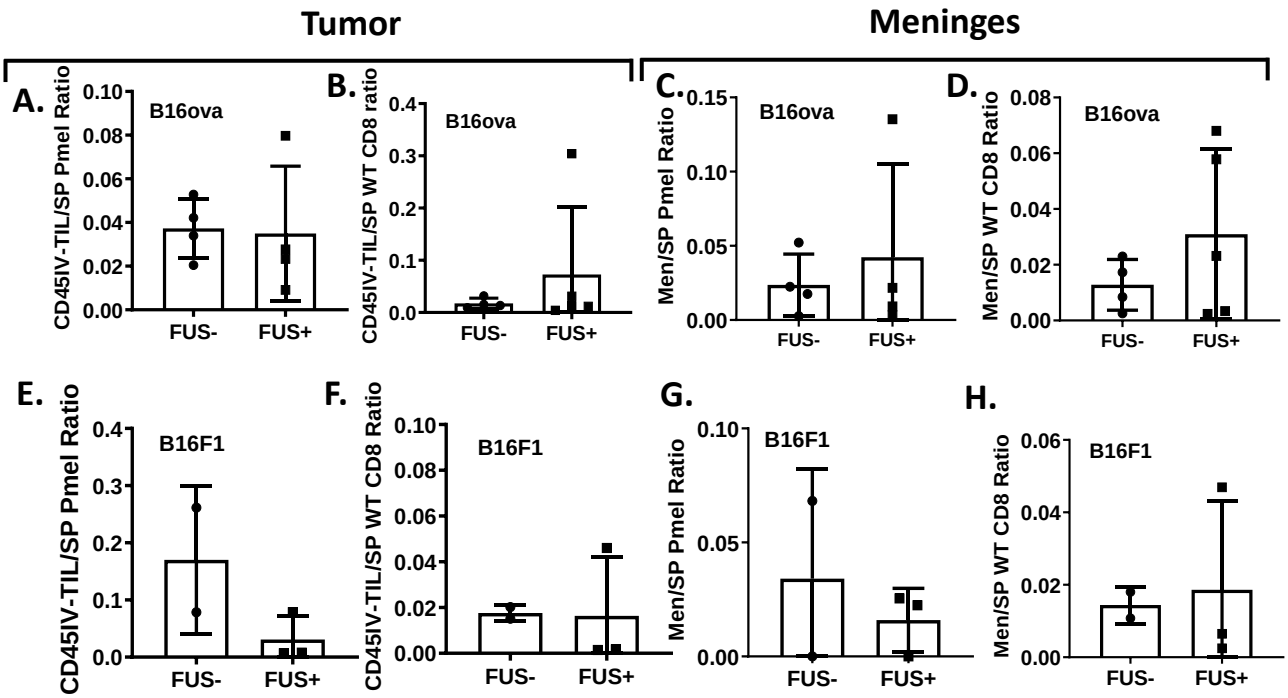

Figure 5.16. Adoptively Transferred Activated T Cell Populations in the Tumor and Meninges of FUS-Treated and Control Animals. A,C,E,G: Ratio of transferred Pmel T cells in the (A,E) tumor or (C,G) meninges to the number in the spleen of FUS-treated or control animals bearing intracranial (A,C) B16ova or (E,G) B16F1 tumors. **B,D,F,H:** Ratio of transferred non-specific T cells in the (B,F) tumor or (D,H) meninges to the number in the spleen of FUS-treated or control animals bearing intracranial (B,D) B16ova or (F,H) B16F1 tumors.

Chapter 6: Future Directions

6.1 The Role of BPN Distribution Versus Cell Uptake in Enhanced FUS + BPN-Mediated Tumor Transfection

In Chapter 3 of this dissertation, we develop a method for transfection of both primary and secondary brain tumors using focused ultrasound + MB BTB/BBB opening and non-viral brain-penetrating nanoparticle gene vectors. Additionally, we identified FUS-induced increases in interstitial fluid flow a likely key contributor to FUS-mediated transfection. We showed that application of FUS + MB BTB/BBB opening prior to direct injection of BPNs results in a two-fold increase in volume of transfection compared to the injection alone. This supports the notion that FUS-induced increases in convective transport yields enhanced particle distribution, and ultimately a greater number of cells taking up and expressing the reporter gene.

However, an alternative explanation for this result is that FUS is enhancing the ability of cells within the tumor to take up the nanoparticles, which can also produce a larger overall number of transfected cells. In order to assess the relative effects of uptake versus distribution of BPNs, we could perform a direct injection experiment similar to what was done in chapter 3, and we could once again utilize BPNs made with fluorescently labeled DNA. This would allow us to assess the effects of FUS + MB BTB/BBB opening on distribution of the DNA-loaded nanoparticles rather than transfection. One important consideration for this experiment would be the timing of tissue harvest after the injection. If there is enough time for clearance of the nanoparticles, it will once again be difficult to distinguish between uptake and distribution, since only fluorescently labeled-DNA that has been taken up by cells will remain in the system. This experiment could also be performed with agents that are not taken up by cells, and therefore expected to remain in the tissue interstitial space. To this end, data from the literature has shown that FUS + MB BBB opening prior to injection of gadolinium yields and increased volume of contrast enhancement(*90*). This supports the hypothesis that FUS enhances movement of agents in the tissue and can thus enhance BPN distribution, however there is a vast difference

in size between these two agents making it difficult to extend this result to our nanoparticle-based system. Similar experiments could be performed with liposomal or nanoparticle-based MR contrast agents that are more comparable in size our BPNs. Furthermore, such agents could be used in conjunction with the MRI based transport analysis to assess how FUS + MB BTB/BBB opening modulates transport of larger agents within brain tumor tissue.

6.2 Further Evaluation of the Role of Interstitial Fluid Flow on FUS + BPN-Mediated Tumor Transfection

The finding in chapter 3 that FUS + MB BTB/BBB opening results in a two-fold increase in interstitial fluid velocity opens up many questions regarding the role of interstitial flow in BPN delivery and transfection. Here, we found similar increases in interstitial fluid velocity magnitude at both tested FUS pressures, 0.45 and 0.55 MPa. This result brings up the question of whether this increase in flow velocity magnitude is independent of the applied FUS pressure. Future studies should aim to answer this question by similarly measuring pre- and post-FUS flow velocity magnitude at various FUS pressures below 0.45 MPa and above 0.55 MPa and assessing transfection. It is possible that even at very low pressures below the threshold for BBB opening in normal brain tissue, application of FUS in the presence of circulating microbubbles may still enhance transfection over the EPR effect by altering interstitial transport properties of BPNs that accumulate in the tissue. It is also possible that at higher pressures increased magnitude of bubble oscillation can differentially drive fluid into the tissue and change flow velocity. In these studies, passive cavitation detection can be used to determine whether bubble cavitation corresponds to changes in interstitial transport. Determining the pressure dependence of these changes in interstitial transport may be crucial in optimizing delivery parameters.

Here, we have shown that 6 hours after delivery of cy5 fluorescently labelled DNA-BPNs with FUS + MB, we achieve increased *ex vivo* fluorescence signal due to enhanced nanoparticle delivery. While we do provide immunofluorescence images of tumor tissue sections showing regions of intense cy5 signal outside of blood vessels, future studies could focus on quantifying effects of FUS on penetration of BPNs away from vessels. This can be done by similarly using cy5 labeled DNA-BPNs and studying acute time points following delivery. Intravenous injection fluorescent lectin prior to euthanasia of the animals would allow for labelling of functionally perfused vessel, and evaluation of cy5-BPN distance from vessels via IF. Furthermore, we could see whether distribution of the fluorescence signal throughout tissue sections correlates spatially to flow velocity magnitude maps obtained from the transport analysis.

6.3 Therapeutic Strategies for FUS + BPN Brain Tumor Transfection

In chapter 3 of this dissertation, we prove that FUS + MB BTB/BBB facilitates BPN-mediated transfection of intracranial tumors, as well as provide evidence that supports a possible mechanism beyond vascular permeabilization. Future studies should focus on determining the cell types that are transfected, as well as estimating the percentage of cells within the tumor that are transfected. These will be important factors in determining the most promising therapeutic strategies for this technique. Going forward, one important thing to consider is that since the plasmid DNA will not be stably transfected into the cells, therapeutic genes specifically aimed at the tumor cell population will likely require repeated treatments. Furthermore, expanding this approach to into highly invasive tumor models or resection models will be important, as these more accurately reflect the application of this technology in a clinical setting.

It is possible that the best application of this strategy will be for a combination approach, utilizing both immunotherapeutic gene therapy and direct tumor cell killing to generate an antitumor response. Such an approach has been previously describe and developed using adenoviral vectors for expression of both fms-like tyrosine kinase 3 ligand (Flt3L) and Herpes Simplex Virus Type 1-Thymidine Kinase (TK) with ganciclovir (GCV) prodrug administration(*153*). Flt3L is a cytokine that differentiates dendritic cell precursors and also acts as a cytokine for DC recruitment. Interestingly, Flt3L has been shown to preferentially act on the CD103+ conventional DC compartment, which as previously described have been implicated in cross-presentation of tumor antigens and stimulation of antitumor immunity(*130*). Expression of Flt3l aims to increase the abundance of intratumoral DCs, while TK suicide gene therapy with GCV administration induces release of tumor antigens by direct tumor cell killing. This approach has been shown to induce antitumor immune responses to intracranial tumors and provide long-term survival in intracranial tumor bearing mice and rats(*154*). Additionally, induction of immunological memory has been demonstrated in these animals by elimination of untreated tumor foci and protection against brain tumor rechallenge(*155*, *156*). This approach is being tested in a phase I clinical trial (NCT01811992) for GB patients, in which adenoviral vectors are administered into the tumor resection cavity. Focused ultrasound provides the opportunity to achieve a similar treatment strategy in a completely noninvasive manner in preclinical brain tumor models. The approach developed in this thesis could be used to deliver the Flt3L gene to intracranial tumors and surrounding normal brain tissue to stimulate infiltration and differentiation of DCs. Subsequently, a second FUS treatment for thermal or mechanical ablation within the tumor bulk could be utilized to kill tumor cells and generate tumor antigens for immune priming. Several aspects of this approach would need to be optimized, however the versatility of FUS as a treatment modality provides opportunities to investigate a wide variety of combined immunotherapeutic and direct cell killing strategies.

6.4 Assessment of FUS Preconditioning Mechanism and Development of Successful Application in Tumors

In Chapter 4 of this dissertation, we tested whether FUS preconditioning prior to FUS + MB BTB/BBB disruption for BPN delivery can enhance intracranial tumor transfection. Though we did not achieve enhanced tumor transfection with either of the tested preconditioning parameters, we have previously shown that a similar approach was effective in the rat striatum, increasing transfection up to 5-fold(*95*). To begin to understand why this treatment was unsuccessful in tumors, a more extensive characterization of the mechanism of FUS preconditioning in normal brain tissue will be necessary. Future work should aim to fully characterize the tissue bioeffects and subsequent alteration of the tissue structure that results in efficacy of this approach in normal brain tissue. These studies should use techniques such as acoustic radiation force imaging (ARFI) to measure the tissue displacement achieved during the preconditioning procedure. While we have previously implicated activation of mechanosensitive TRPA ion channels in enhanced BPN spreading, the molecular responses occurring in the tissue should be further characterized. Moreover, tissue sections should be analyzed to assess structural changes in the tissue such as ECM content and distribution.

Once the tissue bioeffects of successful FUS preconditioning protocols in normal tissues is established, we can design FUS parameters to achieve similar tissue heating and mechanical perturbation in tumor tissue and assess the response. It is possible that even if we achieve the same thermal and mechanical perturbation in tumor tissue, tumor responses will vary compared to normal tissue. Factors such as ECM abundance and structure, as well as expression level or even localization of certain mechanosensitive ion channels may be altered in tumor tissue and can contribute to differential or defective responses. A better mechanistic understanding of preconditioning in normal tissue will allow us to dissect these differences and devise approaches to support this response in tumor tissue. Ultimately, FUS preconditioning is still a

desirable method to enhance transfection of brain tumor tissue, however, further work is needed to devise an effective protocol.

6.5 Characterization of Response to FUS + MB BTB/BBB Opening in Intracranial Melanoma

In chapter 5 we describe a mild, transient pro-inflammatory response to FUS + MB BTB/BBB in intracranial melanoma tumors. In these studies, gene set enrichment analysis revealed increases in signaling pathways related to type I and type 2 interferons, IL1a, IL1b, as well as several additional pro-inflammatory interleukins. The mRNA for these particular molecules, however, were not significantly increased at either of the tested time points. This could suggest that our timing is inappropriate to detect changes in these transcripts. Future studies should include additional time points to obtain better temporal resolution of the proinflammatory response. Additionally, assays for measuring protein levels in the CSF and/or interstitial fluid, such as Luminex, can be used to gain a better understanding of the nature of DAMPs released upon FUS + MB BTB/BBB opening

6.5 Investigation of the Microglial Response to FUS + MB BTB/BBB Opening

In Chapter 5 of this dissertation we characterized response of intracranial melanoma tumors to FUS + MB BTB/BBB opening. While we mainly focused on dendritic cells, due to their importance in bridging innate and adaptive immunity and generating antitumor responses, other cell types in the brain may also be important in responding to FUS in brain tumors. Both microglia and perivascular macrophages express pattern recognition receptors, and therefore have the ability to respond to DAMPs generated upon tissue damage(*146*, *147*)(*133*). Stimulation of microglia via DAMPs has been observed in response to CNS injury and infection(*133*) , and these cells have been shown to be activated in response to FUS + MB BBB

opening in normal brain tissue(*96*). Future studies should examine the role of microglia in the response of intracranial melanoma tumor tissue to FUS + MB BTB/BBB opening. To do this we could use similar flow cytometry based methods to probe various aspects of this cells population. Additionally, inhibitors such as PLX3397, a CSF1R inhibitor, can be used to deplete the microglial population in mice(*157*). Such inhibitors can be used as tools to probe whether the response to FUS is altered in the absence of microglia.

6.6 Evaluation of Tumor Cell Expression of Classical MHC Class I Molecules and Antigen Processing and Presentation after FUS + MB BTB/BBB Opening

We observed increased expression of classical MHC class I molecules and transcripts involved in MHC class I peptide processing and presentation in FUS-treated tumors via bulk RNA sequencing. These gene signatures in antigen-presenting cells could support cross-presentation of tumor antigens, but we saw little evidence of increased presentation of the SIINFEKL peptide on dendritic cells. Future studies should interrogate whether this response is primarily occurring in tumor cells, as this could also be beneficial to anti-tumor immunity by making the tumor cells more visible to tumor specific effector T cells. It is known that downregulation of MHC I expression is one mechanism used by tumor cells to evade detection by the immune system(*141–144*).

6.7 Response of T Cell Population to FUS + MB BTB/BBB Opening

In Chapter 5, we did not assess T cell response due to the relatively early timepoints chosen to analyze the tissue response to FUS. Due to the limited and transient nature of the proinflammatory response generated by FUS, we hypothesize that we would not detect FUS-induced increases in T cell activation, but future studies could investigate this further. Particularly, the prevalence of CD11b+ versus CD103+ DC subsets in analyzed tissues, though

not unexpected, may support preferential activation of CD4+ T cells as opposed to CD8+ T cells in this setting, something that could be studied going forward(*130*).

While we did not assess de novo T cell response, we did investigate the ability of FUS + MB BTB/BBB opening to augment homing of adoptively transferred activated T cells to intracranial melanoma tumors. We found no differences in T cell homing to tumors with FUS + MB BTB/BBB opening, however this result may be dictated by the timing of the adoptive transfer relative to the FUS treatment as well as the time of the tissue harvest. For instance, accumulation of HER-2 specific NK-92 cells in a model of HER2+ breast cancer brain metastasis was found to depend upon timing of the cell injection, with greater accumulation achieved when cells were administered immediately prior to FUS + MB BTB/BBB disruption(*61*). Future studies should also investigate whether homing of activated tumor specific T cells can be enhanced by varying the timepoint of adoptive cell transfer with respect to FUS + MB BTB/BBB disruption.

6.8 Summary

Together, this body of work begins to build a platform for use of FUS + MB BTB/BBB opening to be utilized in combination with innovative gene- and immune-based therapeutic strategies for the treatment of brain tumors.

References

1. Q. T. Ostrom, H. Gittleman, P. Liao, C. Rouse, Y. Chen, J. Dowling, Y. Wolinsky, C. Kruchko, J. Barnholtz-Sloan, CBTRUS Statistical Report: Primary Brain and Central Nervous System Tumors Diagnosed in the United States in 2007-2011. *Neuro. Oncol.* **16**, iv1–iv63 (2014).

2. M. Weller, B. Fisher, M. J. B. Taphoorn, K. Belanger, A. A. Brandes, C. Marosi, U. Bogdahn, J. Curschmann, R. C. Janzer, Radiotherapy plus concomitant and adjuvant temozolomide for glioblastoma. *Cancer/Radiothérapie*. **9**, 196–197 (2005).

3. H. Takei, E. Rouah, Y. Ishida, Brain metastasis: clinical characteristics, pathological findings and molecular subtyping for therapeutic implications. *Brain Tumor Pathol.* **33**, 1–12 (2016).

4. H. C. Bauer, I. A. Krizbai, H. Bauer, A. Traweger, “You shall not pass”-tight junctions of the blood-brain barrier. *Front. Neurosci.* **8**, 1–21 (2014).

5. N. J. Abbott, L. Rönnbäck, E. Hansson, Astrocyte-endothelial interactions at the blood-brain barrier. *Nat. Rev. Neurosci.* **7**, 41–53 (2006).

6. N. J. Abbott, Blood-brain barrier structure and function and the challenges for CNS drug delivery. *J. Inherit. Metab. Dis.* **36**, 437–449 (2013).

7. W. Löscher, H. Potschka, Drug resistance in brain diseases and the role of drug efflux transporters. *Nat. Rev. Neurosci.* **6**, 591–602 (2005).

8. W. M. Pardridge, The blood-brain barrier: bottleneck in brain drug development. *NeuroRx*. **2**, 3–14 (2005).

9. O. Van Tellingen, B. Yetkin-arik, M. C. De Gooijer, P. Wesseling, T. Wurdinger, H. E. De Vries, Overcoming the blood – brain tumor barrier for effective glioblastoma treatment.

Drug Resist. Updat. **19**, 1–12 (2015).

10. P. Carmeliet, R. K. Jain, Angiogenesis in Cancer and Other Diseases. *Nature*. **407**, 249–257 (2000).

11. R. K. Jain, Normalization of Tumor Vasculature: An Emerging Concept in Antiangiogenic Therapy. *Science (80-.).* **307**, 58–62 (2005).

12. R. K. Jain, T. Stylianopoulos, Delivering nanormedicine to solid tumors. *Nat. Rev. Clin. Oncol.* **7**, 653–664 (2010).

13. P. R. Lockman, R. K. Mittapalli, K. S. Taskar, V. Rudraraju, B. Gril, K. A. Bohn, C. E. Adkins, A. Roberts, H. R. Thorsheim, J. A. Gaasch, S. Huang, D. Palmieri, P. S. Steeg, Q. R. Smith, Heterogeneous blood-tumor barrier permeability determines drug efficacy in experimental brain metastases of breast cancer. *Clin. Cancer Res.* **16**, 5664–5678 (2010).

14. S. Puhalla, W. Elmquist, D. Freyer, L. Kleinberg, C. Adkins, P. Lockman, J. McGregor, L. Muldoon, G. Nesbit, D. Peereboom, Q. Smith, S. Walker, E. Neuwelt, Unsanctifying the sanctuary: Challenges and opportunities with brain metastases. *Neuro. Oncol.* **17**, 639–651 (2015).

15. R. K. Oberoi, K. E. Parrish, T. T. Sio, R. K. Mittapalli, W. F. Elmquist, J. N. Sarkaria, Strategies to improve delivery of anticancer drugs across the blood-brain barrier to treat glioblastoma. *Neuro. Oncol.* **18**, 27–36 (2016).

16. L. C. Hou, A. Veeravagu, A. R. Hsu, V. C. K. Tse, Recurrent glioblastoma multiforme: a review of natural history and management options. *Neurosurg. Focus*. **20** (2006), doi:10.3171/foc.2006.20.4.2.

17. C. Nicholson, Diffusion in Brain Extracellular Space. **6**, 1277–1340 (2008).

18. M. Westphal, D. C. Hilt, E. Bortey, P. Delavault, R. Olivares, P. C. Warnke, I. R. Whittle, J. Jääskeläinen, Z. Ram, A phase 3 trial of local chemotherapy with biodegradable carmustine (BCNU) wafers (Gliadel wafers) in patients with primary malignant glioma. *Neuro. Oncol.* **5**, 79–88 (2004).

19. H. Brem, S. Piantadosi, P. C. Burger, M. Walker, R. Selker, N. A. Vick, K. Black, M. Sisti, S. Brem, G. Mohr, P. Muller, R. Morawetz, S. C. Schold, Placebo-controlled trial of safety and efficacy of intraoperative controlled delivery by biodegradable polymers of chemotherapy for recurrent gliomas. *Lancet*. **345**, 1008–1012 (1995).

20. S. Valtonen, U. Timonen, P. Toivanen, H. Kalimo, L. Kivipelto, O. Heiskanen, G. Unsgaard, T. Kuurne, Interstitial chemotherapy with carmustine-loaded polymers for high-grade gliomas: A randomized double-blind study. *Neurosurgery*. **41**, 44–49 (1997).

21. L. K. Fung, M. G. Ewend, A. Sills, E. P. Sipos, R. Thompson, M. Watts, O. M. Colvin, H. Brem, W. M. Saltzman, Pharmacokinetics of interstitial delivery of carmustine, 4-hydroperoxycyclophosphamide, and paclitaxel from a biodegradable polymer implant in the monkey brain. *Cancer Res.* **58**, 672–684 (1998).

22. R. R. Lonser, M. Sarntinoranont, P. F. Morrison, E. H. Oldfield, Convection-enhanced delivery to the central nervous system. **122**, 697–706 (2015).

23. A. Jahangiri, A. T. Chin, P. M. Flanigan, R. Chen, K. Bankiewicz, M. K. Aghi, Convection-enhanced delivery in glioblastoma: a review of preclinical and clinical studies. *J. Neurosurg.* **126**, 191–200 (2017).

24. R. A. Kroll, E. A. Neuwelt, Outwitting the blood-brain barrier for therapeutic purposes: Osmotic opening and other means. *Neurosurgery*. **42**, 1083–1100 (1998).

25. M. W. Brightman, M. Hori, S. I. Rapoport, T. S. Reese, E. Westergaard, Osmotic opening

of tight junctions in cerebral endothelium. *J. Comp. Neurol.* **152**, 317–325 (1973).

26. E. M. Kemper, W. Boogerd, I. Thuis, J. H. Beijnen, O. van Tellingen, Modulation of the blood-brain barrier in oncology: Therapeutic opportunities for the treatment of brain tumours? *Cancer Treat. Rev.* **30**, 415–423 (2004).

27. C. V. Borlongan, D. F. Emerich, Facilitation of drug entry into the CNS via transient permeation of blood-brain barrier: Laboratory and preliminary clinical evidence from bradykinin receptor agonist, Cereport. *Brain Res. Bull.* **60**, 297–306 (2003).

28. J. Xie, Z. Shen, Y. Anraku, K. Kataoka, X. Chen, Nanomaterial-based blood-brain-barrier (BBB) crossing strategies. *Biomaterials*. **224**, 119491 (2019).

29. N. Lipsman, Y. Meng, A. J. Bethune, Y. Huang, B. Lam, M. Masellis, N. Herrmann, C. Heyn, I. Aubert, A. Boutet, G. S. Smith, K. Hynynen, S. E. Black, Blood–brain barrier opening in Alzheimer's disease using MR-guided focused ultrasound. *Nat. Commun.* **9**, 1–8 (2018).

30. A. Abrahao, Y. Meng, M. Llinas, Y. Huang, C. Hamani, T. Mainprize, I. Aubert, C. Heyn, S. E. Black, K. Hynynen, N. Lipsman, L. Zinman, First-in-human trial of blood-brain barrier opening in amyotrophic lateral sclerosis using MR-guided focused ultrasound. *Nat. Commun.*, 1–9 (2019).

31. T. Mainprize, N. Lipsman, Y. Huang, Y. Meng, A. Bethune, S. Ironside, C. Heyn, R. Alkins, M. Trudeau, A. Sahgal, J. Perry, K. Hynynen, Blood-Brain Barrier Opening in Primary Brain Tumors with Non-invasive MR-Guided Focused Ultrasound: A Clinical Safety and Feasibility Study. *Sci. Rep.* **9**, 321 (2019).

32. K. B. Bader, C. K. Holland, Gauging the likelihood of stable cavitation from ultrasound contrast agents. **58**, 127–144 (2015).

33. R. E. Apfel, Acoustic cavitation: A possible consequence of biomedical uses of ultrasound. *Br. J. Cancer*. **45**, 140–146 (1982).

34. J. A. Rooney, Shear as a Mechanism for Sonically Induced Biological Effects. *J. Acoust. Soc. Am.* **52**, 1718–1724 (1972).

35. N. Sheikov, N. McDannold, N. Vykhodtseva, F. Jolesz, K. Hynynen, Cellular mechanisms of the blood-brain barrier opening induced by ultrasound in presence of microbubbles. *Ultrasound Med. Biol.* **30**, 979–989 (2004).

36. N. Sheikov, N. McDannold, F. Jolesz, Y. Z. Zhang, K. Tam, K. Hynynen, Brain arterioles show more active vesicular transport of blood-borne tracer molecules than capillaries and venules after focused ultrasound-evoked opening of the blood-brain barrier. *Ultrasound Med. Biol.* **32**, 1399–1409 (2006).

37. N. Sheikov, N. McDannold, S. Sharma, K. Hynynen, Effect of Focused Ultrasound Applied with an Ultrasound Contrast Agent on the Tight Junctional Integrity of the Brain Microvascular Endothelium. *Ultrasound Med. Biol.* **34**, 1093–1104 (2008).

38. M. Aryal, K. Fischer, C. Gentile, S. Gitto, Y. Z. Zhang, N. McDannold, Effects on P-glycoprotein expression after blood-brain barrier disruption using focused ultrasound and microbubbles. *PLoS One*. **12**, 1–15 (2017).

39. C. Y. Xia, Y. H. Liu, P. Wang, Y. X. Xue, Low-frequency ultrasound irradiation increases blood-tumor barrier permeability by transcellular pathway in a rat glioma model. *J. Mol. Neurosci.* **48**, 281–290 (2012).

40. C. D. Arvanitis, V. Askoxylakis, Y. Guo, M. Datta, J. Kloepper, G. B. Ferraro, M. O. Bernabeu, D. Fukumura, N. McDannold, R. K. Jain, Mechanisms of enhanced drug delivery in brain metastases with focused ultrasound-induced blood–tumor barrier

disruption. *Proc. Natl. Acad. Sci.*, 201807105 (2018).

41. T. Sun, Y. Zhang, C. Power, P. M. Alexander, J. T. Sutton, M. Aryal, N. Vykhodtseva, E. L. Miller, N. J. McDannold, Closed-loop control of targeted ultrasound drug delivery across the blood–brain/tumor barriers in a rat glioma model. *Proc. Natl. Acad. Sci.* **114**, E10281–E10290 (2017).

42. N. McDannold, Y. Zhang, J. G. Supko, C. Power, T. Sun, C. Peng, N. Vykhodtseva, A. J. Golby, D. A. Reardon, Acoustic feedback enables safe and reliable carboplatin delivery across the blood-brain barrier with a clinical focused ultrasound system and improves survival in a rat glioma model. *Theranostics*. **9**, 6284–6299 (2019).

43. R. Stupp, M. E. Hegi, W. P. Mason, M. J. van den Bent, M. J. B. Taphoorn, R. C. Janzer, S. K. Ludwin, A. Allgeier, B. Fisher, K. Belanger, P. Hau, A. a Brandes, J. Gijtenbeek, C. Marosi, C. J. Vecht, K. Mokhtari, P. Wesseling, S. Villa, E. Eisenhauer, T. Gorlia, M. Weller, D. Lacombe, J. G. Cairncross, R.-O. Mirimanoff, Effects of radiotherapy with concomitant and adjuvant temozolomide versus radiotherapy alone on survival in glioblastoma in a randomised phase III study: 5-year analysis of the EORTC-NCIC trial. *Lancet Oncol.* **10**, 459–66 (2009).

44. K. C. Wei, P. C. Chu, H. Y. J. Wang, C. Y. Huang, P. Y. Chen, H. C. Tsai, Y. J. Lu, P. Y. Lee, I. C. Tseng, L. Y. Feng, P. W. Hsu, T. C. Yen, H. L. Liu, Focused Ultrasound-Induced Blood-Brain Barrier Opening to Enhance Temozolomide Delivery for Glioblastoma Treatment: A Preclinical Study. *PLoS One*. **8**, 1–10 (2013).

45. H. L. Liu, C. Y. Huang, J. Y. Chen, H. Y. J. Wang, P. Y. Chen, K. C. Wei, Pharmacodynamic and therapeutic investigation of focused ultrasound-induced blood-brain barrier opening for enhanced temozolomide delivery in glioma treatment. *PLoS One*. **9**, 1–19 (2014).

46. Z. Kovacs, B. Werner, A. Rassi, J. O. Sass, E. Martin-Fiori, M. Bernasconi, Prolonged survival upon ultrasound-enhanced doxorubicin delivery in two syngenic glioblastoma mouse models. *J. Control. Release*. **187**, 74–82 (2014).

47. N. Park, Juyoung, Aryal, Muna, Vykhodtseva, Natalia, Zhang, Yong-Zhi, McDannold, Evaluation of permeability, doxorubicin delivery, and drug retention in a rat brain tumor model after ultrasound-induced blood-tumor barrier disruption. *J. Control. Release*. **250**, 77–85 (2017).

48. Y. L. Lin, M. T. Wu, F. Y. Yang, Pharmacokinetics of doxorubicin in glioblastoma multiforme following ultrasound-Induced blood-brain barrier disruption as determined by microdialysis. *J. Pharm. Biomed. Anal.* **149**, 482–487 (2018).

49. H.-L. Liu, M. Hua, P.-Y. Chen, P.-C. Chu, C.-H. Pan, H.-W. Yang, C.-Y. Huang, J.-J. Wang, T.-C. Yen, K.-C. Wei, Blood-Brain Barrier Disruption with Focused Ultrasound Enhances Delivery of Chemotherapeutic Drugs for Glioblastoma Treatment. *Ultrasound Med. Biol.* **255**, 834–40 (2010).

50. M. Aryal, J. Park, N. Vykhodtseva, Y.-Z. Zhang, N. McDannold, Enhancement in blood-tumor barrier permeability and delivery of liposomal doxorubicin using focused ultrasound and microbubbles: evaluation during tumor progression in a rat glioma model. *Phys. Med. Biol.* **60**, 2511–2527 (2015).

51. M. Aryal, N. Vykhodtseva, Y. Z. Zhang, J. Park, N. McDannold, Multiple treatments with liposomal doxorubicin and ultrasound-induced disruption of blood-tumor and blood-brain barriers improve outcomes in a rat glioma model. *J. Control. Release*. **169**, 103–111 (2013).

52. F. Y. Yang, T. T. Wong, M. C. Teng, R. S. Liu, M. Lu, H. F. Liang, M. C. Wei, Focused ultrasound and interleukin-4 receptor-targeted liposomal doxorubicin for enhanced

targeted drug delivery and antitumor effect in glioblastoma multiforme. *J. Control. Release*. **160**, 652–658 (2012).

53. L. H. Treat, N. McDannold, Y. Zhang, N. Vykhodtseva, K. Hynynen, Improved anti-tumor effect of liposomal doxorubicin after targeted blood-brain barrier disruption by MRI-guided focused ultrasound in rat glioma. *Ultrasound Med. Biol.* **38**, 1716–1725 (2012).

54. F. Y. Yang, H. E. Wang, R. S. Liu, M. C. Teng, J. J. Li, M. Lu, M. C. Wei, T. T. Wong, Pharmacokinetic Analysis of 111In-Labeled Liposomal Doxorubicin in Murine Glioblastoma after Blood-Brain Barrier Disruption by Focused Ultrasound. *PLoS One*. **7**, 1–7 (2012).

55. M. Aryal, N. Vykhodtseva, Y.-Z. Zhang, N. McDannold, Multiple sessions of liposomal doxorubicin delivery via focused ultrasound mediated blood-brain barrier disruption: a safety study. *J. Control. Release*. **204**, 60–9 (2015).

56. K. F. Timbie, U. Afzal, A. Date, C. Zhang, J. Song, G. Wilson Miller, J. S. Suk, J. Hanes, R. J. Price, MR image-guided delivery of cisplatin-loaded brain-penetrating nanoparticles to invasive glioma with focused ultrasound. *J. Control. Release*. **263**, 120–131 (2017).

57. C. H. Fan, Y. H. Cheng, C. Y. Ting, Y. J. Ho, P. H. Hsu, H. L. Liu, C. K. Yeh, Ultrasound/magnetic targeting with SPIO-DOX-microbubble complex for image-guided drug delivery in brain tumors. *Theranostics*. **6**, 1542–1556 (2016).

58. T. Kobus, I. K. Zervantonakis, Y. Zhang, N. J. McDannold, Growth inhibition in a brain metastasis model by antibody delivery using focused ultrasound-mediated blood-brain barrier disruption. *J. Control. Release*. **238**, 281–288 (2016).

59. H.-L. Liu, P.-H. Hsu, C.-Y. Lin, C.-W. Huang, W.-Y. Chai, P.-C. Chu, C.-Y. Huang, P.-Y. Chen, L.-Y. Yang, J. S. Kuo, K.-C. Wei, Focused ultrasound enhances central nervous

system delivery of Bevacizumab for malignant glioma treatment. *Radiology*. **281**, 99–108 (2016).

60. P.-Y. Chen, H.-Y. Hsieh, C.-Y. Huang, C.-Y. Lin, K.-C. Wei, H.-L. Liu, Focused ultrasound-induced blood-brain barrier opening to enhance interleukin-12 delivery for brain tumor immunotherapy: a preclinical feasibility study. *J. Transl. Med.* **13**, 93 (2015).

61. R. Alkins, A. Burgess, M. Ganguly, G. Francia, R. Kerbel, W. S. Wels, K. Hynynen, Focused ultrasound delivers targeted immune cells to metastatic brain tumors. *Cancer Res.* **73**, 1892–1899 (2013).

62. R. Alkins, A. Burgess, R. Kerbel, W. S. Wels, K. Hynynen, Early treatment of HER2-amplified brain tumors with targeted NK-92 cells and focused ultrasound improves survival. *Neuro. Oncol.* **18**, 974–981 (2016).

63. S. Wang, O. O. Olumolade, T. Sun, G. Samiotaki, E. E. Konofagou, Noninvasive, neuron-specific gene therapy can be facilitated by focused ultrasound and recombinant adeno-associated virus. *Gene Ther.* **22**, 104–110 (2015).

64. P. H. Hsu, K. C. Wei, C. Y. Huang, C. J. Wen, T. C. Yen, C. L. Liu, Y. T. Lin, J. C. Chen, C. R. Shen, H. L. Liu, Noninvasive and Targeted Gene Delivery into the Brain Using Microbubble-Facilitated Focused Ultrasound. *PLoS One*. **8**, 1–8 (2013).

65. E. L. Chang, C. Y. Ting, P. H. Hsu, Y. C. Lin, E. C. Liao, C. Y. Huang, Y. C. Chang, H. L. Chan, C. S. Chiang, H. L. Liu, K. C. Wei, C. H. Fan, C. K. Yeh, Angiogenesis-targeting microbubbles combined with ultrasound-mediated gene therapy in brain tumors. *J. Control. Release*. **255**, 164–175 (2017).

66. G. Zhao, Q. Huang, F. Wang, X. Zhang, J. Hu, Y. Tan, N. Huang, Z. Wang, Z. Wang, Y. Cheng, Targeted shRNA-loaded liposome complex combined with focused ultrasound for

blood-brain barrier disruption and suppressing glioma growth. *Cancer Lett.* **418**, 147–158 (2018).

67. P. Yue, W. Miao, L. Gao, X. Zhao, J. Teng, Ultrasound-triggered effects of the microbubbles coupled to GDNF plasmid-loaded PEGylated liposomes in a rat model of Parkinson's disease. *Front. Neurosci.* **12**, 1–9 (2018).

68. P. Yue, L. Gao, X. Wang, X. Ding, J. Teng, Ultrasound-triggered effects of the microbubbles coupled to GDNF- and Nurr1-loaded PEGylated liposomes in a rat model of Parkinson's disease. *J. Cell. Biochem.* **119**, 4581–4591 (2018).

69. C. H. Fan, C. Y. Ting, C. Y. Lin, H. L. Chan, Y. C. Chang, Y. Y. Chen, H. L. Liu, C. K. Yeh, Noninvasive, Targeted, and Non-Viral Ultrasound-Mediated GDNF-Plasmid Delivery for Treatment of Parkinson's Disease. *Sci. Rep.* **6**, 1–11 (2016).

70. M. E. Karakatsani, S. Wang, G. Samiotaki, T. Kugelman, O. O. Olumolade, C. Acosta, T. Sun, Y. Han, H. A. S. Kamimura, V. Jackson-Lewis, S. Przedborski, E. Konofagou, Amelioration of the nigrostriatal pathway facilitated by ultrasound-mediated neurotrophic delivery in early Parkinson's disease. *J. Control. Release*. **303**, 289–301 (2019).

71. S. Wang, T. Kugelman, A. Buch, M. Herman, Y. Han, M. E. Karakatsani, S. A. Hussaini, K. Duff, E. E. Konofagou, Non-invasive, Focused Ultrasound-Facilitated Gene Delivery for Optogenetics. *Sci. Rep.* **7**, 1–7 (2017).

72. A. Alonso, E. Reinz, B. Leuchs, J. Kleinschmidt, M. Fatar, B. Geers, I. Lentacker, M. G. Hennerici, S. C. de Smedt, S. Meairs, A. Tyagi, Focal delivery of AAV2/1-transgenes into the rat brain by localized ultrasound-induced BBB Opening. *Ann. Neurosci.* **21**, 22 (2014).

73. M. A. Stavarache, N. Petersen, E. M. Jurgens, E. R. Milstein, Z. B. Rosenfeld, D. J. Ballon, M. G. Kaplitt, Safe and stable noninvasive focal gene delivery to the mammalian

brain following focused ultrasound. *J. Neurosurg.*, 1–10 (2018).

74. K. Xhima, F. Nabbouh, K. Hynynen, I. Aubert, A. Tandon, Noninvasive delivery of an α-synuclein gene silencing vector with magnetic resonance–guided focused ultrasound. *Mov. Disord.* **33**, 1567–1579 (2018).

75. E. Thévenot, J. F. Jordão, M. A. O'Reilly, K. Markham, Y.-Q. Weng, K. D. Foust, B. K. Kaspar, K. Hynynen, I. Aubert, Targeted delivery of self-complementary adeno-associated virus serotype 9 to the brain, using magnetic resonance imaging-guided focused ultrasound. *Hum. Gene Ther.* **23**, 1144–1155 (2012).

76. Q. Huang, J. Deng, F. Wang, S. Chen, Y. Liu, Z. Wang, Z. Wang, Y. Cheng, Targeted gene delivery to the mouse brain by MRI-guided focused ultrasound-induced blood-brain barrier disruption. *Exp. Neurol.* **233**, 350–356 (2012).

77. C. H. Fan, E. L. Chang, C. Y. Ting, Y. C. Lin, E. C. Liao, C. Y. Huang, Y. C. Chang, H. L. Chan, K. C. Wei, C. K. Yeh, Folate-conjugated gene-carrying microbubbles with focused ultrasound for concurrent blood-brain barrier opening and local gene delivery. *Biomaterials*. **106**, 46–57 (2016).

78. C. Y. Lin, H. Y. Hsieh, W. G. Pitt, C. Y. Huang, I. C. Tseng, C. K. Yeh, K. C. Wei, H. L. Liu, Focused ultrasound-induced blood-brain barrier opening for non-viral, non-invasive, and targeted gene delivery. *J. Control. Release*. **212**, 1–9 (2015).

79. C. Y. Lin, H. Y. Hsieh, C. M. Chen, S. R. Wu, C. H. Tsai, C. Y. Huang, M. Y. Hua, K. C. Wei, C. K. Yeh, H. L. Liu, Non-invasive, neuron-specific gene therapy by focused ultrasound-induced blood-brain barrier opening in Parkinson's disease mouse model. *J. Control. Release*. **235**, 72–81 (2016).

80. C. Y. Lin, H. Y. Hsieh, W. G. Pitt, C. Y. Huang, I. C. Tseng, C. K. Yeh, K. C. Wei, H. L.

Liu, Focused ultrasound-induced blood-brain barrier opening for non-viral, non-invasive, and targeted gene delivery. *J. Control. Release*. **212**, 1–9 (2015).

81. Y. Negishi, M. Yamane, N. Kurihara, Y. Endo-Takahashi, S. Sashida, N. Takagi, R. Suzuki, K. Maruyama, Enhancement of blood–brain barrier permeability and delivery of antisense oligonucleotides or plasmid DNA to the brain by the combination of bubble liposomes and high-intensity focused ultrasound. *Pharmaceutics*. **7**, 344–362 (2015).

82. L. Long, X. Cai, R. Guo, P. Wang, L. Wu, T. Yin, S. Liao, Z. Lu, Treatment of Parkinson's disease in rats by Nrf2 transfection using MRI-guided focused ultrasound delivery of nanomicrobubbles. *Biochem. Biophys. Res. Commun.* **482**, 75–80 (2017).

83. B. P. Mead, P. Mastorakos, J. S. Suk, A. L. Klibanov, J. Hanes, R. J. Price, Targeted gene transfer to the brain via the delivery of brain-penetrating DNA nanoparticles with focused ultrasound. *J. Control. Release*. **223**, 109–117 (2016).

84. M. Pan, Y. Zhang, Z. Deng, F. Yan, G. Hong, Noninvasive and Local Delivery of Adenoviral-Mediated Herpes Simplex Virus Thymidine Kinase to Treat Glioma Through Focused Ultrasound-Induced Blood-Brain Barrier Opening in Rats. *J. Biomed. Nanotechnol.* **14**, 2031–2041 (2018).

85. K. Negron, N. Khalasawi, B. Lu, C.-Y. Ho, J. Lee, S. Shenoy, H.-Q. Mao, T.-H. Wang, J. Hanes, J. S. Suk, Widespread gene transfer to malignant gliomas with In vitro-to-In vivo correlation. *J. Control. Release*. **303**, 1–11 (2019).

86. B. P. Mead, N. Kim, G. W. Miller, D. Hodges, P. Mastorakos, A. L. Klibanov, J. W. Mandell, J. Hirsh, J. S. Suk, J. Hanes, R. J. Price, Novel Focused Ultrasound Gene Therapy Approach Noninvasively Restores Dopaminergic Neuron Function in a Rat Parkinson's Disease Model. *Nano Lett.* **17**, 3533–3542 (2017).

87. P. Mastorakos, C. Zhang, S. Berry, Y. Oh, S. Lee, C. G. Eberhart, G. F. Woodworth, J. S. Suk, J. Hanes, Highly PEGylated DNA Nanoparticles Provide Uniform and Widespread Gene Transfer in the Brain. *Adv. Healthc. Mater.* **4**, 1023–1033 (2015).

88. D. S. Hersh, B. A. Nguyen, J. G. Dancy, A. R. Adapa, J. A. Winkles, G. F. Woodworth, A. J. Kim, V. Frenkel, Pulsed ultrasound expands the extracellular and perivascular spaces of the brain. *Brain Res.* **1646**, 543–550 (2016).

89. D. S. Hersh, P. Anastasiadis, A. Mohammadabadi, B. A. Nguyen, S. Guo, J. A. Winkles, A. J. Kim, R. Gullapalli, A. Keller, V. Frenkel, G. F. Woodworth, MR-guided transcranial focused ultrasound safely enhances interstitial dispersion of large polymeric nanoparticles in the living brain. *PLoS One*. **13**, 1–19 (2018).

90. S. Wang, M. E. Karakatsani, C. Fung, T. Sun, C. Acosta, E. Konofagou, Direct brain infusion can be enhanced with focused ultrasound and microbubbles. *J. Cereb. Blood Flow Metab.* **37**, 706–714 (2017).

91. A. Khaibullina, B. S. Jang, H. Sun, N. Le, S. Yu, V. Frenkel, J. A. Carrasquillo, I. Pastan, K. C. P. Li, C. H. Paik, Pulsed high-intensity focused ultrasound enhances uptake of radiolabeled monoclonal antibody to human epidermoid tumor in nude mice. *J. Nucl. Med.* **49**, 295–302 (2008).

92. S. Wang, I. S. Shin, H. Hancock, B. Jang, H. Kim, S. M. Lee, V. Zderic, V. Frenkel, I. Pastan, C. H. Paik, M. R. Dreher, Pulsed High Intensity Focused Ultrasound Increases Penetration and Therapeutic Efficacy of Monoclonal Antibodies in Murine Xenograft Tumors. **162**, 218–224 (2012).

93. S. Lee, H. Han, H. Koo, J. H. Na, H. Y. Yoon, K. E. Lee, H. Lee, H. Kim, I. C. Kwon, K. Kim, Extracellular matrix remodeling in vivo for enhancing tumor-targeting efficiency of nanoparticle drug carriers using the pulsed high intensity focused ultrasound. *J. Control.*

Release. **263**, 68–78 (2017).

94. A. Ziadloo, J. Xie, V. Frenkel, Pulsed focused ultrasound exposures enhance locally administered gene therapy in a murine solid tumor model. *J. Acoust. Soc. Am.* **133**, 1827–1834 (2013).

95. B. P. Mead, C. T. Curley, N. Kim, K. Negron, W. J. Garrison, J. Song, D. Rao, G. W. Miller, J. W. Mandell, B. W. Purow, J. S. Suk, J. Hanes, R. J. Price, Focused Ultrasound Preconditioning for Augmented Nanoparticle Penetration and Efficacy in the Central Nervous System. *Small*. **1903460**, 1–6 (2019).

96. Z. I. Kovacs, S. Kim, N. Jikaria, F. Qureshi, B. Milo, B. K. Lewis, M. Bresler, S. R. Burks, J. A. Frank, Disrupting the blood–brain barrier by focused ultrasound induces sterile inflammation. *Proc. Natl. Acad. Sci. U. S. A.* **114**, E75–E84 (2017).

97. H.-L. Liu, Y.-Y. Wai, P.-H. Hsu, L.-A. Lyu, J.-S. Wu, C.-R. Shen, J.-C. Chen, T.-C. Yen, J.-J. Wang, In vivo assessment of macrophage CNS infiltration during disruption of the blood-brain barrier with focused ultrasound: a magnetic resonance imaging study. *J. Cereb. Blood Flow Metab.* **30**, 177–186 (2010).

98. D. McMahon, R. Bendayan, K. Hynynen, Acute effects of focused ultrasound-induced increases in blood-brain barrier permeability on rat microvascular transcriptome. *Sci. Rep.* **7**, 45657 (2017).

99. G. Leinenga, J. Götz, Scanning ultrasound removes amyloid-β and restores memory in an Alzheimer's disease mouse model. *Sci. Transl. Med.* **7**, 278ra33 (2015).

100. J. F. Jordão, E. Thévenot, K. Markham-Coultes, T. Scarcelli, Y.-Q. Weng, K. Xhima, M. O'Reilly, Y. Huang, J. McLaurin, K. Hynynen, I. Aubert, Amyloid-β plaque reduction, endogenous antibody delivery and glial activation by brain-targeted, transcranial focused

ultrasound. *Exp. Neurol.* **248**, 16–29 (2013).

101. D. S. Chen, I. Mellman, Oncology meets immunology: The cancer-immunity cycle. *Immunity*. **39**, 1–10 (2013).

102. I. Mellman, Dendritic cells: master regulators of the immune response. *Cancer Immunol. Res.* **1**, 145–149 (2013).

103. G. F. Woodworth, G. P. Dunn, E. a Nance, J. Hanes, H. Brem, Emerging insights into barriers to effective brain tumor therapeutics. *Front. Oncol.* **4**, 126 (2014).

104. N. Sheikov, N. J. McDannold, S. Sharma, K. Hynynen, Effect of focused ultrasound applied with an ultrasound contrast agent on the tight junctional integrity of the brain microvascular endothelium. *Ultrasound Med. Biol.* **34**, 1093–104 (2008).

105. K. F. Timbie, B. P. Mead, R. J. Price, Drug and gene delivery across the blood–brain barrier with focused ultrasound. *J. Control. Release*. **219**, 61–75 (2015).

106. E. Nance, K. Timbie, G. W. Miller, J. Song, C. Louttit, A. L. Klibanov, T.-Y. Shih, G. Swaminathan, R. J. Tamargo, G. F. Woodworth, J. Hanes, R. J. Price, Non-invasive delivery of stealth, brain-penetrating nanoparticles across the blood-brain barrier using MRI-guided focused ultrasound. *J. Control. Release*. **189**, 123–132 (2014).

107. E.-J. Park, Y.-Z. Zhang, N. Vykhodtseva, N. McDannold, Ultrasound-mediated blood-brain/blood-tumor barrier disruption improves outcomes with trastuzumab in a breast cancer brain metastasis model. *J. Control. Release*. **163**, 277–284 (2012).

108. M. Kinoshita, N. McDannold, F. A. Jolesz, K. Hynynen, Noninvasive localized delivery of Herceptin to the mouse brain by MRI-guided focused ultrasound-induced blood-brain barrier disruption. *Proc. Natl. Acad. Sci. U. S. A.* **103**, 11719–11723 (2006).

109. K. M. Kingsmore, A. Vaccari, D. Abler, S. X. Cui, F. H. Epstein, R. C. Rockne, S. T.

Acton, J. M. Munson, MRI analysis to map interstitial flow in the brain tumor microenvironment. *APL Bioeng.* **2**, 031905 (2018).

110. M. Gerstenmayer, B. Fellah, R. Magnin, E. Selingue, B. Larrat, Acoustic Transmission Factor through the Rat Skull as a Function of Body Mass, Frequency and Position. *Ultrasound Med. Biol.* **44**, 2336–2344 (2018).

111. J. J. Choi, M. Pernot, S. A. Small, E. E. Konofagou, Noninvasive, transcranial and localized opening of the blood-brain barrier using focused ultrasound in mice. *Ultrasound Med. Biol.* **33**, 95–104 (2007).

112. Y.-S. Tung, F. Vlachos, J. a Feshitan, M. a Borden, E. E. Konofagou, The mechanism of interaction between focused ultrasound and microbubbles in blood-brain barrier opening in mice. *J. Acoust. Soc. Am.* **130**, 3059–67 (2011).

113. H. Chen, E. E. Konofagou, The size of blood – brain barrier opening induced by focused ultrasound is dictated by the acoustic pressure. *J. Cereb. Blood Flow Metab.* **34**, 1197–1204 (2014).

114. C. T. Curley, N. D. Sheybani, T. N. Bullock, R. J. Price, Focused ultrasound immunotherapy for central nervous system pathologies: challenges and opportunities. *Theranostics*. **7**, 3608-3623. (2017).

115. J. Suk, Jung Soo, Kim, Anthony J., Trehan, Kania, Schneider, Craig S., Cebotaru, Liudmila, Woodward, Owen M., Boylan, Nicholas J., Boyle, Michael P., Lai, Samuel K., Guggino, William B., Hanes, Lung Gene Therapy with Highly Compacted DNA Nanoparticles that Overcome the Mucus Barrier. *J. Control. Release*. **178**, 8–17 (2014).

116. C. W. Burke, J. S. Suk, A. J. Kim, Y.-H. J. Hsiang, A. L. Klibanov, J. Hanes, R. J. Price, Markedly enhanced skeletal muscle transfection achieved by the ultrasound-targeted

delivery of non-viral gene nanocarriers with microbubbles. *J. Control. Release*. **162**, 414–421 (2012).

117. R. K. Baxter, Laurenc T., Jain, Transport of Fluid and Macromolecules in Tumors I. Role of Interstital Pressure and Convection. *Microvasc. Res.* **37**, 77–104 (1989).

118. K. Hynynen, N. McDannold, N. a Sheikov, F. a Jolesz, N. Vykhodtseva, Local and reversible blood-brain barrier disruption by noninvasive focused ultrasound at frequencies suitable for trans-skull sonications. *Neuroimage*. **24**, 12–20 (2005).

119. S. K. Wu, C. F. Chiang, Y. H. Hsu, T. H. Lin, H. C. Liou, W. M. Fu, W. L. Lin, Short-time focused ultrasound hyperthermia enhances liposomal doxorubicin delivery and antitumor efficacy for brain metastasis of breast cancer. *Int. J. Nanomedicine*. **9**, 4485–4494 (2014).

120. S. K. Wu, C. F. Chiang, Y. H. Hsu, H. C. Liou, W. M. Fu, W. L. Lin, Pulsed-wave low-dose ultrasound hyperthermia selectively enhances nanodrug delivery and improves antitumor efficacy for brain metastasis of breast cancer. *Ultrason. Sonochem.* **36**, 198–205 (2017).

121. F. Faul, E. Erdfelder, A. G. Lang, A. Buchner, G*Power 3: A flexible statistical power analysis program for the social, behavioral, and biomedical sciences. *Behav. Res. Methods*. **39**, 175–191 (2007).

122. J. Cohen, *Statistical Power Analysis for the Behavioral Sciences* (Routledge Academic, New York, NY, 1988).

123. G. C. Van Rhoon, T. Samaras, P. S. Yarmolenko, M. W. Dewhirst, E. Neufeld, N. Kuster, CEM43°C thermal dose thresholds: A potential guide for magnetic resonance radiofrequency exposure levels? *Eur. Radiol.* **23**, 2215–2227 (2013).

124. Y. Boucher, H. Salehi, B. Witwer, G. R. Harsh, R. K. Jain, Interstitial fluid pressure in intracranial tumours in patients and in rodents. *Br. J. Cancer*. **75**, 829–836 (1997).

125. L. Nayak, E. Q. Lee, P. Y. Wen, Epidemiology of brain metastases. *Curr. Oncol. Rep.* **14**, 48–54 (2012).

126. D. M. Pardoll, The blockade of immune checkpoints in cancer immunotherapy. *Nat. Rev. Cancer*. **12**, 252–64 (2012).

127. J. J. Luke, K. T. Flaherty, A. Ribas, G. V. Long, Targeted agents and immunotherapies: Optimizing outcomes in melanoma. *Nat. Rev. Clin. Oncol.* **14**, 463–482 (2017).

128. M. B. Headley, A. Bins, A. Nip, E. W. Roberts, M. R. Looney, A. Gerard, M. F. Krummel, Visualization of Immediate Immune Responses to Pioneer Metastatic Cells in the Lung. *Nature*. **531**, 513–517 (2016).

129. A. Louveau, B. A. Plog, S. Antila, K. Alitalo, M. Nedergaard, J. Kipnis, Understanding the functions and relationships of the glymphatic system and meningeal lymphatics. *J. Clin. Invest.* **127**, 3210–3219 (2017).

130. J. P. Böttcher, C. Reis e Sousa, The Role of Type 1 Conventional Dendritic Cells in Cancer Immunity. *Trends in Cancer*. **4**, 784–792 (2018).

131. H. S. Goodridge, C. N. Reyes, C. A. Becker, T. R. Katsumoto, J. Ma, A. J. Wolf, N. Bose, A. S. H. Chan, A. S. Magee, M. E. Danielson, A. Weiss, J. P. Vasilakos, D. M. Underhill, Activation of the innate immune receptor Dectin-1 upon formation of a ~ Phagocytic synapse-TM. *Nature*. **472**, 471–475 (2011).

132. J. Pugin, D. Heumann, A. Tomasz, V. V. Kravchenko, Y. Akamatsu, M. Nishijima, M. P. Glauser, P. S. Tobias, R. J. Ulevitch, CD14 Is a pattern recognition receptor. *Immunity*. **1**, 509–516 (1994).

133. H. Janova, C. Böttcher, I. R. Holtman, T. Regen, D. van Rossum, A. Götz, A. S. Ernst, C. Fritsche, U. Gertig, N. Saiepour, K. Gronke, C. Wrzos, S. Ribes, S. Rolfes, J. Weinstein,

H. Ehrenreich, T. Pukrop, J. Kopatz, C. Stadelmann, G. Salinas-Riester, M. S. Weber, M. Prinz, W. Brück, B. J. L. Eggen, H. W. G. M. Boddeke, J. Priller, U. K. Hanisch, CD14 is a key organizer of microglial responses to CNS infection and injury. *Glia*. **64**, 635–649 (2016).

134. T. D. Troutman, J. F. Bazan, C. Pasare, Toll-like receptors, signalingadapters and regulation of the pro-inflammatory response by PI3K. *Cell Cycle*. **11**, 3559–3567 (2012).

135. D. A. Ferrington, D. S. Gregerson, *Immunoproteasomes: Structure, function, and antigen presentation* (2012), vol. 109.

136. I. A. York, K. L. Rock, Antigen Processing and Presentation By the Class I Major Histocompatibility Complex. *Annu. Rev. Immunol.* **14**, 369–396 (1996).

137. R. M. Ransohoff, V. H. Perry, Microglial Physiology: Unique Stimuli, Specialized Responses. *Annu. Rev. Immunol.* **27**, 119–145 (2009).

138. R. T. Palframan, S. Jung, G. Cheng, W. Weninger, Y. Luo, M. Dorf, D. R. Littman, B. J. Rollins, H. Zweerink, A. Rot, U. H. Von Andrian, Inflammatory chemokine transport and presentation in HEV: A remote control mechanism for monocyte recruitment to lymph nodes in inflamed tissues. *J. Exp. Med.* **194**, 1361–1373 (2001).

139. J. B. McLachlan, J. P. Hart, S. V. Pizzo, C. P. Shelburne, H. F. Staats, M. D. Gunn, S. N. Abraham, Mast cell-derived tumor necrosis factor induces hypertrophy of draining lymph nodes during infection. *Nat. Immunol.* **4**, 1199–1205 (2003).

140. J. L. K. Wee, D. L. V Greenwood, X. Han, J. P. Y. Scheerlinck, Inflammatory cytokines IL-6 and TNF-α regulate lymphocyte trafficking through the local lymph node. *Vet. Immunol. Immunopathol.* **144**, 95–103 (2011).

141. F. Garrido, F. Ruiz-Cabello, T. Cabrera, J. J. Pérez-Villar, M. López-Botet, M. Duggan-

Keen, P. L. Stern, Implications for immunosurveillance of altered HLA class I phenotypes in human tumours. *Immunol. Today*. **18**, 89–95 (1997).

142. B. Seliger, M. J. Maeurer, S. Ferrone, Antigen-processing machinery breakdown and tumor growth. *Immunol. Today*. **21**, 455–464 (2000).

143. A. Passarelli, F. Mannavola, L. S. Stucci, M. Tucci, F. Silvestris, Immune system and melanoma biology: A balance between immunosurveillance and immune escape. *Oncotarget*. **8**, 106132–106142 (2017).

144. A. Paschen, R. María Méndez, P. Jimenez, A. Sucker, F. Ruiz-Cabello, M. Song, F. Garrido, D. Schadendorf, Complete loss of HLA class I antigen expression on melanoma cells: A result of successive mutational events. *Int. J. Cancer*. **103**, 759–767 (2003).

145. D. J. Propper, D. Chao, J. P. Braybrooke, P. Bahl, P. Thavasu, F. Balkwill, H. Turley, N. Dobbs, K. Gatter, D. C. Talbot, A. L. Harris, T. S. Ganesan, Low-Dose IFN-γ Induces Tumor MHC Expression in Metastatic Malignant Melanoma. *Clin. Cancer Res.* **9**, 84–92 (2003).

146. R. Medzhitov, Recognition of microorganisms and activation of the immune response. *Nature*. **449**, 819–826 (2007).

147. A. F. McGettrick, L. A. J. O'Neill, Toll-like receptors: Key activators of leucocytes and regulator of haematopoiesis. *Br. J. Haematol.* **139**, 185–193 (2007).

148. R. Patro, G. Duggal, M. I. Love, R. A. Irizarry, C. Kingsford, Salmon provides fast and bias-aware quantification of transcript expression. *Nat. Methods*. **14**, 417–419 (2017).

149. C. Soneson, M. I. Love, M. D. Robinson, Differential analyses for RNA-seq: transcript-level estimates improve gene-level inferences. *F1000Research*. **4**, 1521 (2015).

150. M. I. Love, W. Huber, S. Anders, Moderated estimation of fold change and dispersion for

RNA-seq data with DESeq2. *Genome Biol.* **15**, 1–21 (2014).

151. A. Liberzon, A. Subramanian, R. Pinchback, H. Thorvaldsdóttir, P. Tamayo, J. P. Mesirov, Molecular signatures database (MSigDB) 3.0. *Bioinformatics*. **27**, 1739–1740 (2011).

152. A. A. Sergushichev, An algorithm for fast preranked gene set enrichment analysis using cumulative statistic calculation. *bioRxiv*, 060012 (2016).

153. K. R. Kelson, K. M. Kroeger, G. D. King, W. Xiong, M. G. Castro, P. R. Lowenstein, N. S. Sanderson, A. G. Muhammad, C. Liu, D. Larocque, Combined Flt3L/TK Gene Therapy Induces Immunological Surveillance Which Mediates an Immune Response Against a Surrogate Brain Tumor Neoantigen. *Mol. Ther.* **19**, 1793–1801 (2011).

154. S. Ali, G. D. King, J. F. Curtin, M. Candolfi, W. Xiong, C. Liu, M. Puntel, Q. Cheng, J. Prieto, A. Ribas, J. Kupiec-, N. Van Rooijen, H. Lassmann, P. R. Lowenstein, G. Maria, Combined Immunostimulation and Conditional Cytotoxic Gene Therapy Provide Long-term Survival in a Large Glioma Model. *Cancer Res.* **65**, 7194–7204 (2005).

155. G. D. King, A. K. M. G. Muhammad, J. F. Curtin, C. Barcia, M. Puntel, C. Liu, S. B. Honig, M. Candolfi, S. Mondkar, P. R. Lowenstein, M. G. Castro, Flt3L and TK gene therapy eradicate multifocal glioma in a syngeneic glioblastoma model. *Neuro. Oncol.*, 19–31 (2008).

156. A. G. Muhammad, M. Candolfi, G. D. King, K. Yagiz, D. Foulad, Y. Mineharu, K. M. Kroeger, K. A. Treuer, S. Nichols, N. S. Sanderson, J. Yang, M. Khayznikov, N. Van Rooijen, P. R. Lowenstein, M. G. Castro, Antiglioma Immunological Memory in Response to Conditional Cytotoxic/Immune-Stimulatory Gene Therapy: Humoral and Cellular Immunity Lead to Tumor Regression. *Clin. Cancer Res.* **15**, 6113–6127 (2009).

157. M. R. P. Elmore, A. R. Najafi, M. A. Koike, N. N. Dagher, E. E. Spangenberg, R. A. Rice, M. Kitazawa, B. Matusow, H. Nguyen, B. L. West, K. N. Green, Colony-stimulating factor 1 receptor signaling is necessary for microglia viability, unmasking a microglia progenitor cell in the adult brain. *Neuron*. **82**, 380–397 (2014).